

# Chemical Studies on the Uses of Urea Complexes to Synthesize Compounds Having Electrical and Biological Applications

Omar B. Ibrahim<sup>\*1</sup>, Moamen S. Refat<sup>1,2</sup>, Mahmoud Salman<sup>1</sup>, M.M. AL-Majthoub<sup>1</sup>

<sup>1</sup>Department of Chemistry, Faculty of Science, Taif University, Al-Hawiah, Taif, P.O. Box 888, 21974, Saudi Arabia

<sup>2</sup>Department of Chemistry, Faculty of Science, Port Said University, Port Said, Egypt

omarstar1958@yahoo.com

**Abstract-** The chelation of urea (U) with silver(I), chromium(III), cadmium(II) and zinc(II) ions at different state of temperatures has been studied by elemental analyses, magnetic susceptibility, conductivity measurements, (infrared and <sup>1</sup>H-NMR) spectra, thermal analysis (TG/DTG), scanning electron microscopy (SEM), Energy-dispersive X-ray spectroscopy (EDX), and x-ray powder diffraction (XRD). The high values of molar conductivity of the resulting urea complexes show them to be electrolytes in nature. The physical and spectral data were well explained in terms of the formation of AgNO<sub>3</sub>.2U.6CH<sub>3</sub>OH (1), AgNO<sub>3</sub>.2U.CH<sub>3</sub>OH (2) and Ag metal (3) for silver(I), CrCl<sub>3</sub>.2U.12H<sub>2</sub>O (4), CrCl<sub>3</sub>.4U.9H<sub>2</sub>O (5) and Cr<sub>2</sub>O<sub>3</sub> (6) for chromium(III), CdCl<sub>2</sub>.2U. H<sub>2</sub>O (7), CdCl<sub>2</sub>.4U.H<sub>2</sub>O (8) and CdO (9) for cadmium(II) and ZnCl<sub>2</sub>.4U.4H<sub>2</sub>O (10), ZnCl<sub>2</sub>.2U.6H<sub>2</sub>O (11) and ZnO (12) for zinc(II). Complexes of urea (1, 4, 7 and 10), (2, 5, 8 and 11) and (3, 6, 9 and 12) were synthesized at room, 60°C and 800°C, respectively. On the basis of the infrared spectral data and the values of stretching vibrational bands of both -C=O and -NH<sub>2</sub> groups, the complexation of metal ions toward urea was distinguished. The enhancement of the microbial treatments against bacteria (*Escherichia Coli*, *Staphylococcus Aureus*, *Bacillus subtilis* and *Pseudomonas aeruginosa*) and fungi (*Aspergillus Flavus* and *Candida Albicans*) was assessed and recorded remarkable efficiency.

**Keywords-** Urea; Transition Metals; Biological Activity; Conductance; Spectroscopic Studies; Thermal Analysis

## I. INTRODUCTION

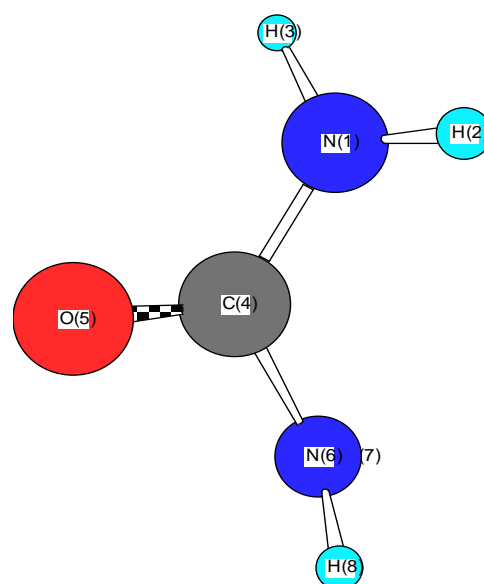
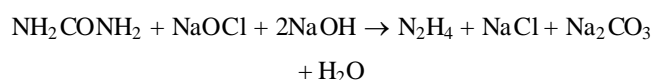
Carbamide, carbonyldiamide or the most famous name, urea (Scheme 1), CH<sub>4</sub>N<sub>2</sub>O, was first prepared by Wöhler<sup>[1]</sup> by evaporating a solution containing a mixture of potassium isocyanate and ammonium sulphate. Ammonium isocyanate, which is formed first, undergoes molecular rearrangement to give urea, as shown by the following reaction:



Urea may be prepared in the laboratory by the interaction of ammonia with carbonyl chloride, alkyl carbonates, chloroformates or urethans. Industrially<sup>[2-4]</sup>, urea is prepared by allowing liquid carbon dioxide and liquid ammonia to interact, and heating the formed ammonium carbamate at 130 ~ 150 °C under about 35 atmospheric pressure. The carbamate is decomposed to form urea and water according to the following reaction;



Urea is physiologically very important. It is the chief nitrogenous product of protein metabolism. Adults excrete about 30 g of urea per day in the urine, from which it can be extracted by evaporating the urine to small volume and adding nitric acid, to give the slightly soluble urea nitrate, CO(NH<sub>2</sub>)<sub>2</sub>.HNO<sub>3</sub>. Urea has a melting point of 132°C, soluble in water and ethanol, but insoluble in ether. Urea is used for preparing formaldehyde-Urea resin (plastics)<sup>[5]</sup>, barbiturates<sup>[6]</sup>, and fertilizers<sup>[7-10]</sup>. Urea is also extensively used in the paper industry to soften cellulose and has been used to promote healing in infected wounds and many other applications in the field of medicine<sup>[11-13]</sup>. Recently, urea is used for the manufacture of hydrazine in which urea is treated with alkaline sodium hypochlorite<sup>[6]</sup> e.g.,



Scheme 1 Structure of urea

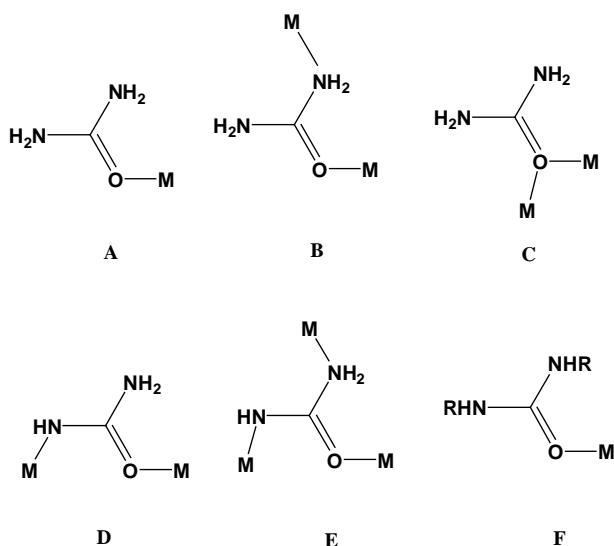
Urea is used in reactive dyeing<sup>[14]</sup> which has an effect on the formation and cleavage of covalent bond between the reactive dye and cellulose. The overall effect of urea on reactive dyeing depends on the solvolytic stability of the dye-fiber bond under specific dyeing conditions.

Complexes of urea with some metal ions are used as fertilizers<sup>[15-18]</sup>. Complexes of urea with zinc sulphate and

nitrate,  $[\text{Zn}(\text{CON}_2\text{H}_4)_6]\text{SO}_4 \cdot \text{H}_2\text{O}$  and  $[\text{Zn}(\text{CON}_2\text{H}_4)_4](\text{NO}_3)_2 \cdot 2\text{H}_2\text{O}$  have very important application in this field<sup>[19]</sup>. These complexes were found to increase the yield of rice more than a dry mixture of urea-zinc salt does. Calcium nitrate-urea complex,  $[\text{Ca}(\text{urea})_4](\text{NO}_3)_2$ ,<sup>[20, 21]</sup> was used also as an adduct fertilizer. Some metal-urea complexes have pharmaceutical application, e.g., the platinum-urea complex which is used as antitumor<sup>[22]</sup>.

Crystal structure studies have shown that in solid urea, both nitrogen atoms are identical. Bond length measurements<sup>[6]</sup> in urea give the C-N distance as 1.37 Å, while, in aliphatic amines the C-N bond length is 1.47 Å. This indicates that the C-N bond in urea has some double bond character (about 28%).

Urea usually coordinates as a monodentate ligand through the oxygen atom, forming a  $\text{C}=\text{O} \cdots \text{M}$  angle considerably smaller than 180°, in accordance with the  $sp^2$  hybridization of the O atom (**A** in Scheme 2). The rare N, O-bidentate coordination mode (**B** in Scheme 2) has been found in a very limited number of cases<sup>[23, 24]</sup>, while in  $[\text{Hg}_2\text{Cl}_4\text{U}_2]$  each U molecule bridges the two  $\text{Hg}^{\text{II}}$  atoms through the oxygen atom<sup>[25]</sup> (**C** in Scheme 2). Of particular chemical/biological interest is the ability of U to undergo metal-promoted deprotonation<sup>[26]</sup>, the monoanionic ligand  $\text{H}_2\text{NCONH}^-$  adopts the  $\mu_2$  (**D** in Scheme 2) and  $\mu_3$  (**E** in Scheme 2) coordination modes. The urea and its derivatives such as the N,N'-dimethylurea and N,N'-diethylurea (Scheme 2) have only been found to coordinate as monodentate ligands through the oxygen atom (**F** in Scheme 2).



Scheme 2 The coordination modes of urea towards metal ions

Raman and infrared spectra of urea have been observed by several investigators<sup>[27-32]</sup>. The normal vibrations of the urea molecule were calculated by Kellner<sup>[33]</sup> on the assumption of the non-planar model. However, on the basis of the dichroic measurement of the infrared band arising from the N-H stretching vibration by Waldron and Badger<sup>[34]</sup> and the proton magnetic resonance absorption measurement made by Andrew and Hyndman<sup>[35]</sup>, it is

concluded that urea molecule has a planar structure. Yamaguchi et al.<sup>[36]</sup> calculated the normal vibrations of the  $\text{C}_{2v}$  model of urea molecule as an eight-body problem using a potential function of the Urey-Bradley force field and obtained the force constants which have been refined by the least-squares method. Based on the result of these calculations, Yamaguchi<sup>[36]</sup>, assigned all of the observed frequencies in the spectra of urea and urea- $d_4$ . To the two vibrations of the frequencies  $1686 \text{ cm}^{-1}$  and  $1603 \text{ cm}^{-1}$ , there are considerable contributions of both CO stretching and  $\text{NH}_2$  bending motions, whereas Stewart<sup>[37]</sup> assigned the  $1686 \text{ cm}^{-1}$  band to CO stretching vibration and the  $1603 \text{ cm}^{-1}$  band to  $\text{NH}_2$  bending motion. The calculations studied by Yamaguchi showed that for the band at  $1686 \text{ cm}^{-1}$ , the contribution of the  $\text{NH}_2$  bending motion is greater than that of CO stretching motion. The band at  $1629 \text{ cm}^{-1}$  corresponds to almost pure  $\text{NH}_2$  bending vibration. The  $\text{NH}_2$  bending motion of  $\text{A}_1$  type is equal to that of  $\text{B}_2$  type. The  $\text{A}_1$  type band should have a frequency of about  $1630 \text{ cm}^{-1}$ , if there is no coupling between  $\text{NH}_2$  bending and CO stretching motions. On the other hand, the observed frequency of  $1610 \text{ cm}^{-1}$  of urea- $d_4$  is assigned to almost pure skeletal vibration. Therefore, the interaction between the  $1630 \text{ cm}^{-1}$  and  $1610 \text{ cm}^{-1}$  vibration gives rise to the two observed bands at  $1686 \text{ cm}^{-1}$  and  $1603 \text{ cm}^{-1}$ . The infrared bands of urea- $d_4$  observed at  $1245 \text{ cm}^{-1}$  and  $1154 \text{ cm}^{-1}$  are assigned, respectively, to  $\text{A}_1$  type and  $\text{B}_2$  type,  $\text{ND}_2$  bending vibrations. This assignment is consistent with the observed depolarization degrees of the Raman lines. The large frequency difference between the  $\text{A}_1$  and  $\text{B}_2$  vibrations is due to the fact that in the  $\text{A}_1$  vibration, the cross term related to the CN stretching vibration is large.

The  $1464 \text{ cm}^{-1}$  frequency of urea is assigned to the CN stretching vibration of  $\text{B}_2$  type. The corresponding frequency of urea- $d_4$  is observed at  $1490 \text{ cm}^{-1}$ . The  $1150 \text{ cm}^{-1}$  band is assigned to  $\text{NH}_2$  rocking vibrations of both  $\text{A}_1$  and  $\text{B}_2$  types. The normal vibration calculation yields almost the same values for these frequencies.

Urea possesses two types of potential donor atoms, the carbonyl oxygen and amide nitrogens. Penland et al.<sup>[38]</sup> studied the infrared spectra of urea complexes to determine whether coordination occurred through oxygen or nitrogen atoms. The electronic structure of urea may be represented by a resonance hybrid of structures **A-F** as shown in scheme 1 with each contributing roughly an equal amount. If coordination occurs through nitrogen, contributions of structure **B** will decrease. This results in an increase of the CO stretching frequency with a decrease of CN stretching frequency. The N-H stretching frequency in this case may fall in the same range as those of the amido complexes. If coordination occurs through oxygen, the contribution of structure (**A**) will decrease. This may result in a decrease of the CO stretching frequency but no appreciable change in NH stretching frequency. Since the vibrational spectrum of urea itself has been analyzed completely<sup>[36]</sup>, band shifts caused by coordination can be checked immediately. For example, the effect of the coordination on the spectra of the complexes of urea with  $\text{Pt}(\text{II})$  and  $\text{Cr}(\text{III})$  in which the coordination occurs through nitrogen and oxygen atoms, respectively<sup>[38]</sup>. The mode of coordination of urea with

metal ions seems to be dependent upon the type and nature of metal. Pd(II) coordinates to the nitrogen, whereas Fe(III), Zn(II), and Cu(II) coordinate to the oxygen of urea<sup>[38]</sup>.

In urea-metal complexes, if a nitrogen-to-metal bond is present, the vibrational spectrum of this complex differs significantly from that of the free urea molecule. The N-H stretching frequencies would be shifted to lower values, and the C=O bond stretching vibration ( $\nu(\text{C}=\text{O})$ ) would be shifted to higher frequency at about  $1700\text{ cm}^{-1}$ <sup>[39]</sup>.

Recently, urea represents not only an important molecule in biology<sup>[40]</sup> but also an important raw material in chemical industry<sup>[41]</sup>. The aim of this publication is to report the synthesis, characterization, conductance and biological studies of the resulting compounds formed from the reactions of urea with  $\text{AgNO}_3$ ,  $\text{CrCl}_3 \cdot 6\text{H}_2\text{O}$ ,  $\text{CdCl}_2 \cdot \text{H}_2\text{O}$  and  $\text{ZnCl}_2$  at room, elevated and ignition temperatures.

## II. EXPERIMENTAL

### A. Materials

Urea,  $\text{AgNO}_3$ ,  $\text{CrCl}_3 \cdot 6\text{H}_2\text{O}$ ,  $\text{CdCl}_2 \cdot \text{H}_2\text{O}$ ,  $\text{ZnCl}_2$  and methanol solvent were obtained from Aldrich Company. Urea was received from Fluka chemical company. All chemicals used in this study were of analytically reagent grade and used without further purification.

### B. Synthesis of Ag(I), Cr(III), Cd(II) and Zn(II) Urea Complexes

#### 1) Synthesis of Urea Complexes at Room Temperature:

The complexes,  $\text{AgNO}_3 \cdot 2\text{U} \cdot 6\text{CH}_3\text{OH}$  (**1**),  $\text{CrCl}_3 \cdot 2\text{U} \cdot 12\text{H}_2\text{O}$  (**4**),  $\text{CdCl}_2 \cdot 2\text{U} \cdot \text{H}_2\text{O}$  (**7**) and  $\text{ZnCl}_2 \cdot 4\text{U} \cdot 4\text{H}_2\text{O}$  (**10**) were prepared by mixing equal methanolic solutions of  $\text{AgNO}_3$  (1.70 g, 0.01 mole),  $\text{CrCl}_3 \cdot 6\text{H}_2\text{O}$  (2.67 g, 0.01 mole),  $\text{CdCl}_2 \cdot \text{H}_2\text{O}$  (2.02 g, 0.01 mole) or  $\text{ZnCl}_2$  (1.37 g, 0.01 mole) in 25 mL methanol with a 50 mL volume of urea solution (6.0 g, 0.1 mole) in methanol solvent. The mixtures were allowed to be stirred for about 12 hours under refluxed system at room temperature *Ca.* 25°C. In all cases of Ag(I), Cr(III), Cd(II) and Zn(II)-urea mixtures, the products took longer time of precipitation. In all the cases, the amount of the formed precipitate was increased with increasing the time of standing. The colored precipitation complexes formed in each case was filtered off, dried under *vacuo* over anhydrous calcium chloride.

#### 2) Synthesis of Urea Complexes at 60 °C:

The urea complexes,  $\text{AgNO}_3 \cdot 2\text{U} \cdot \text{CH}_3\text{OH}$  (**2**),  $\text{CrCl}_3 \cdot 4\text{U} \cdot 9\text{H}_2\text{O}$  (**5**),  $\text{CdCl}_2 \cdot 4\text{U} \cdot \text{H}_2\text{O}$  (**8**) and  $\text{ZnCl}_2 \cdot 2\text{U} \cdot 6\text{H}_2\text{O}$  (**11**), were prepared by a method similar to that described for the preparation of urea complexes at room temperature. A 25 mL volume of urea solution (6.0 g, 0.1 mole) was mixed with an equal volume of Ag(I), Cr(III), Cd(II) or Zn(II) salts solution,  $\text{AgNO}_3$  (1.70 g, 0.01 mole),  $\text{CrCl}_3 \cdot 6\text{H}_2\text{O}$  (2.67 g, 0.01 mole),  $\text{CdCl}_2 \cdot \text{H}_2\text{O}$  (2.02 g, 0.01 mole) or  $\text{ZnCl}_2$  (1.37 g, 0.01 mole) in 25 mL methanol. The mixtures were stirred for about 2 hours then heated to 60°C for 6 hours on a water bath under refluxed system. The

precipitated products were filtered off, dried at 60 °C in an oven for 3 hours and then dried under *vacuo* over anhydrous calcium chloride.

### C. Measurements

The elemental analyses of carbon, hydrogen and nitrogen contents were performed by the microanalysis unit at Cairo University, Egypt, using a Perkin Elmer CHN 2400 (USA). The molar conductivities of freshly prepared  $1.0 \times 10^{-3}\text{ mol/cm}^3$  dimethylsulfoxide (DMSO) solutions were measured for the soluble urea complexes using Jenway 4010 conductivity meter. Magnetic measurements were performed on the Magnetic Susceptibility Balance, Sherwood Scientific, and Cambridge Science Park-Cambridge-England. The infrared spectra with KBr discs were recorded on a Bruker FT-IR Spectrophotometer ( $4000\text{--}400\text{ cm}^{-1}$ ). The  $^1\text{H-NMR}$  (400 MHz) spectra were recorded on Varian Gemini Spectrophotometers. The thermal studies TG/DTG-50H were carried out on a Shimadzu thermogravimetric analyzer under static air till 800 °C. Scanning electron microscopy (SEM) images and Energy Dispersive X-ray Detection (EDX) were taken in Joel JSM-6390 equipment, with an accelerating voltage of 20 KV. The X-ray diffraction patterns for the urea complexes were recorded on X Pert PRO PANalytical X-ray powder diffraction, target copper with secondary monochromate.

### D. Antibacterial and Antifungal Activities

Antimicrobial activity of the tested samples was determined using a modified Kirby-Bauer disc diffusion method<sup>[42]</sup>. Briefly, 100  $\mu\text{l}$  of the best bacteria/fungi were grown in 10 mL of fresh media until they reached a count of approximately 108 cells/mL for bacteria and 105 cells/mL for fungi<sup>[43]</sup>. 100  $\mu\text{l}$  of microbial suspension was spread onto agar plates corresponding to the broth in which they were maintained. Isolated colonies of each organism that might be playing a pathogenic role should be selected from primary agar plates and tested for susceptibility by disc diffusion method<sup>[44, 45]</sup>.

Of the many media available, National Committee for Clinical Laboratory Standards (NCCLS) recommends Mueller-Hinton agar due to: it results in good batch-to-batch reproducibility. Disc diffusion method for filamentous fungi is tested by using approved standard method (M38-A) developed by the NCCLS<sup>[46]</sup> for evaluating the susceptibility of filamentous fungi to antifungal agents. Disc diffusion method for yeast developed standard method (M44-P) by the NCCLS<sup>[47]</sup>. Plates inoculated with filamentous fungi as *Aspergillus Flavus* at 25°C for 48 hours; Gram (+) bacteria as *Staphylococcus Aureus*, *Bacillus subtilis*; Gram (-) bacteria as *Escherichia Coli*, *Pseudomonas aeruginosa* they were incubated at 35-37°C for 24-48 hours and yeast as *Candida Albicans* incubated at 30°C for 24-48 hours and, then the diameters of the inhabitation zones were measured in millimeters<sup>[42]</sup>. Standard discs of Tetracycline (Antibacterial agent), Amphotericin B (Antifungal agent) served as positive controls for antimicrobial activity but filter disc impregnated

with 10  $\mu$ l of solvent (distilled water, chloroform, DMSO) were used as a negative control.

The agar used is Mueller-Hinton agar that is rigorously tested for composition and pH. Furthering the depth of the agar in the plate is a factor to be considered in the disc diffusion method. This method is well documented and standard zones of inhibition which have been determined for susceptible values. Blank paper disks (Schleicher & Schuell, Spain) with a diameter of 8.0 mm were impregnated 10  $\mu$ l of tested concentration of the stock solutions. When a filter paper disc impregnated with a tested chemical is placed on agar, the chemical will diffuse from the disc into the agar. This diffusion will place the chemical in the agar only around the disc. The solubility of the chemical and its molecular size will determine the size of the area of chemical infiltration around the disc. If an organism is placed on the agar, it will not grow in the area around the disc if it is susceptible to the chemical. This area of no growth around the disc is known as a "Zone of inhibition" or "Clear zone". For the disc diffusion, the zone diameters were measured with slipping calipers of the National for Clinical Laboratory Standards [44]. Agar-based methods such as Etest disk diffusion can be good alternatives because they are simpler and faster than broth methods [48, 49].

### III. RESULTS AND DISCUSSION

The color, physical characteristic, micro-analytical data, molar conductance measurements of Ag(I), Cr(III), Cd(II) and Zn(II) urea complexes are given in Table 1. The elemental analysis data of some prepared complexes revealed 1 : 2 molar ratio (M:U) (where M = Ag(I), Cr(III), Cd(II) or Zn(II) and U = urea) and good agreement with the general formulas  $\text{AgNO}_3 \cdot 2\text{U} \cdot 6\text{CH}_3\text{OH}$  (1),  $\text{AgNO}_3 \cdot 2\text{U} \cdot \text{CH}_3\text{OH}$  (2),  $\text{CrCl}_3 \cdot 2\text{U} \cdot 12\text{H}_2\text{O}$  (4),  $\text{CdCl}_2 \cdot 2\text{U} \cdot \text{H}_2\text{O}$  (7), and  $\text{ZnCl}_2 \cdot 2\text{U} \cdot 6\text{H}_2\text{O}$  (11). On the other hand,  $\text{CrCl}_3 \cdot 4\text{U} \cdot 9\text{H}_2\text{O}$  (5),  $\text{CdCl}_2 \cdot 4\text{U} \cdot \text{H}_2\text{O}$  (8) and  $\text{ZnCl}_2 \cdot 4\text{U} \cdot 4\text{H}_2\text{O}$  (10) complexes formed with 1 : 4 (M : U) molar ratio. It is important to mention that complexes 1, 4, 7, and 10 of urea were prepared at room temperature but urea complexes of 2, 5, 8, and 11 were resulted from the complexation between urea and Ag(I), Cr(III), Cd(II) or Zn(II) ions at 60 °C with molar ratio 4 : 1 (U : M). The reactions can be represented by the stoichiometric equations:

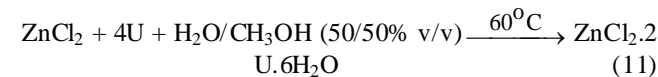
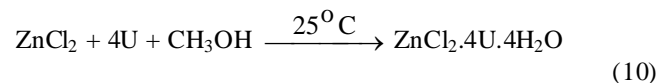
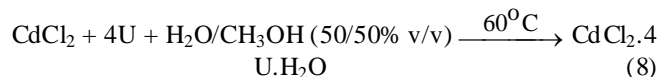
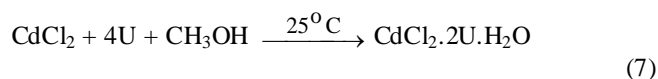
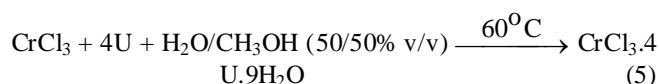
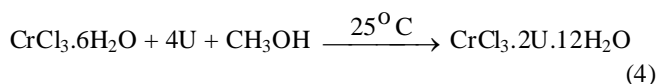
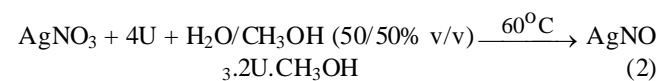
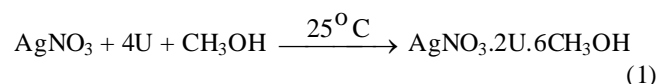


TABLE I PHYSICAL CHARACTERIZATION, MICRO-ANALYTICAL AND MOLAR CONDUCTANCE DATA OF UREA COMPLEXES

Complexes Molecular Formula Empirical Formula (MW.)	Color	Molar Ratio	Elemental Analysis (%) Found (Calcd.)		$\Delta m$ ( $\Omega^{-1} \text{cm}^2 \text{mol}^{-1}$ )
			C	H	
$\text{AgNO}_3 \cdot 2\text{U} \cdot 6\text{CH}_3\text{OH}$ (1) 481.87 g/mol	Grey	1:2	19.7 9 (19.9 2)	6.46 (6.64)	75
$\text{AgNO}_3 \cdot 2\text{U} \cdot \text{CH}_3\text{OH}$ (2) 321.87 g/mol	Dark grey	1:2	10.7 0 (11.1 8)	3.70 (3.37)	83
$\text{CrCl}_3 \cdot 2\text{U} \cdot 12\text{H}_2\text{O}$ (4) 494.55 g/mol	Dark green	1:2	4.70 (4.85 )	6.40 (6.47)	154
$\text{CrCl}_3 \cdot 4\text{U} \cdot 9\text{H}_2\text{O}$ (5) 560.55 g/mol	Green	1:4	8.60 (8.56 )	5.94 (6.06)	149
$\text{CdCl}_2 \cdot 2\text{U} \cdot \text{H}_2\text{O}$ (7) 321.32 g/mol	White	1:2	7.60 (7.47 )	2.96 (3.11)	98
$\text{CdCl}_2 \cdot 4\text{U} \cdot \text{H}_2\text{O}$ (8) 441.32 g/mol	White	1:4	10.7 0 (10.8 7)	3.98 (4.08)	103
$\text{ZnCl}_2 \cdot 4\text{U} \cdot 4\text{H}_2\text{O}$ (10) 448.29 g/mol	White	1:4	10.9 1 (10.7 1)	5.46 (5.35)	121
$\text{ZnCl}_2 \cdot 2\text{U} \cdot 6\text{H}_2\text{O}$ (11) 364.29 g/mol	White	1:2	6.50 (6.59 )	6.50 (6.59)	107

The complexes are hygroscopic, low melting points, soluble in  $\text{H}_2\text{O}$  and dimethylsulfoxide, DMSO. The molar conductivities of  $10^{-3} \text{ mol dm}^{-3}$  solutions of the prepared complexes in DMSO (Table 1) indicate that the complexes have an electrolytic nature.

#### A. Molar Conductance Measurements

The molar conductivity values for the urea complexes in DMSO solvent ( $10^{-3} \text{ mol dm}^{-3}$ ) are exhibited in the range of (75–154)  $\Omega^{-1} \text{cm}^2 \text{mol}^{-1}$ , suggesting them to be electrolytes (Table 1). Conductivity measurements within the limits of their solubility provide a method of testing the degree of ionization of the complexes, the molar ions that a complex liberates in solution (in case of presence anions outside the coordination sphere), the higher will be its molar conductivity and vice versa. It is clear from the conductivity data that the complexes present seems to be electrolytes.

Also the molar conductance values indicate that the anions present outside the coordination sphere. This result was confirmed from the elemental analysis data where  $\text{Cl}^-$  or  $\text{NO}_3^-$  ions are precipitated with colored solution by adding of  $\text{AgNO}_3$  or  $\text{FeSO}_4$  solutions, respectively, this experimental test is well matched with CHN data. All these complexes have electrolytic properties. This fact elucidated that the  $\text{Cl}^-$  or  $\text{NO}_3^-$  were present. These results establish the stoichiometry of these complexes, which are in agreement with the general formulas suggested.

### B. Magnetic Measurements

Magnetic measurements were carried out on a Sherwood Scientific magnetic balance according to the Gauy method. The calculations were evaluated by applying the following equations:

$$\chi_g = \frac{c(R - R_o)}{10^9 M}$$

$$\chi_m = \chi_g MWt.$$

$$\mu_{eff} = 2.828\sqrt{\chi_m T}$$

where  $\chi$  is mass susceptibility per gm sample

$c$  is the calibration constant of the instrument and equal to 0.0816

$R$  is the balance reading for the sample and tube

$R_o$  is the balance reading for the empty tube

$M$  is the weight of the sample in gm

$T$  is the absolute temperature

The magnetic moments of the  $\text{CrCl}_3 \cdot 2\text{U} \cdot 12\text{H}_2\text{O}$  (4) and  $\text{CrCl}_3 \cdot 4\text{U} \cdot 9\text{H}_2\text{O}$  (5) complexes at  $T = 300$  K and their corresponding hybrid orbitals were calculated. The observed values of the effective magnetic moments  $\mu_{eff}$  measured for these complexes equal to 2.85 B.M., this is in convenient with experimental values of 3.27 B.M. [50] obtained for octahedral Cr(III) complex with  $d^2sp^3$  hyperdization for both Cr(III)/U complexes.

### C. Infrared Spectra

The infrared spectra of the Ag(I), Cr(III), Cd(II) and Zn(II) urea complexes at room,  $60^\circ\text{C}$  and  $800^\circ\text{C}$  temperature are shown in Figs. 1, 2 and 3, respectively. The band locations were measured for the mentioned urea complexes, together with the proposed assignments for the most characteristic vibrations are presented in Tables 2, 3, 4 and 5. In order to facilitate the spectroscopic analysis and to put our hand on proper structure of the prepared complexes, the spectra of the urea complexes were accurately compared with those of the urea and similar complexes in literature survey. The infrared spectra in the wide frequency range ( $4000\text{--}400\text{ cm}^{-1}$ ) are shown in Fig. 1, whereas the region between  $1500\text{--}400\text{ cm}^{-1}$  is focused to urea complexes at  $800^\circ\text{C}$  temperatures (Fig. 3). The discussion of the spectra will be addressed on the basis of the most characteristic vibrations.

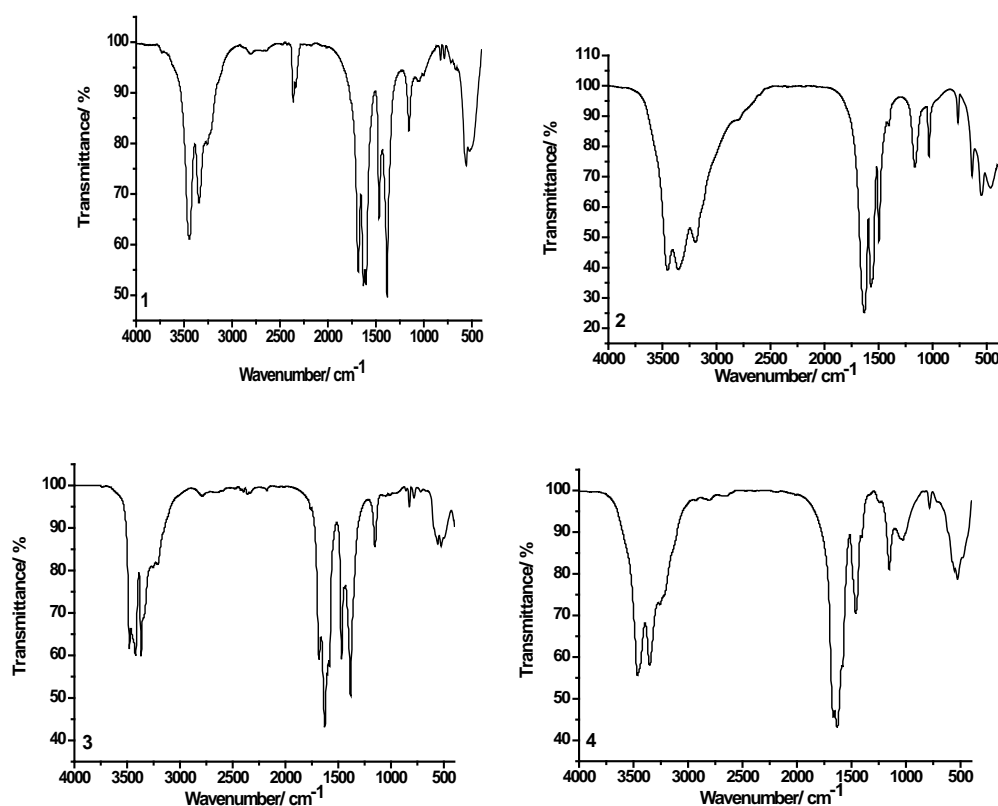


Fig. 1 Infrared spectra of urea complexes at room temperature:  $\text{AgNO}_3 \cdot 2\text{U} \cdot 6\text{CH}_3\text{OH}$  (1),  $\text{CrCl}_3 \cdot 2\text{U} \cdot 12\text{H}_2\text{O}$  (2),  $\text{CdCl}_2 \cdot 2\text{U} \cdot \text{H}_2\text{O}$  (3) and  $\text{ZnCl}_2 \cdot 4\text{U} \cdot 4\text{H}_2\text{O}$  complexes

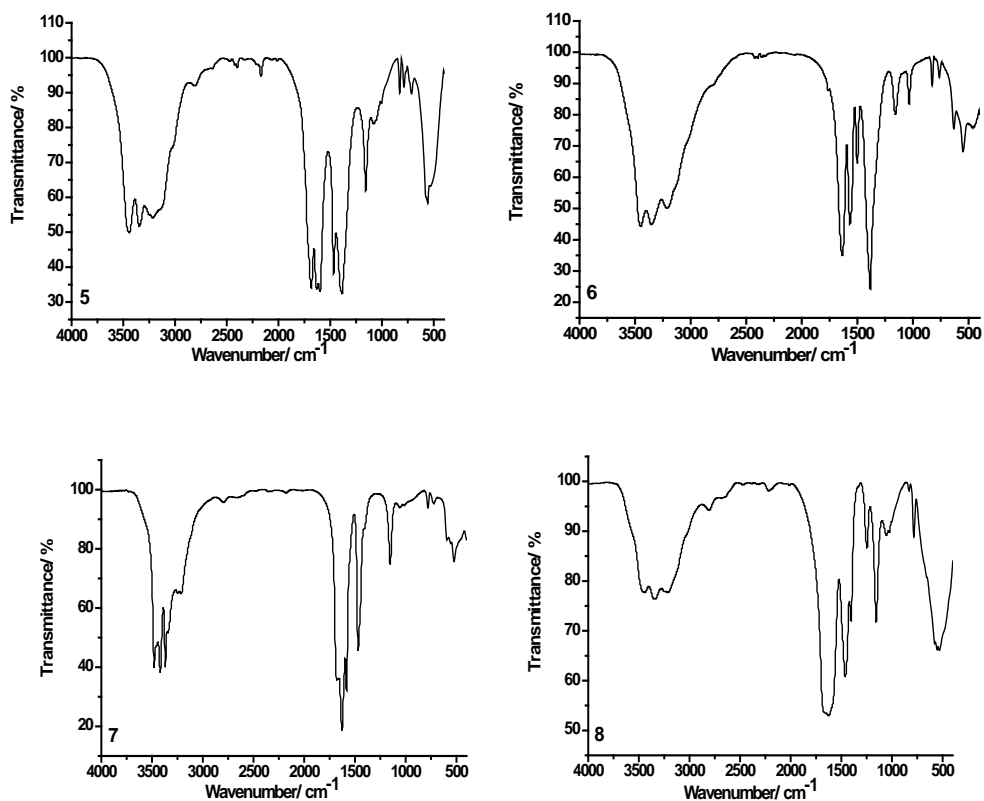


Fig. 2 Infrared spectra of urea complexes at  $60^\circ\text{C}$ :  $\text{AgNO}_3 \cdot 2\text{U} \cdot \text{CH}_3\text{OH}$  (5),  $\text{CrCl}_3 \cdot 4\text{U} \cdot 9\text{H}_2\text{O}$  (6),  $\text{CdCl}_2 \cdot 4\text{U} \cdot \text{H}_2\text{O}$  (7) and  $\text{ZnCl}_2 \cdot 2\text{U} \cdot 6\text{H}_2\text{O}$  (8) complexes

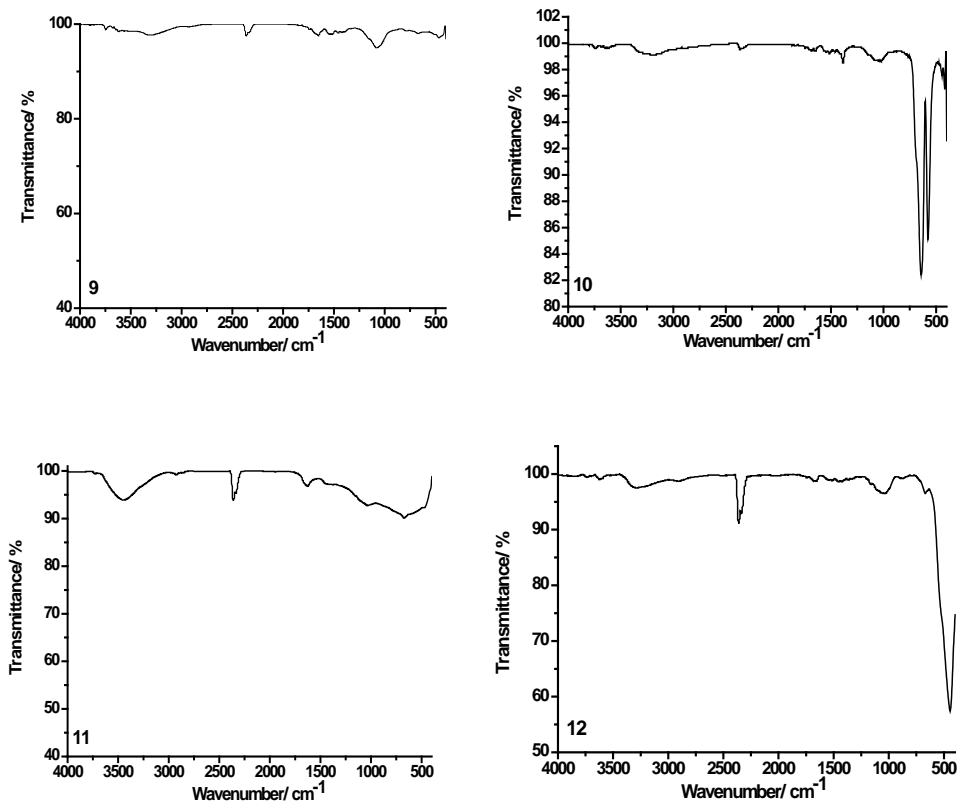


Fig. 3 Infrared spectra of urea complexes at  $800^\circ\text{C}$ :  $\text{AgO}/\text{Ag}$  metal (9),  $\text{Cr}_2\text{O}_3$  (10),  $\text{CdO}/\text{Cd}$  metal (11) and  $\text{ZnO}/\text{Zn}$  metal (12) compounds

TABLE II CHARACTERISTIC INFRARED FREQUENCIES ( $\text{CM}^{-1}$ ) AND TENTATIVE ASSIGNMENTS OF UREA (U),  $[\text{Pt}(\text{urea})_2\text{Cl}_2]$  (A),  $[\text{Cr}(\text{urea})_6]\text{Cl}_3$  (B),  $\text{AgNO}_3 \cdot 2\text{U} \cdot 6\text{CH}_3\text{OH}$  (1) AND  $\text{AgNO}_3 \cdot 2\text{U} \cdot \text{CH}_3\text{OH}$  (2) COMPLEXES

U	A	B	1	2	Assignments <sup>(b)</sup>
3450	3390 3290	3440 3330	3444 3344	3443 3345	$\nu_{\text{as}}(\text{NH}_2)$ $\nu(\text{OH}); \text{CH}_3\text{OH}$
3350	3130 3030	3190	3258	3215	$\nu_s(\text{NH}_2)$ $\nu(\text{CH}_3); \text{CH}_3\text{OH}$
1683	1725	1505	1684	1683	$\delta(\text{C}=\text{O})$
1471	1395	1505	1384	1387	$\nu(\text{C}-\text{N})$

TABLE III CHARACTERISTIC INFRARED FREQUENCIES ( $\text{CM}^{-1}$ ) AND TENTATIVE ASSIGNMENTS OF UREA (U),  $[\text{Pt}(\text{urea})_2\text{Cl}_2]$  (A),  $[\text{Cr}(\text{urea})_6]\text{Cl}_3$  (B),  $\text{CrCl}_3 \cdot 2\text{U} \cdot 12\text{H}_2\text{O}$  (4) AND  $\text{CrCl}_3 \cdot 4\text{U} \cdot 9\text{H}_2\text{O}$  (5) COMPLEXES

U	A	B	4	5	Assignments <sup>(b)</sup>
3450	3390 3290	3440 3330	3452 3354	3450 3353	$\nu(\text{OH}); \text{H}_2\text{O}$ $\nu_{\text{as}}(\text{NH}_2)$
3350	3130 3030	3190	3194	3211	$\nu_s(\text{NH}_2)$
1683	1725	1505	1630 1571	1635 1567	$\delta(\text{H}_2\text{O})$ $\delta(\text{C}=\text{O})$
1471	1395	1505	1497	1501	$\nu(\text{C}-\text{N})$

TABLE IV CHARACTERISTIC INFRARED FREQUENCIES ( $\text{CM}^{-1}$ ) AND TENTATIVE ASSIGNMENTS OF UREA (U),  $[\text{Pt}(\text{urea})_2\text{Cl}_2]$  (A),  $[\text{Cr}(\text{urea})_6]\text{Cl}_3$  (B),  $\text{CdCl}_2 \cdot 2\text{U} \cdot \text{H}_2\text{O}$  (7) AND  $\text{CdCl}_2 \cdot 4\text{U} \cdot \text{H}_2\text{O}$  (8) COMPLEXES

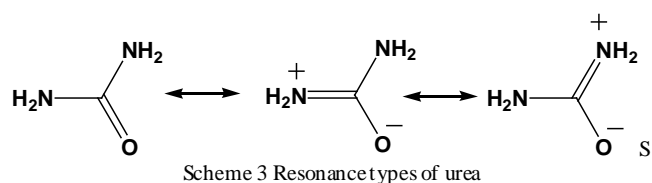
U	A	B	7	8	Assignments <sup>(b)</sup>
3450	3390 3290	3440 3330	3479 3420	3479 3419	$\nu(\text{OH}); \text{H}_2\text{O}$ $\nu_{\text{as}}(\text{NH}_2)$
3350	3130 3030	3190	3367 3210	3368 3211	$\nu_s(\text{NH}_2)$
1683	1725	1505	1681	1679	$\delta(\text{C}=\text{O})$
1471	1395	1505	1583	1583	$\nu(\text{C}-\text{N})$

TABLE V CHARACTERISTIC INFRARED FREQUENCIES ( $\text{CM}^{-1}$ ) AND TENTATIVE ASSIGNMENTS OF UREA (U),  $[\text{Pt}(\text{urea})_2\text{Cl}_2]$  (A),  $[\text{Cr}(\text{urea})_6]\text{Cl}_3$  (B),  $\text{ZnCl}_2 \cdot 4\text{U} \cdot 4\text{H}_2\text{O}$  (10) AND  $\text{ZnCl}_2 \cdot 2\text{U} \cdot 6\text{H}_2\text{O}$  (11) COMPLEXES

U	A	B	10	11	Assignments <sup>(b)</sup>
3450	3390 3290	3440 3330	3463 3351	3446 3344	$\nu(\text{OH}); \text{H}_2\text{O}$ $\nu_{\text{as}}(\text{NH}_2)$
3350	3130 3030	3190	3258	3212	$\nu_s(\text{NH}_2)$
1683	1725	1505	1630	1624	$\delta(\text{C}=\text{O})$ $\delta(\text{H}_2\text{O})$
1471	1395	1505	1462	1461	$\nu(\text{C}-\text{N})$

The assignments of full vibrational analysis of crystalline urea have been published<sup>[38]</sup>. Tables 2 to 5 give diagnostic infrared peaks of the free urea ligand, published work and Ag(I), Cr(III), Cd(II) and Zn(II) complexes. Assignments have been given in comparison with the data obtained for the free urea, that is, uncoordinated, U<sup>[38]</sup> and its  $[\text{Pt}(\text{urea})_2\text{Cl}_2]$  and  $[\text{Cr}(\text{urea})_6]\text{Cl}_3$  complexes<sup>[38]</sup>. The mode of coordination of urea with metal ions seems to be dependent upon the type and nature of metal. Pd(II) ions in

$[\text{Pt}(\text{urea})_2\text{Cl}_2]$  coordinate to the nitrogen, whereas Fe(III), Zn(II), and Cu(II) coordinate to the oxygen of urea<sup>[38]</sup>. The distinguished bands of  $\nu(\text{C}-\text{N})$  are exhibited at lower wave numbers in the spectra of  $\text{AgNO}_3 \cdot 2\text{U} \cdot 6\text{CH}_3\text{OH}$  (1) and  $\text{AgNO}_3 \cdot 2\text{U} \cdot \text{CH}_3\text{OH}$  (2) complexes than for free urea, whereas the  $\nu(\text{C}=\text{O})$  band shows a frequency at the same wave number of free urea. These shifts are consistent with nitrogen coordination, suggesting the presence of  $+\text{N}=\text{C}-\text{O}^-$  resonance features<sup>[51]</sup>, see Scheme 3.



Concerning  $\text{CrCl}_3 \cdot 2\text{U} \cdot 12\text{H}_2\text{O}$  (**4**),  $\text{CrCl}_3 \cdot 4\text{U} \cdot 9\text{H}_2\text{O}$  (**5**),  $\text{CdCl}_2 \cdot 2\text{U} \cdot \text{H}_2\text{O}$  (**7**),  $\text{CdCl}_2 \cdot 4\text{U} \cdot \text{H}_2\text{O}$  (**8**),  $\text{ZnCl}_2 \cdot 4\text{U} \cdot 4\text{H}_2\text{O}$  (**10**) and  $\text{ZnCl}_2 \cdot 2\text{U} \cdot 6\text{H}_2\text{O}$  (**11**) complexes, the coordination mode takes place *via* oxygen of amide group, the positively charged metal ion stabilizes the negative charge on the oxygen atom; the NCO group now occurs in its polar resonance form and the double bond character of the CN bond increases or is still not affected, while the double bond character of the CO bond decreases, resulting in an increase of the CN stretching frequency with a simultaneous decrease in the CO stretching frequency<sup>[52,53]</sup>.

The band related to the stretching vibration  $\nu(\text{O-H})$  of uncoordinated  $\text{H}_2\text{O}$  is observed as expected in the range of  $(3400 \sim 3450) \text{ cm}^{-1}$ , while the corresponding bending motion of the uncoordinated water,  $\delta(\text{H}_2\text{O})$ , is observed in the range of  $(1630 \sim 1638) \text{ cm}^{-1}$ .

In both silver complexes, the characteristic stretching vibrations of the nitrate group,  $\text{NO}_3^-$ , is observed at around  $(1385 \text{ cm}^{-1}$  and  $1160 \text{ cm}^{-1}$  attributed to  $\nu_{\text{as}}(\text{NO}_2)$  and  $\nu_{\text{s}}(\text{NO}_2)$ , respectively<sup>[54]</sup>. The stretching motion of  $\nu(\text{N=O})$  is observed at  $1475 \text{ cm}^{-1}$  as a strong band, while the bending motion of the type  $\delta(\text{NO}_2)$  are well resolved and observed at  $786$  as a medium band.

#### D. $^1\text{H-NMR}$ Spectral Analysis

$^1\text{H-NMR}$  data were assignment in parts per million (ppm), and they were referenced internally to the residual proton impurity in DMSO (dimethylsulfoxide). The  $^1\text{H-NMR}$  spectra of the  $\text{CdCl}_2 \cdot 2\text{U} \cdot \text{H}_2\text{O}$  (**7**),  $\text{CdCl}_2 \cdot 4\text{U} \cdot \text{H}_2\text{O}$  (**8**),  $\text{ZnCl}_2 \cdot 4\text{U} \cdot 4\text{H}_2\text{O}$  (**10**) and  $\text{ZnCl}_2 \cdot 2\text{U} \cdot 6\text{H}_2\text{O}$  (**11**) complexes (Fig. 4) are consistent with the suggested formulas, scheme 4. The  $^1\text{H-NMR}$  spectral data of Cd(II) and Zn(II) complexes were reported in Table 6.

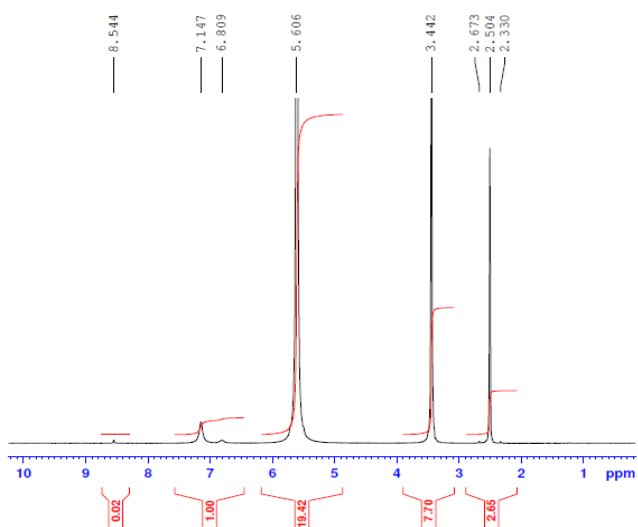


Fig. 4A  $^1\text{H-NMR}$  spectrum of  $\text{CdCl}_2 \cdot 2\text{U} \cdot \text{H}_2\text{O}$  (**7**) complex

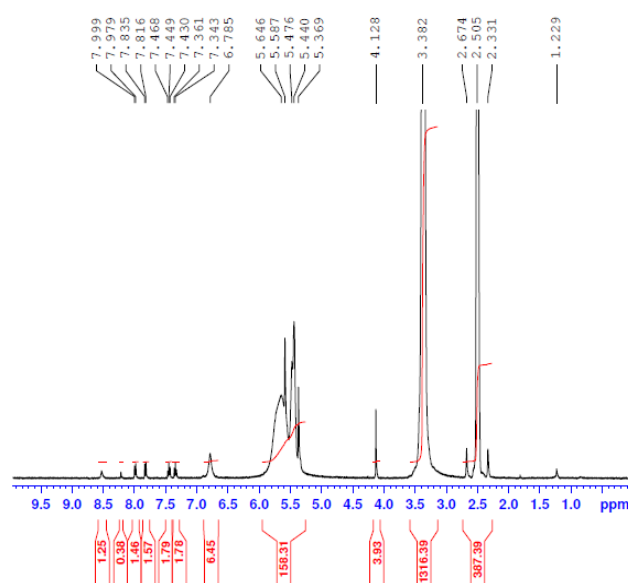


Fig. 4B  $^1\text{H-NMR}$  spectrum of  $\text{CdCl}_2 \cdot 4\text{U} \cdot \text{H}_2\text{O}$  (**8**) complex

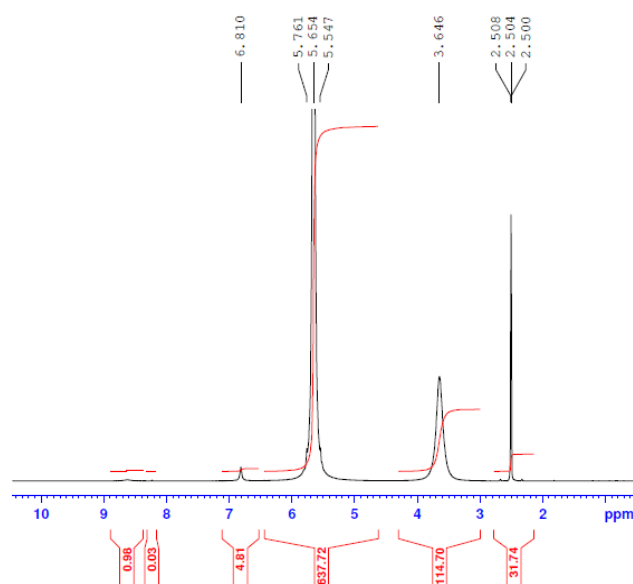


Fig. 4C  $^1\text{H-NMR}$  spectrum of  $\text{ZnCl}_2 \cdot 4\text{U} \cdot 4\text{H}_2\text{O}$  (**10**) complex

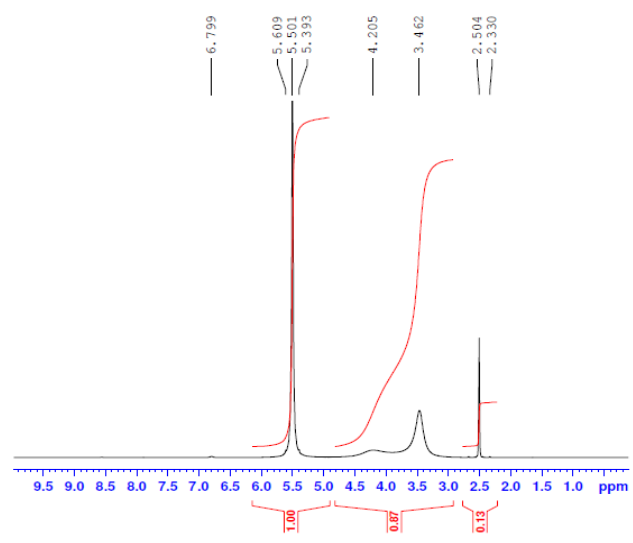
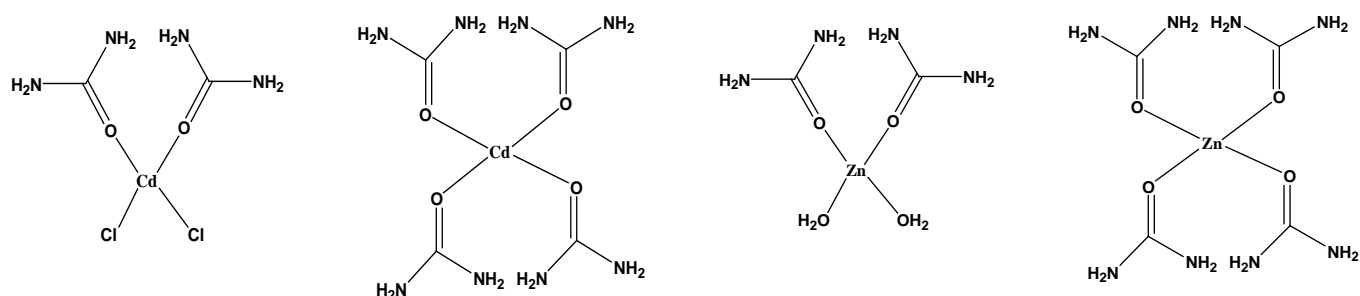


Fig. 4D  $^1\text{H-NMR}$  spectrum of  $\text{ZnCl}_2 \cdot 2\text{U} \cdot 6\text{H}_2\text{O}$  (**11**) complex



**Scheme 4** Suggested structure of Cd(II) and Zn(II) urea complexes (7, 8, 9 and 10)

**TABLE VI**  $^1\text{H-NMR}$  SPECTRAL BANDS (PPM) AND TENTATIVE ASSIGNMENTS OF  $\text{CdCl}_2 \cdot 2\text{U} \cdot \text{H}_2\text{O}$  (7),  $\text{CdCl}_2 \cdot 4\text{U} \cdot \text{H}_2\text{O}$  (8),  $\text{ZnCl}_2 \cdot 4\text{U} \cdot 4\text{H}_2\text{O}$  (10) AND  $\text{ZnCl}_2 \cdot 2\text{U} \cdot 6\text{H}_2\text{O}$  (11) COMPLEXES

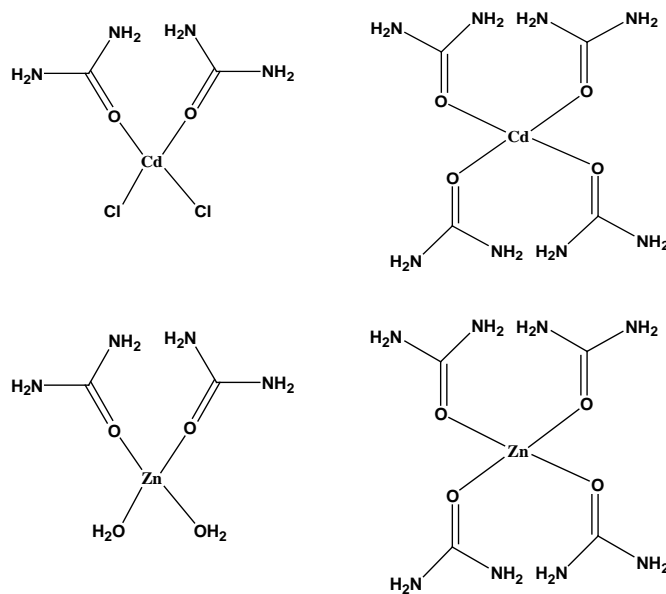
urea	ppm				Assignments (b)
	7	8	10	11	
5.600	3.442	4.128	3.646	3.462	□ ; -NH <sub>2</sub>
---	5.606–8.544	5.369–7.999	5.547–5.761	5.393–5.609	□ ; +NH <sub>2</sub>

In the free urea ligand, the only one peak at 5.6 ppm is assigned to (4H; 2NH<sub>2</sub>) four protons of two symmetric amino groups. Upon the complexation of Cd(II) and Zn(II) via oxygen atom and the resonance case in scheme 3, the discussion of the upfield and downfield status for the protons concerning -NH<sub>2</sub> group is due to the formation of new metal complexes chelating. Compared with the  $^1\text{H-NMR}$  spectrum data of pure urea, the  $^1\text{H-NMR}$  spectra of the Cd(II) and Zn(II) complexes exhibits two types of -NH<sub>2</sub> groups one of them neutral and the other one has a positively charged =<sup>+</sup>NH<sub>2</sub>, so the value of protons for -NH<sub>2</sub> group is appeared with upfield chemical shift at 3.442, 4.128, 3.646 and 3.462 ppm, for  $\text{CdCl}_2 \cdot 2\text{U} \cdot \text{H}_2\text{O}$  (7),  $\text{CdCl}_2 \cdot 4\text{U} \cdot \text{H}_2\text{O}$  (8),  $\text{ZnCl}_2 \cdot 4\text{U} \cdot 4\text{H}_2\text{O}$  (10) and  $\text{ZnCl}_2 \cdot 2\text{U} \cdot 6\text{H}_2\text{O}$  complexes, respectively. On the other hand, the protons of =<sup>+</sup>NH<sub>2</sub> group is downfield and presented at (5.606~8.544 ppm), (5.369~7.999 ppm), (5.547~6.810 ppm) and (5.393~6.799 ppm), respectively, for complexes 7, 8, 10 and 11. According to this result, it can be deduced that the electronic environments of the urea protons change with the formation of the new complexes.

#### E. Thermal Analysis

The  $\text{AgNO}_3 \cdot 2\text{U} \cdot 6\text{CH}_3\text{OH}$  (1),  $\text{AgNO}_3 \cdot 2\text{U} \cdot \text{CH}_3\text{OH}$  (2),  $\text{CrCl}_3 \cdot 2\text{U} \cdot 12\text{H}_2\text{O}$  (4),  $\text{CrCl}_3 \cdot 4\text{U} \cdot 9\text{H}_2\text{O}$  (5),  $\text{CdCl}_2 \cdot 2\text{U} \cdot \text{H}_2\text{O}$  (7),  $\text{CdCl}_2 \cdot 4\text{U} \cdot \text{H}_2\text{O}$  (8),  $\text{ZnCl}_2 \cdot 4\text{U} \cdot 4\text{H}_2\text{O}$  (10), and

$\text{ZnCl}_2 \cdot 2\text{U} \cdot 6\text{H}_2\text{O}$  (11) complexes were studied by thermogravimetric analysis from ambient temperature to 800°C in oxygen atmosphere. Figures 5A-D and 6A-D and Tables 7 and 8 illustrate TG curves and decomposition stages obtained for these complexes with a temperature rate 30°C/min.



**Scheme 4:** Suggested structure of Cd(II) and Zn(II) urea complexes (7, 8, 9 and 10)

**TABLE VII** THE MAXIMUM TEMPERATURE,  $T_{\text{MAX}}$ /°C, AND WEIGHT LOSS VALUES OF THE DECOMPOSITION STAGES FOR THE  $\text{AgNO}_3 \cdot 2\text{U} \cdot 6\text{CH}_3\text{OH}$  (1),  $\text{CrCl}_3 \cdot 2\text{U} \cdot 12\text{H}_2\text{O}$  (4),  $\text{CdCl}_2 \cdot 2\text{U} \cdot \text{H}_2\text{O}$  (7), AND  $\text{ZnCl}_2 \cdot 4\text{U} \cdot 4\text{H}_2\text{O}$  (10) COMPLEXES

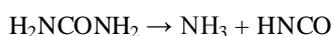
Complexes	Decomposition	$T_{\text{max}}$ /°C	Lost species	% Weight loss	
				Found	Calc.
1	First step	237	6CH <sub>3</sub> OH	39.14	39.84
	Second step	299	NO <sub>3</sub>	12.49	12.86
	Third step	381	Urea	11.08	12.44
	Fourth step	492	CH <sub>4</sub> + N <sub>2</sub>	10.55	9.13
	Residue		AgO	26.73	25.73
4	First step	123	2H <sub>2</sub> O	7.69	7.28

	Second step	207	2.5H <sub>2</sub> O	8.34	9.10
	Third step	273	6H <sub>2</sub> O+3HCl	41.94	43.98
	Fourth step	509	2Urea	24.63	24.26
	Residue		CrO <sub>1.5</sub>	17.39	15.37
7	First step	252	Cl <sub>2</sub> +H <sub>2</sub> O	28.04	27.70
	Second step	317, 404, 656	2Urea	37.39	37.34
	Residue		Cd metal	34.57	34.98
10	First step	244	4H <sub>2</sub> O+Cl <sub>2</sub> +Urea	44.48	45.28
	Second step	354, 561	3Urea	40.74	40.15
	Residue		Zn metal	14.77	14.59

TABLE VIII THE MAXIMUM TEMPERATURE, T<sub>MAX</sub>/°C, AND WEIGHT LOSS VALUES OF THE DECOMPOSITION STAGES FOR THE AgNO<sub>3</sub>.2U.CH<sub>3</sub>OH (2), CrCl<sub>3</sub>.4U.9H<sub>2</sub>O (5), CdCl<sub>2</sub>.4U.H<sub>2</sub>O (8) AND ZnCl<sub>2</sub>.2U.6H<sub>2</sub>O (11) COMPLEXES

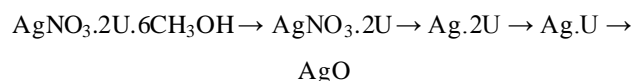
Complexes	De composition	T <sub>max</sub> /°C	Lost species	% Weight loss	
				Found	Calc.
2	First step	149	CH <sub>3</sub> OH	8.17	9.94
	Second step	243, 297, 384	Urea + NO <sub>3</sub>	37.38	37.90
	Third step	495	Urea	20.42	18.64
	Residue		Ag	34.24	33.55
5	First step	234	7.5H <sub>2</sub> O+3HCl+4Urea	83.55	82.15
	Residue		CrO <sub>1.5</sub>	16.45	17.85
8	First step	213	Urea + H <sub>2</sub> O	17.22	17.66
	Second step	275	Urea + ½Cl <sub>2</sub>	19.50	21.63
	Third step	373	Urea	13.42	13.60
	Fourth step	690	Urea + ½Cl <sub>2</sub>	47.15	47.11
	Residue		Contaminated carbon	2.71	---
11	First step	95	2.5H <sub>2</sub> O	11.79	12.35
	Second step	239	1.5H <sub>2</sub> O+Cl <sub>2</sub> +2H <sub>2</sub> O	37.34	36.78
	Third step	349	Urea	15.05	16.47
	Fourth step	563	Urea + loss Zn metal	28.29	26.87
	Residue			7.53	7.53

Thermal analysis of AgNO<sub>3</sub>.2U.6CH<sub>3</sub>OH (1) complex (Fig. 5A) shows that the silver(I) complex prepared at room temperature is thermally stable up to 145°C. Its thermal decomposition occurs in four stages of weight loss of different intermediates followed by four endothermic maximum temperatures DTG<sub>max</sub> = 237, 299, 381 and 492°C, respectively. From the TG-DTG curves it is clear that the first decomposition stage from 145 to 279°C corresponds to the loss of six methanol molecules (39.14% experimental loss; 39.84% theoretical loss). The continued loss, decomposition steps second and third up to 416°C corresponds to the complete decomposition of the nitrate, NO<sub>3</sub><sup>-</sup>, and one urea molecules (12.49% experimental loss; 12.86% theoretical loss) and (11.08% experimental loss; 12.44% theoretical loss) followed by endothermic DTG<sub>max</sub> at 299°C and 381°C, respectively. The most probable thermal decomposition of urea from the complex may be represented as:



As the temperature is raised to 596°C, the complete loss of second urea molecule (10.55% experimental loss; 9.13% theoretical loss) and conversion to silver(I) oxide. Based on the results of thermal analysis of residual

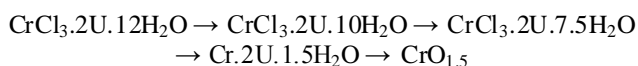
supported by the infrared spectra (Fig. 3), XRD, EDX and SEM measurements, the mechanism of the thermal decomposition of the complex is proposed as:



The TG curve of the AgNO<sub>3</sub>.2U.CH<sub>3</sub>OH complex has a three stages of the dissociation of complex are indicated in TG and DTG curve. The decomposition starts from 43°C and ends at 201°C, the mass loss experimentally is 8.17% against theoretically 9.94%, corresponding to the release of 1 mol of methanol. The second stage is a wide scale that started from 201 to 420°C with three DTG<sub>max</sub> = 243, 297 and 384°C, respectively. The mass loss experimentally is 37.38% against theoretical 37.90%, showing that 1 mol urea and NO<sub>3</sub><sup>-</sup> ion is liberated. The third stage is in continuation with the second stage from 420 to 489°C with maximum peak at 495°C. The experimental mass loss is 20.42% against theoretical mass loss of 18.64%, corresponding to the dissociation of 1 mol of urea. The residual product is silver metal, comparable with the final decomposition product of AgNO<sub>3</sub>.2U.6CH<sub>3</sub>OH which gave silver(I) oxide at the final decomposition stage, that we can discuss this

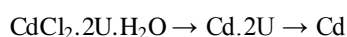
differentiate according to the solvent effect. The product of thermal decomposition was analyzed by the infrared and X-ray powder diffraction measurement.

The TG-DTG curve of  $\text{CrCl}_3 \cdot 2\text{U} \cdot 12\text{H}_2\text{O}$  (4) complex indicates the dissociation of complex in four stages. The first transition changes from 42 to 166°C, and the experimental mass loss is 7.69% against the theoretical mass loss of 7.28%, corresponding to the release of 2 mol of water. The second transformation is from 166 to 237°C, and the mass loss experimental is 8.34% against the theoretical loss of 9.10%, due to the release of 2.5 mol of water. The third stage is in continuation with the second stage from 237 to 480°C. The mass loss experimentally is 41.94% against theoretical mass loss of 43.98%, corresponding to the dissociation of 6 mol of water and 3 mol HCl. The fourth stage is from 480 to 563°C. The experimental mass loss is 17.39%, showing that 2 urea are dissociated. The experiment result is matched with theoretical value. The final product is considered to be  $\text{CrO}_{1.5}$ . The thermo analytical data for  $\text{CrCl}_3 \cdot 2\text{U} \cdot 12\text{H}_2\text{O}$  (4) complex are also given in Table 7. All transitions in DTG curve corresponding to the transition are observed in the TG curve and recorded at  $\text{DTG}_{\text{max}} = 123, 207, 273$  and  $509^\circ\text{C}$ , respectively. The final decomposition step led to formed chromium oxide  $\text{Cr}_2\text{O}_3$ . The sequential thermal dissociation process of the complex is shown as follows:



The thermoanalytical data for  $\text{CrCl}_3 \cdot 4\text{U} \cdot 9\text{H}_2\text{O}$  complex are listed in Table 8. There is one very strong endothermic peak in DTG curve corresponding to the chemical events observed in the TG curve. Weight loss in the range of 39 to 270 °C with  $\text{DTG}_{\text{max}} = 234^\circ\text{C}$  is experimental to be 83.55% which is close to theoretical value 82.15%, indicating loss of 7.5 mol of water, 4 mol of urea and 3 mol of HCl. At 270°C weight of residual  $\text{Cr}_2\text{O}_3$  oxide polluted with carbon atoms was experimental to be 16.45% which is close to theoretical value 17.84%. The final thermal decomposition was checked using IR, XRD, SEM and EDX measurements.

The TG-DTG curve of  $\text{CdCl}_2 \cdot 2\text{U} \cdot \text{H}_2\text{O}$  complex has two stages the transitions observed in the TG-DTG curve. The first transition changes from 167 to 293°C with  $\text{DTG}_{\text{max}} = 252^\circ\text{C}$ , and the experimental mass loss is 28.04% against the theoretical loss of 27.70%, corresponding to the release of 1 mol of water and 1 mol of  $\text{Cl}_2$ . The second transition stage is a large scale which started from 293 to 713°C, with three  $\text{DTG}_{\text{max}}$  at 317, 404 and 656°C. The experimental mass loss is 37.39% against the theoretical mass loss of 37.34%, due to the release of 2 mol of urea. The final product is considered to be Cd metal. The disturbed in the arrangement of the decomposition stages back to the lower melting and boiling points of cadmium metal which occurs at 321°C and 767°C, respectively. The sequential thermal dissociation process of the complex is shown as follows:



$\text{CdCl}_2 \cdot 4\text{U} \cdot \text{H}_2\text{O}$  complex: in the range of 135-766°C, four  $\text{DTG}_{\text{max}}$  at 213°C, 275°C, 373°C and 690°C with four mass loss stages are exhibited. The Table 8 summarized the thermoanalytical and weight loss obtained data. The thermal transformation starts with an endothermic peak existing on DTG curve with  $\text{max} = 213^\circ\text{C}$ . This stage of decomposition corresponds to experimental mass loss of 17.22%, which can be attributed to the loss of one urea ligand and the decomposition of 1 mol water. The second stage with experimental mass loss of 19.50% and theoretical mass loss of 21.64% may result from decomposition of the 1 mol urea and half mol of chlorine gas. The third and fourth decomposition stages amount to a total experimental mass loss of 60.57% with theoretical mass loss of 60.71%, which assigned to the loss of 2 urea and half chlorine molecules. The decline in output of the final product was discussed according the previous notification concerning the lower melting and boiling points of cadmium metal.

The zinc(II) urea complex which was prepared at room temperature,  $\text{ZnCl}_2 \cdot 4\text{U} \cdot 4\text{H}_2\text{O}$ , shows two main stages of decomposition as is evident from DTG peaks at 244°C and (354°C and 561°C), and is thermally stable up to 127°C. The first stage of decomposition with experimental mass loss of 44.48% and theoretical mass loss of 45.28% may be assigned to the decomposition of 4 mol water, 1 mol  $\text{Cl}_2$  and 1 mol urea. The second stage, amounting to experimental mass loss of 40.74% in good agreement with theoretical mass loss of 40.15% , may be attributed to the loss of the remaining three urea ligand molecules, resulting in the final residue of zinc metal.

The TG curve for  $\text{ZnCl}_2 \cdot 2\text{U} \cdot 6\text{H}_2\text{O}$  complex has three stages of mass losses within the temperature range of 29-653°C at 95°C, 239°C, 349°C and 563°C DTG maximum peaks. The first stage at 29-151°C with experimental mass loss of 11.79% (theoretical: 12.35% ) corresponds to the loss of 2.5  $\text{H}_2\text{O}$  molecules. The second stage at 151-311°C with experimental mass loss of 37.34% (theoretical: 36.78%) corresponds to the loss of 3.5 $\text{H}_2\text{O}$  and  $\text{Cl}_2$  molecules. The third stage of decomposition at the temperature range of 311-467°C is assigned to the loss of one molecule of urea ligand with experimental mass loss of 15.05% (theoretical: 16.47% ). The fourth decomposition stage is distorted, which may be assigned to decomposition of the second urea molecule and loss a part of zinc metal, so the experimental mass loss shifted to higher percentage of 28.29% than expected value of 16.47%. This can be explained through the formation of zinc(II) chloride as an intermediate which has a low melting and boiling degrees at 292°C and 756°C.

To clarify the final decomposition products of urea complexes, the solid residues after thermal degradation under oxygen atmosphere were collected at 800°C and were analyzed by infrared spectroscopy, X-ray diffractometry, EDX and SEM.

#### F. X-ray Powder Diffraction Studies

The x-ray powder diffraction patterns for the Ag(I), Cr(III), Cd(II) and Zn(II) urea at different temperatures with

formulas;  $\text{AgNO}_3 \cdot 2\text{U} \cdot 6\text{CH}_3\text{OH}$  (1),  $\text{AgNO}_3 \cdot 2\text{U} \cdot \text{CH}_3\text{OH}$  (2) and Ag metal (3),  $\text{CrCl}_3 \cdot 2\text{U} \cdot 12\text{H}_2\text{O}$  (4),  $\text{CrCl}_3 \cdot 4\text{U} \cdot 9\text{H}_2\text{O}$  (5) and  $\text{Cr}_2\text{O}_3$  (6),  $\text{CdCl}_2 \cdot 2\text{U} \cdot \text{H}_2\text{O}$  (7),  $\text{CdCl}_2 \cdot 4\text{U} \cdot \text{H}_2\text{O}$  (8) and  $\text{CdO}$  (9) and  $\text{ZnCl}_2 \cdot 4\text{U} \cdot 4\text{H}_2\text{O}$  (10),  $\text{ZnCl}_2 \cdot 2\text{U} \cdot 6\text{H}_2\text{O}$  (11) and  $\text{ZnO}$  (12) are depicted in Fig. 7A-D. Inspecting these patterns, we notice that all systems are well crystalline except for diagrams of silver(I) complex at 800 °C and  $\text{CdCl}_2 \cdot 2\text{U} \cdot \text{H}_2\text{O}$  complex. The crystallite size of these complexes could be estimated from XRD patterns by applying FWHM of the characteristic peaks using Debye-Scherrer Equation 1<sup>[55]</sup>. Where D is the particle size of the crystal grain, K is a constant (0.94 for Cu grid),  $\lambda$  is the x-ray wavelength (1.5406Å),  $\theta$  is the Bragg diffraction angle and  $\beta$  is the integral peak width. The particle size was estimated according to the highest value of intensity compared with the other peaks. These data gave an impression that the particle size located within nano scale range.

$$D = K\lambda / \beta \cos\theta \quad (1)$$

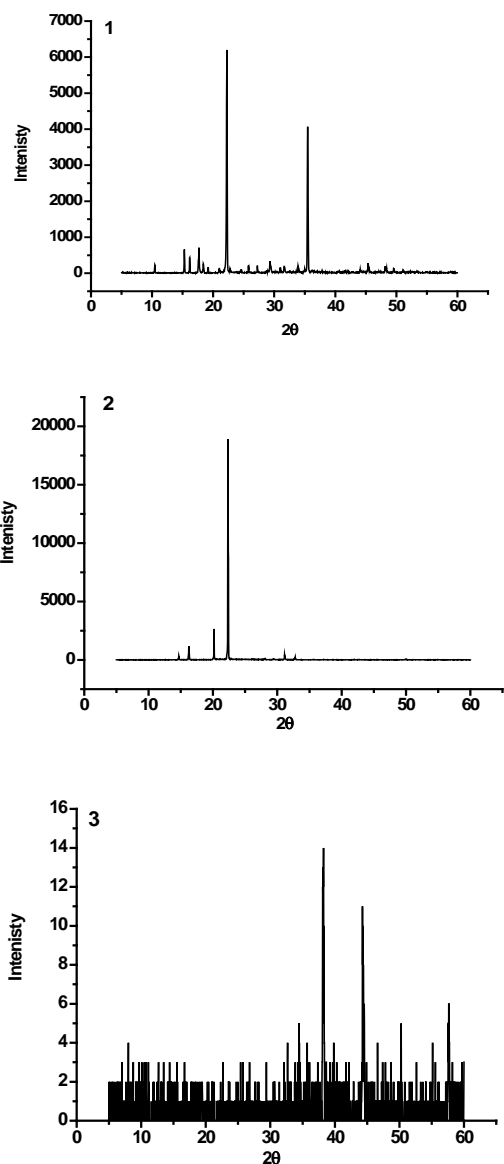


Fig. 7A XRD spectra of the compounds resulted from the reaction of silver(I) nitrate with urea at room (1), 60 °C (2) and 800 °C (3) temperatures

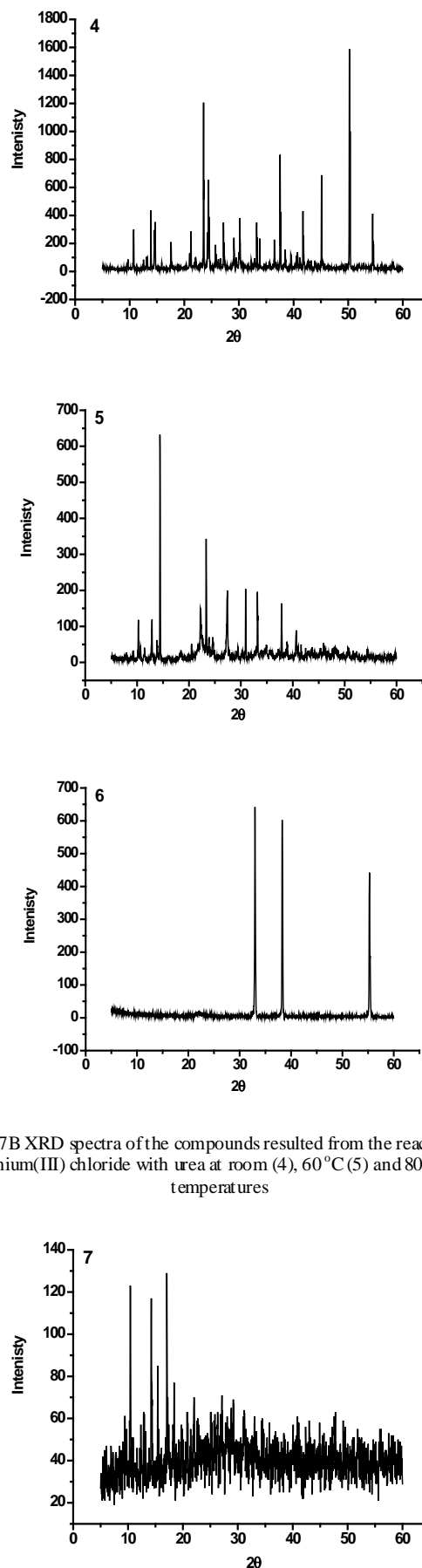


Fig. 7B XRD spectra of the compounds resulted from the reaction of chromium(III) chloride with urea at room (4), 60 °C (5) and 800 °C (6) temperatures

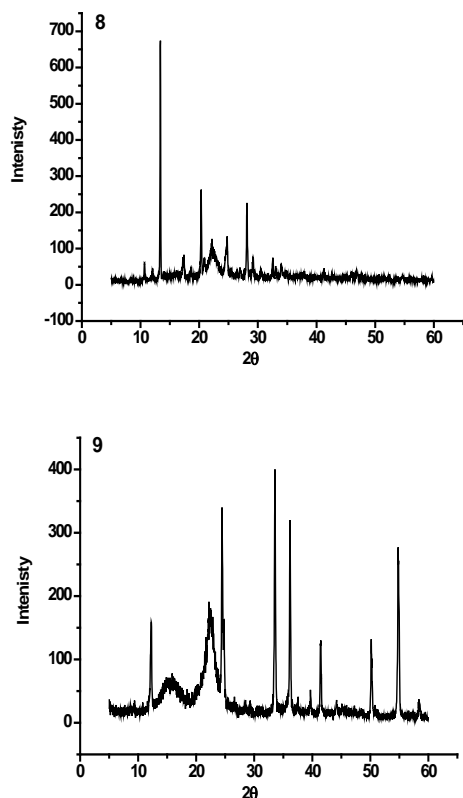


Fig. 7C XRD spectra of the compounds resulted from the reaction of cadmium(II) chloride with urea at room (7), 60 °C (8) and 800 °C (9) temperatures

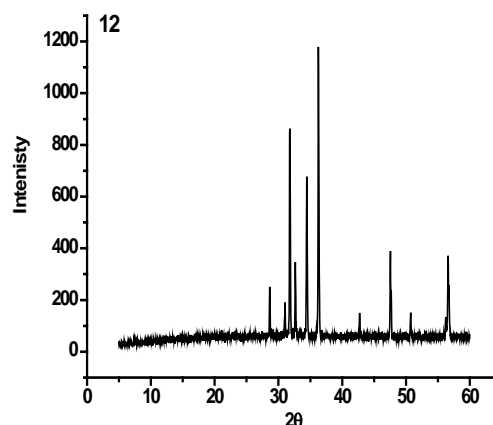
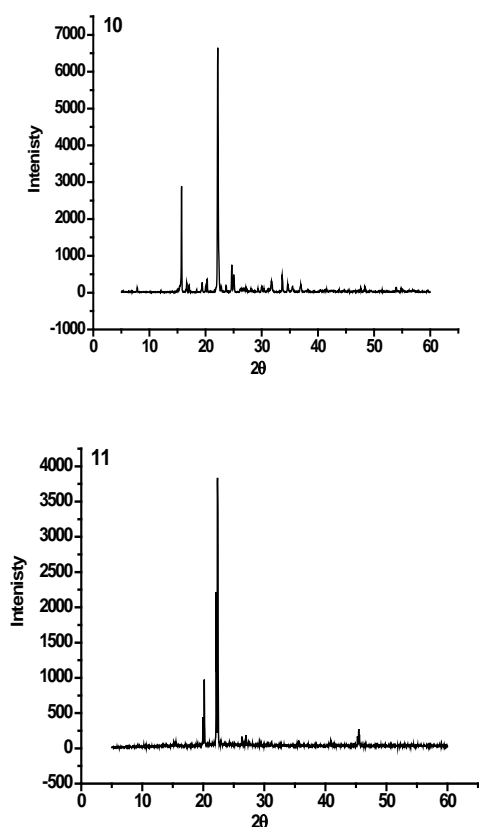


Fig. 7D XRD spectra of the compounds resulted from the reaction of zinc(II) chloride with urea at room (10), 60 °C (11) and 800 °C (12) temperatures

### G. SEM and EDX Studies

Scanning electron microscopy is a simple tool used to give an impression about the microscopic aspects of the physical behavior of urea as a chelating agent (Figs. 8A-D). Although this tool is not a qualified method to confirm complex formation but it can be a reference to the presence of a single component in the synthetic complexes. The pictures of the Ag(I), Cr(III), Cd(II) and Zn(II) complexes show a small particle size with a nano feature products. The chemical analysis results by EDX for the formed complexes show a homogenous distribution in between metal ions and chelating agent. SEM examinations were checked the morphology of the surfaces of these complexes that show small particles which tend to agglomerates formation with different shapes comparison with the start materials. The peaks of EDX profile of these complexes (Figs. 9A-D) refer to all elements which constitute the molecules of urea complexes (1-to-12) that clearly identified confirming the proposed structures

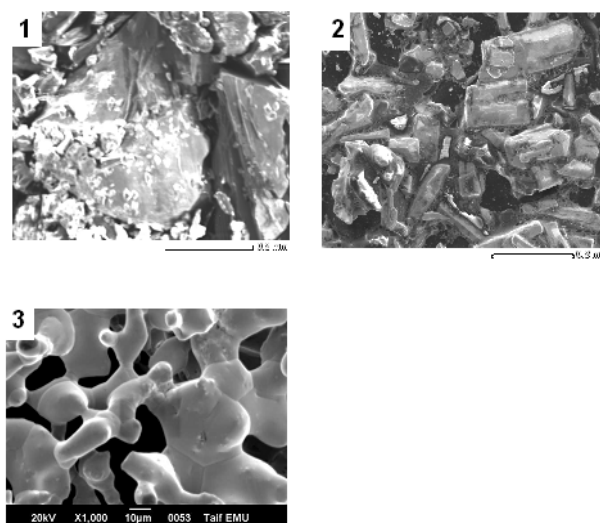


Fig. 8A SEM image of the compounds resulted from the reaction of silver(I) nitrate with urea at room (1), 60 °C (2) and 800 °C (3) temperatures

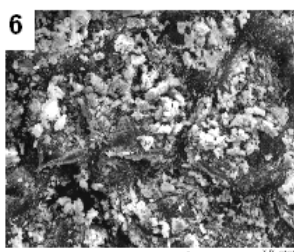
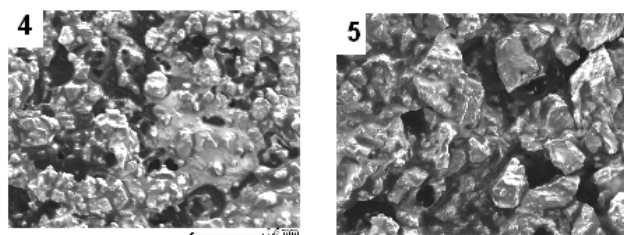


Fig. 8B SEM image of the compounds resulted from the reaction of chromium(III) chloride with urea at room (4), 60 °C (5) and 800 °C (6) temperatures

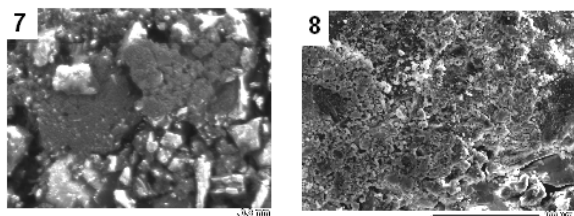


Fig. 8C SEM image of the compounds resulted from the reaction of cadmium(II) chloride with urea at room (7), 60 °C (8) and 800 °C (9) temperatures

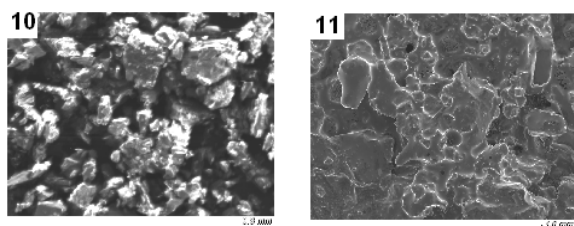
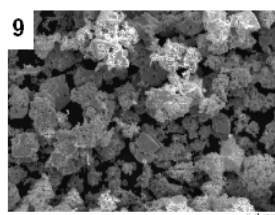


Fig. 8D SEM image of the compounds resulted from the reaction of zinc(II) chloride with urea at room (10), 60 °C (11) and 800 °C (12) temperatures

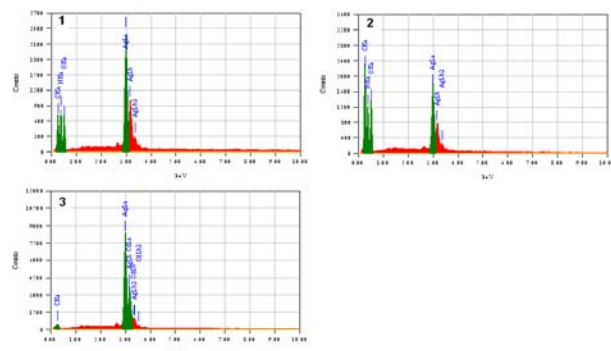
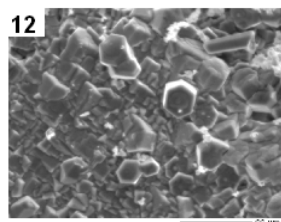


Fig. 9A EDX diagram of the compounds resulted from the reaction of silver(I) nitrate with urea at room (1), 60 °C (2) and 800 °C (3) temperatures

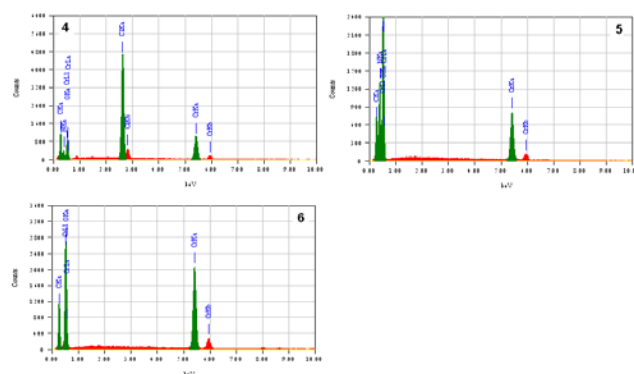


Fig. 9B EDX diagram of the compounds resulted from the reaction of chromium(III) chloride with urea at room (4), 60 °C (5) and 800 °C (6) temperatures

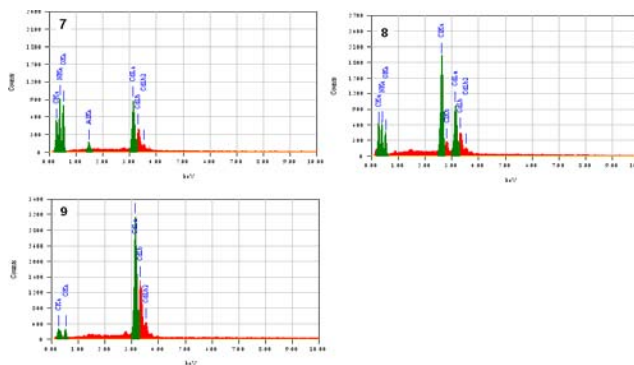


Fig. 9C EDX diagram of the compounds resulted from the reaction of cadmium(II) chloride with urea at room (7), 60 °C (8) and 800 °C (9) temperatures

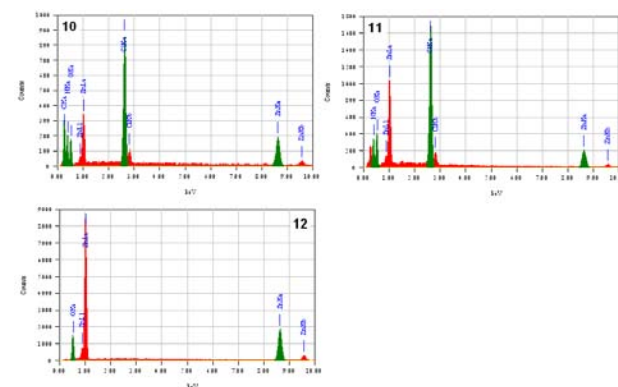


Fig. 9D EDX image of the compounds resulted from the reaction of zinc(II) chloride with urea at room (10), 60 °C (11) and 800 °C (12) temperatures

### H. Biological Evaluation

Biological evaluations were checked in term of antimicrobial activities of target compounds against gram-positive (*Bacillus subtilis* and *Staphylococcus aureus*) and gram-negative (*Escherichia coli* and *Pseudomonas aeruginosa*) and tow strains of fungus (*Aspergillus flavus* and *Candida albicans*). Result from the agar disc diffusion tests for antimicrobial activities of target compounds are presented in Table 9, and illustrated in Fig. 10. The diameters of zone of inhibition (in mm) of the standard drug tetracycline against gram positive bacteria *B. subtilis* and *S. aureus* and gram negative bacteria *E. coli* and *P. aeruginosa*

were found to be 36, 30, 31 and 35 mm, respectively, while the standard drug amphotericin B against *Aspergillus flavus* and *Candida albicans* gave 18 and 19, respectively. Under identical conditions, Table 9 shows that, Complex 1 has (14, 12, 12, 15, 0.0 and 0.0 mm), Complex 4 has (12, 16, 11, 12, 0.0 and 0.0 mm), Complex 7 has (24, 21, 23, 21, 18 and 12 mm), and Complex 10 has (19, 23, 26, 24, 0.0 and 0.0 mm), respectively, for *Bacillus subtilis*, *Escherichia coli*, *Pseudomonas aeruginosa*, *Staphylococcus aureus*, *Aspergillus flavus* and *Candida albicans*. All complexes were found to be efficiency antimicrobial agents except for 1, 4, and 10 complexes have no efficiency against *Aspergillus flavus* and *Candida albicans* fungus.

TABLE IX INHIBITION ZONE DIAMETER (MM) OF THE TARGET COMPOUNDS AGAINST TESTED MICROORGANISMS FOR  $\text{AgNO}_3 \cdot 2\text{U} \cdot 6\text{CH}_3\text{OH}$  (1),  $\text{CrCl}_3 \cdot 2\text{U} \cdot 12\text{H}_2\text{O}$  (4),  $\text{CdCl}_2 \cdot 2\text{U} \cdot \text{H}_2\text{O}$  (7), AND  $\text{ZnCl}_2 \cdot 4\text{U} \cdot 4\text{H}_2\text{O}$  (10) COMPLEXES

Sample	Inhibition Zone Diameter (Mm /Mg Sample)					
	<i>Bacillus Subtilis</i> (G <sup>+</sup> )	<i>Escherichia Coli</i> (G <sup>-</sup> )	<i>Pseudomonas Aeruginosa</i> (G <sup>-</sup> )	<i>Staphylococcus Aureus</i> (G <sup>+</sup> )	<i>Aspergillus Flavus</i> (Fungus)	<i>Candida Albicans</i> (Fungus)
Control: DMSO	0.0	0.0	0.0	0.0	0.0	0.0
Antibacterial agent (Tetracycline)	36	31	35	30	--	--
Antifungal agent (Amphotericin B)	--	--	--	--	18	19
1	14	12	12	15	0.0	0.0
4	12	16	11	12	0.0	0.0
7	24	21	23	21	18	12
10	19	23	26	24	0.0	0.0

G: Gram reaction.

Solvent: DMSO.

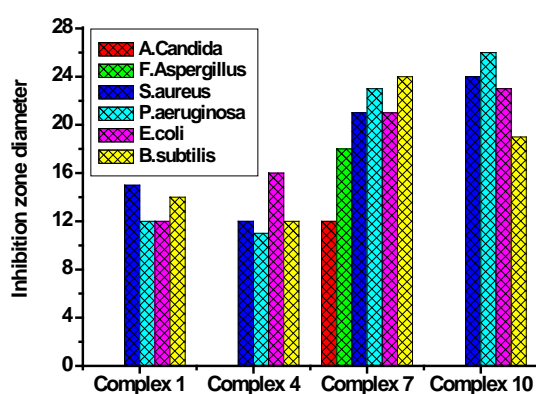


Fig. 10 Biological evaluation diagram of  $\text{AgNO}_3 \cdot 2\text{U} \cdot 6\text{CH}_3\text{OH}$  (1),  $\text{CrCl}_3 \cdot 2\text{U} \cdot 12\text{H}_2\text{O}$  (4),  $\text{CdCl}_2 \cdot 2\text{U} \cdot \text{H}_2\text{O}$  (7), and  $\text{ZnCl}_2 \cdot 4\text{U} \cdot 4\text{H}_2\text{O}$  (10) complexes

### REFERENCES

- [1] Wöhler, Ann. Physik, 12 (1828) 253.
- [2] Jr. Tonn, Chem. Eng., 62 (1955) 186.
- [3] P. Moore, Chem. & Eng. News, 37 (1959) 84.
- [4] A. Franz, J. Org. Chem., 26 (1961) 3304.

- [5] D. Feldman, A. Barbalata, "Synthetic Polymers", Chapman & Hall, London (1996).
- [6] I. L. Finar, "Organic Chemistry", Longman group limited, London (1973) P. 460.
- [7] M. J. Rahman, P. Bozadjiev and Y. Polovski, fert. Res., 38(2) (1994) 89.
- [8] S. George, M. Chellapandian, B. Sivasankar, K. Jayaraman, Bioprocess Eng., 16(2) (1997) 83.
- [9] X. J. Wang, L.A. Douglas, Agrochimica, 40(5-6) (1996) 209.
- [10] O. A. Yerokun, S. Afr. J. plant soil, 14(2) (1997) 63.
- [11] R. Heinig, SOFW J., 122(14) (1996) 998.
- [12] C. T. Gnewuch, G. Sosnovsky, Chem. Rev., 97(3) (1997) 829.
- [13] C. I. Miyagawa, Drug Intell. & Clin. Pharma., 20 (1986) 527.
- [14] E. Kissa, Text. Res. J., 39(8) (1969) 734.
- [15] I. Srinivasa, K. Vishivanathapuram, M. B. Mishra, S. K. Ghosh, Technology, 7(12) (1970) 27.
- [16] I. M. Kaganskii, A. M. Babenko, Zh. Prikl. Khim., 43(11) (1970) 2390.
- [17] Y. Zhang, J. Bai, T. Wei, A. Lu, Huaxue Shijie, 37(4) (1996) 178.
- [18] Y.K. Kim, J.W. Williard, A.W. Frazier, J. Chem. Eng. Data, 33(3) (1988) 306.
- [19] Hu. Chuncong, Chem. Abs., 113, 888 (1990).
- [20] A.D. Pandey, L. Singh, R. Yadav, K. M. Varma, Chem. Abs., 118 (1993) 607.

- [21] A. Crispoldi, *Chem. Abs.*, 119 (1993) 831.
- [22] M. Sugimura, Y. Kameyama, T. Hashimoto, T. Kobayashi, S. Muramatsu. *Chem. Abs.*, 112 (1990) 63.
- [23] P. S. Gentile, P. Carfagno, S. Haddad, L. Campisi, *Inorg. Chim. Acta*, 6(C) (1972) 296.
- [24] D. S. Sagatys, R. C. Bott, G. Smith, K. A. Byriel, C. H. L. Kennard, *Polyhedron*, 11(1) (1992) 49.
- [25] K. Lewinski, J. Sliwinski, L. Lebioda, *Inorg. Chem.*, 22(16) (1983) 2339.
- [26] S. V. Kryatov, A. Y. Nazarenko, P. D. Robinson, E. V. Rybak-Akimova, *Chemical Communications*, 11 (2000) 921.
- [27] T. J. Bhoopathy, M. Baskaran, S. Mohan, *Indian J. Phys.*, 62 B (1) (1988) 47.
- [28] A. Yamaguchi, R. B. Penland, S. Mizushima, T. J. Lane, Columba Curran, J. V. Quagliano, *J. Amer. Chem. Soc.*, 80 (1958) 527.
- [29] J. L. Duncan, *Spectrochim. Acta, Part A*, 27 (1970) 1197.
- [30] G. B. Aitken, J. L. Duncan, G. P. Mc Quillan, *J. Chem. Soc. A*, 2695, (1971).
- [31] D. Hadzi, J. Kidric, Z. V. Knezevic, B. Barlic, *Spectrochim. Acta, Part A*, 32 (1976) 693.
- [32] Sib Sankar Bala, Pradip N. Ghosh, *J. Mol. Str.*, 101 (1983) 69.
- [33] L. Kellner, *Proc. Roy. Soc.*, A 177 (1941) 456.
- [34] R. D. Waldron, R. M. Badger, *J. Chem. Phys.*, 18 (1950) 566.
- [35] E. R. Andrew, D. Hyndman, *Proc. Phys. Soc.*, A 66 (1953) 1187.
- [36] A. Yamaguchi, T. Miyazawa, T. Shimanouchi, S. Mizushima, *Spectrochim. Acta*, 10 (1957) 170.
- [37] J. E. Stewart, *J. Chem. Phys.*, 26 (1957) 248.
- [38] R. B. Penland, S. Mizushima, C. Curran, J. V. Quagliano, *J. Amer. Chem. Soc.*, 79 (1957) 1575.
- [39] G. F. Svatos, C. Curran, J. V. Quagliano, *This Journal*, 77 (1965) 6159.
- [40] W. F. Boron and E. L. Boulpaep, *Medical Physiology*, Updated Edition, Saunders, Philadelphia, Pa, USA, 2004.
- [41] J. H. Meessen and H. Petersen, "Urea," in *Ullmann's Encyclopedia of Industrial Chemistry*, Electronic Release, Wiley-VCH, Weinheim, Germany, 6th edition, 2002.
- [42] A.W. Bauer, W.M. Kirby, C. Sherris, M. Turck, *Amer. J. Clinical Pathology*, 45 (1966) 493.
- [43] M.A. Pfaller, L. Burmeister, M.A. Bartlett, M.G. Rinaldi, *J. Clin. Microbiol.* 26 (1988) 1437.
- [44] National Committee for Clinical Laboratory Standards, *Performance Vol. antimicrobial susceptibility of Flavobacteria*, 1997.
- [45] National Committee for Clinical Laboratory Standards. 1993. *Methods for dilution antimicrobial susceptibility tests for bacteria that grow aerobically*. Approved standard M7-A3. National Committee for Clinical Laboratory Standards, Villanova, Pa.
- [46] National Committee for Clinical Laboratory Standards. (2002). *Reference Method for Broth Dilution Antifungal Susceptibility Testing of Conidium-Forming Filamentous Fungi: Proposed Standard M38-A*. NCCLS, Wayne, PA, USA.
- [47] National Committee for Clinical Laboratory Standards. (2003). *Methods for Antifungal Disk Diffusion Susceptibility Testing of Yeast: Proposed Guideline M44-P*. NCCLS, Wayne, PA, USA.
- [48] L.D. Liebowitz, H.R. Ashbee, E.G.V. Evans, Y. Chong, N. Mallatova, M. Zaidi, D. Gibbs, and Global Antifungal Surveillance Group. 2001. *Diagn. Microbiol. Infect. Dis.* 4, 27.
- [49] M.J. Matar, L. Ostrosky-Zeichner, V.L. Paetznick, J.R. Rodriguez, E. Chen, J.H. Rex, 2003. *Antimicrob. Agents Chemother.*, 47, 1647.
- [50] A. Earnshaw, "Introduction to Magnetochemistry" Academic press, London and New York, pp. 35, 1968.
- [51] R. Keuleers, H.O. Desseyn, B. Rousseau, C. Van Alsenoy, *J. Phys. Chem. A*, 103(24) (1999) 4621.
- [52] E. Diamantopoulou, G.S. Papaefstatiou, A. Terzis, C.P. Raptopoulou, H.O. Desseyn, S. P. Perlepes, *Polyhedron*, 22 (2003) 825.
- [53] R. Keuleers, G.S. Papaefstathiou, C.P. Raptopoulou, S.P. Perlepes, H.O. Desseyn, *J. Mol. Str.*, 525(1-3) (2000) 173.
- [54] K. Nakamoto "Infrared and Raman Spectra of Inorganic and Coordination Compounds", Wiley, New York, 1978.
- [55] C.X. Quan, L.H. Bin, G.G. Bang. *Mater. Chem. Phys.* 91 (2005) 317.

# Synthesis and Characterization of Silver (Core)/Layered Double Hydroxide (Shell) Nanoparticles

Woo Noh, Xiaodi Sun, Aishwarya Ramachandran, Colton Rearick, Sandwip K. Dey\*

School for Engineering of Matter, Transport and Energy, Center for Interventional Biomaterials,  
Ira Fulton College of Engineering, Arizona State University, Tempe, AZ 85287, USA  
Sandwip.dey@asu.edu

**Abstract-**The development of metallic Silver (Ag) core and layered double hydroxide (LDH) shell nanoparticles (NPs) holds promise in nanomedicine. This drug delivery platform may induce simultaneous therapeutic actions, i.e., hyperthermia due to plasmon resonance of Ag and apoptosis due chemotherapeutic agent within LDH, as well as provide molecular imaging capability. Herein, for the first time, Ag (core)/(Mg<sup>2+</sup>, Al<sup>3+</sup>)-LDH (shell) NPs are synthesized, and the results of characterization of the morphology, composition and surface plasmon resonance (SPR) of the core/shell NPs with varying shell thickness are reported. For the pure 45 nm Ag NP core, the wavelength for transverse SPR absorption was 395 nm, which red-shifted up to 430 nm at a LDH shell thickness of 15 nm. Additionally, the synthesis and characterization of the Ag nanorods are also presented. The observation of longitudinal SPR absorption in the near infrared range makes Ag nanorods a more appropriate core material.

**Keywords-** Ag Core/LDH Shell Nanoparticles; Coprecipitation; Layered Double Hydroxide; Surface Plasmon Resonance; Theranostics

## I. INTRODUCTION

Nanomedicine exploits the high potential of nanotechnology with the progressive understanding of molecular and cellular biology by using platforms having combined therapeutic and diagnostic attributes (i.e., theranostics) for medical benefits. To date, some drug-loaded polymeric liposomes have already gained FDA approval [1], but inorganic nanostructures are also making their mark [2]. Quantum dot, silica, and magnetic nanoparticle (NP)-based theranostics are now in various stages of preclinical and clinical development [3]. Another inorganic ceramic which holds promise in nanomedicine is the layered double hydroxide (LDH), based on the Hydrotalcite (Mg<sub>6</sub>Al<sub>2</sub>(OH)<sub>16</sub>CO<sub>3</sub>·4H<sub>2</sub>O) structure. Here, the positively charged cation hydroxide layers are rendered electrically neutral by electrostatically-bound anions. The space between the octahedral-cation (e.g., divalent Mg<sup>2+</sup>, Co<sup>2+</sup>, Zn<sup>2+</sup> and trivalent Al<sup>3+</sup>, <sup>67</sup>Ga<sup>3+</sup>, Fe<sup>3+</sup>, Mn<sup>3+</sup>, Gd<sup>3+</sup> etc.) layers may be occupied by intercalated anions (e.g., nucleotides, fluorescent molecules, radio-labeled ATP, vitamins, DNA, and drugs), with water held in place via hydrogen bonding to the hydroxyls [4]. To date, one *in vivo* magnetic resonance imaging study [5] and a number of *in vivo* studies [6]-[10] using animal models to determine the pharmacokinetics, toxicity, transfection efficiency, and

therapeutic efficacy of LDH, have been reported. In order for this LDH platform to compete with polymeric and other inorganic theranostics, it is important to demonstrate the potential for additional modalities with respect to therapy and imaging, while maintaining structural simplicity and ease of processing of 100-200 nm NPs [5]. For example, combination therapy may be accomplished by (i) an apoptosis-inducing, chemotherapeutic agent intercalated within the interlayer space of the LDH nanoshell, and (ii) hyperthermic ablation of cancer cells via surface plasmon resonance (SPR) absorption in the near infrared (NIR) region (650–900 nm) [11] by synthesizing a LDH shell on a noble metal core as core/shell nanoparticles. Since the former, i.e., insertion of chemotherapeutic agents in phase-pure LDH, has been amply demonstrated; this article reports a preliminary step towards the fulfillment of the latter goal.

Recently, a few methods for the syntheses of submicron, ceramic magnetic core/LDH shell, particles have been reported. A tedious layer by layer adsorption of commercially available LDH nanosheets onto large Fe<sub>3</sub>O<sub>4</sub> core (500 nm) was used to synthesize submicron Fe<sub>3</sub>O<sub>4</sub> core/(Mg<sup>2+</sup>, Al<sup>3+</sup>)-LDH shell particles [12]. One post-synthetic mechanical processing method, such as ball milling, was used to reduce the particle size after the synthesis of micron-sized MgFe<sub>1.05</sub>O<sub>2.54</sub> core/(Mg,Al)-LDH shell particles [13]. Another method for the synthesis of Fe<sub>3</sub>O<sub>4</sub> core/(Mg<sup>2+</sup>, Al<sup>3+</sup>)-LDH shell NPs was by the precipitation of a 10 nm thick LDH shell onto 220 nm Fe<sub>3</sub>O<sub>4</sub> core, aggregated from primary particles of 10-15 nm [14]. In order to synthesize core/LDH shell nanoparticles with specific sizes, stability of the core NPs under LDH synthesis condition, minimization of homogeneous nucleation, uniformity of heterogeneous nucleation of LDH on the NP core, and control of LDH shell thickness are critical, and thus presents major challenges.

Herein, for the first time, the synthesis of spherical Ag (core)/LDH (shell) NPs using coprecipitation method without the need of any post-treatments, as well as the results of physico-chemical characterization are reported. The ultraviolet-visible (UV-vis) spectroscopy data indicate that for a given spherical Ag core diameter, a red-shift of the maximum wavelength ( $\lambda_{max}$ ) for transverse SPR absorption takes place with increasing LDH shell thickness up to 15 nm [15]. However, the shift is not extended into the desired NIR region. In contrast, since bare Ag nanorods show SPR

absorption in the NIR region, it will perhaps be a more appropriate core to synthesize Ag (nanorod core)/LDH (shell) NPs for nanomedicine.

## II. EXPERIMENTAL

All synthesis procedures and treatments were carried out at room temperature (25°C), unless specified otherwise. All chemicals were purchased from Sigma (St. Louis, MO, USA) and used as received unless otherwise indicated.

### A. Preparation of Silver Core Nanoparticles

A 10 ml solution of 0.25 mM AgNO<sub>3</sub> and 0.25 mM sodium citrate dihydrate was prepared. While vigorously stirring this solution, 600 µl of 0.01 M ice-cold NaBH<sub>4</sub> was added all at once. The color of the solution immediately changed to light yellow, indicating the formation of the seed solution; note, the seed solution was used within 12 hours since the Ag particles had a tendency to aggregate and to form a Ag thin film on the solution surface. This seed solution was used for the synthesis of Ag (core)/LDH (shell) NPs, as well Ag nanorods.

### B. Synthesis of Ag (core)/LDH (shell) Nanoparticles

For coating the Ag NPs with the LDH shell, a 50 ml solution containing 3.33 mM MgCl<sub>2</sub>·6H<sub>2</sub>O, and 1.67 mM AlCl<sub>3</sub>·9H<sub>2</sub>O, and 50 ml of 0.01 M NaOH base solution were simultaneously added to a 3-neck flask containing 50 ml of previously prepared Ag seed solution. Following the constant pH synthesis route, the pH was maintained at 10 while adding the salt and basic solutions. After aging for different durations (3, 6, 12 h), the solutions were centrifuged at 7000 rpm for 30 min. The supernatants were removed, and the Ag (core)/LDH (shell) NPs were re-dispersed in deionized water.

### C. Synthesis of Ag Nanorods

Five sets of 0.1 M cetyltrimethylammonium bromide (CTAB) solutions of 10 ml were prepared. These solutions were heated to 40°C to dissolve the CTAB and then cooled to room temperature. Next, 0.25 ml of 0.01 M AgNO<sub>3</sub> and 0.5 ml of 0.1 M ascorbic acid were added to each CTAB set. Then, various amounts of Ag seed solutions (i.e., 1.0, 0.5, 0.2, 0.1 and 0.05 ml) were added to the sets. Finally, 0.1 ml of 1 M NaOH solution was added to each set. Within 2 min of NaOH addition, the color changed from red to either brown or green depending on the concentration of Ag seed solution, and signaling a change in the aspect ratio. After aging for 1 hour, the solutions were centrifuged at 4000 rpm for 30 min. The supernatants (containing mostly small spheres and platelets) were removed, and Ag nanorods of various aspect ratios in different sets were re-dispersed in deionized water. The aspect ratio of the Ag nanorods increased with decreasing volume of Ag seed solution added.

### D. Characterization

The morphology and particle size of Ag (core)/LDH (shell) NPs are examined by the field emission scanning electron microscopy (FESEM; XL30 ESEM-FEG), which are further corroborated with transmission electron

microscopy (HRTEM; JEOL JEM-2010F TEM with an electron acceleration voltage of 200 KeV and analytical capability) bright field images. To prevent surface charging, the NPs were coated with 20 nm of gold by sputtering. The particle size and size distribution were also determined by dynamic light scattering (DLS; DynaPro MS/X, Protein Solutions Inc.). The crystallographic information of the Ag NPs and Ag (core)/LDH (shell) phases were collected using powder X-ray diffraction (XRD; Rigaku D/Max-IIB instrument with Cu-K<sub>α</sub> radiation, λ = 0.154059 nm) in 2θ range of 8°-90°. The Ag (core)/LDH (shell) nanostructures were confirmed by TEM in the bright field imaging mode. In addition, the elemental composition of the core/shell NPs was spatially mapped by energy dispersive X-ray spectroscopy (EDX) to confirm the formation of the LDH shell on the Ag core. Moreover, the morphology and composition of synthesized Ag nanorods were determined by TEM and EDX. Finally, the plasmon resonance frequencies of the Ag (core)/LDH (shell) NPs and Ag nanorods were determined by ultraviolet-visible spectroscopy (UV-Vis; Perkin Elmer Lambda 18) as a function of LDH shell thickness, and aspect ratio, respectively.

## III. RESULTS AND DISCUSSION

In order to synthesize Ag (core)/LDH (shell) NPs via heterogeneous coprecipitation<sup>[16]</sup>, aggregation of Ag NPs (<50 nm) and homogeneous nucleation must be averted. Note, prior to the heterogeneous nucleation of LDH, Ag NPs were electrostatically stabilized via the negative surface charge of the citrate layer. First, the aggregation of Ag NPs occurs below pH 4.6 (isoelectric point of citrate-stabilized NPs)<sup>[17]</sup>. Second, it was observed that Ag NPs transformed into aggregates when LDH salt solution was mixed with the Ag seed solutions because of an increase in the ionic strength. Due to electrostatic affinity, both Mg<sup>2+</sup> and Al<sup>3+</sup> cations stripped the charged citrate ligands away from the Ag NPs' surface, thereby rendering the unprotected Ag NPs towards aggregation. Third, it was found that high supersaturation condition favored homogeneous nucleation of LDH. Therefore, the optimized condition for the formation of the LDH shell on Ag NP core was the coprecipitation of a 50 ml solution containing 3.33 mM MgCl<sub>2</sub>·6H<sub>2</sub>O, and 1.67 mM AlCl<sub>3</sub>·9H<sub>2</sub>O in the presence of Ag NPs seeds following a constant pH (~10) route under low supersaturation condition (see the experimental section).

The morphology and particle size of heterogeneous LDH in the form of Ag (core)/LDH (shell) NPs were characterized by FESEM, as shown in Figure 1a. The particles exhibited a monodisperse size distribution with diameter ~50 nm. The size and size distribution of Ag (core)/LDH (shell) NPs, determined by DLS (data not shown), corroborated the FESEM and TEM data (given below). In contrast, the homogeneously precipitated discoidal LDH NPs (shown in Figure 1b) had a much larger diameter ~145 nm, despite the identical concentration and volume of LDH precursors used during their (i.e., Ag (core)/LDH (shell) NPs and LDH NPs) syntheses. The remarkable differences in shape and particle size emanate

from the differences in the nucleation and growth mechanism between seed-mediated coprecipitation of core/shell NPs and homogeneous coprecipitation of LDH NPs. In the former case, the total surface area and the large number of spherical Ag NPs offer plenty of heterogeneous nucleation sites. Since the activation energy barrier for heterogeneous nucleation is much lower than for homogeneous nucleation<sup>[16]</sup>, the LDH shells preferentially nucleate and grow on the spherical Ag NPs, resulting in a large number of narrowly-distributed, core/shell nanoparticles of much smaller size. Also, under the optimized reaction condition of low supersaturation, the homogeneous nucleation of LDH NPs is minimized in the presence of Ag nuclei.

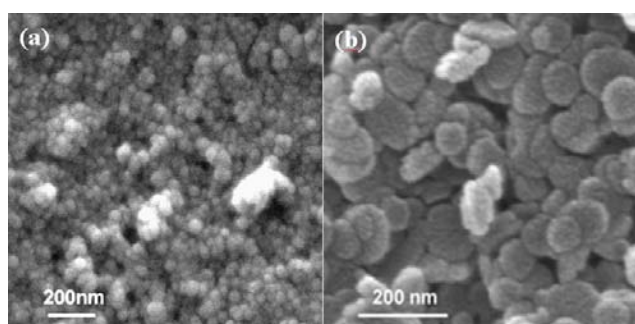


Figure 1 SEM images of (a) Ag (core)/LDH (shell) nanoparticles and (b) homogeneous LDH nanoparticles

The crystallinity of the Ag NPs (Figure 2a) and Ag (core)/LDH (shell) NPs (Figure 2b) were confirmed by XRD; the characteristic diffraction peaks of pure Ag and LDH were indexed and in agreement with past work on LDH<sup>[18]</sup>. With the experimental LDH  $d_{003}$  spacing of 0.793 nm ( $2\theta = 11.15^\circ$ ), and published data on the thickness of the Brucite layer of  $\sim 0.48$  nm<sup>[19]</sup>, the gallery height (or interlayer spacing) is found to be  $\sim 0.313$  nm. This implies that the intercalated species are a mixture of chloride (from precursor) and carbonate (from atmosphere) ions<sup>[4], [20]</sup>, and in agreement with the EDX data (shown later). Identification of the peaks between  $2\theta$  of  $37-40^\circ$  (Figure 2c), shows that the Ag (111) and LDH (012) peaks overlap. Based on these XRD patterns, although it can be inferred that Ag and LDH phases coexist, it does not provide conclusive evidence of core/shell structures.

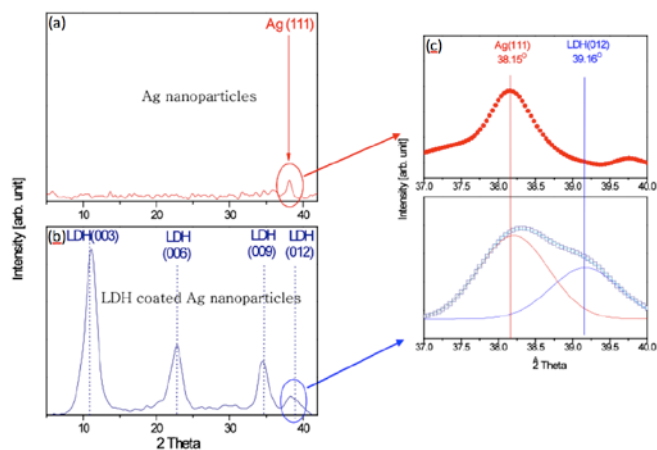


Figure 2 Powder XRD patterns of (a) pure Ag NPs, (b) Ag (core)/LDH (shell) NPs, and (c) magnified data in the  $2\theta = 37-40^\circ$  range

Figure 3 illustrates TEM images of Ag (core)/LDH (shell) NPs, and spatially dependent EDX data; the high magnification image shows a Ag core ( $\sim 45$  nm) coated with a thin LDH shell ( $\sim 10$  nm). Moreover, the EDX data are indicative of distinct compositional transitions as the probe is scanned outward from the center of the Ag NP core, i.e., the Ag signal peak diminishes while the LDH component-peaks (Mg, Al, C, Cl and O) are enhanced, clearly indicating that LDH shell surrounds the Ag core.

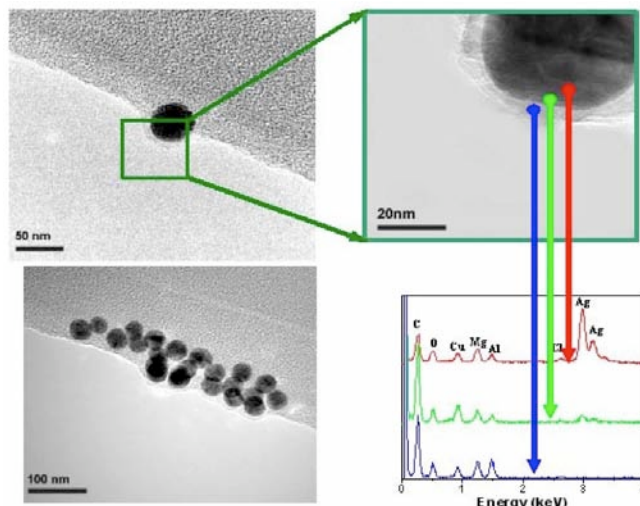


Figure 3 TEM images of spherical Ag (core)/LDH (shell) NPs with spatially-dependent EDX data

Both Ag NPs and various core/shell NPs have been intensively studied for their SPR properties<sup>[21], [22]</sup>. The SPR should arise when the incident photon frequency is resonant with the collective oscillations of the conduction electrons in the metal NP. From Mie theory, the magnitude of the extinction cross-section, comprising of the scattering and absorption components, as well as the wavelength ( $\lambda_{\text{max}}$ ) corresponding to its peak at SPR, should depend on the size (core and shell), shape, NP spacing, and dielectric properties of core and shell<sup>[23]-[25]</sup>. Interestingly, if thickness of LDH shell or the size and aspect ratio of Ag cores can be varied, the Ag-LDH may be readily tuned for maximum absorption (i.e., hyperthermic ablation) or for maximum scattering (i.e., NIR imaging by confocal reflectance microscopy or optical coherence tomography)<sup>[26], [27]</sup>. Since the eventual target for this study is hyperthermic ablation<sup>[28]-[30]</sup>, the focus here is on a size regime ( $<50$  nm) of the spherical Ag core, where dipole plasmon absorption is by far the dominant contributor to the extinction cross-section<sup>[31]</sup>.

Recent reports on the control of LDH shell thickness in core/shell inorganic structures include the tedious layer by layer adsorption LDH nanosheets onto large  $\text{Fe}_3\text{O}_4$  cores (500 nm)<sup>[12]</sup>, and post-synthetic ball milling in  $\text{MgFe}_{1.03}\text{O}_{2.54}$  (core)/(Mg<sup>2+</sup>, Al<sup>3+</sup>)-LDH (shell)<sup>[13]</sup>. In the current study, the shell thickness was found to be proportional to the (i) aging time (3, 6, 12 h), (ii) the quantity of 5 mM precursor salt solution, and (iii) inverse initial Ag NP density (either using 0 and 50 ml of Ag seed solution). Note, the latter methodology was the most reliable and controllable since the thickness of the LDH shell on the Ag core could be readily tuned within a few nanometers.

Figure 4 illustrates UV-vis spectroscopy data on the effects of the LDH shell thickness of spherical Ag (core)/LDH (shell) NPs; shell thicknesses (10, 12, and 15 nm) being controlled by various aging durations (3, 6 and 12 hr). For the Ag NP core,  $\lambda_{\max}$  for transverse SPR is at 395 nm, and with increasing thickness of the LDH shell,  $\lambda_{\max}$  red-shifts up to  $\sim 430$  nm for a shell thickness of 15 nm. However, these shifts are not sufficient and fall far below the targeted NIR range (800 nm).

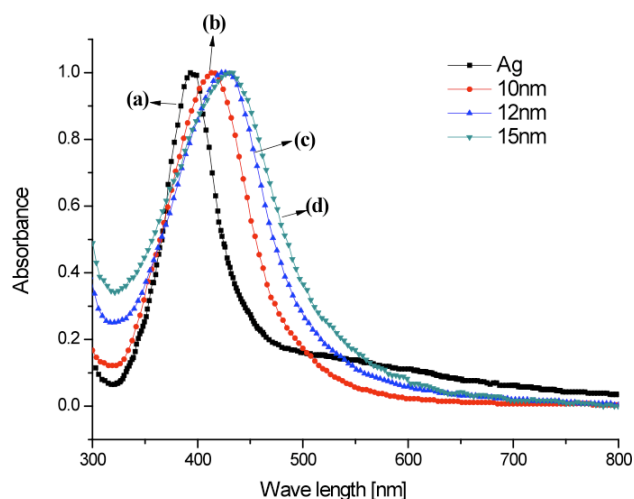


Figure 4 Absorption spectra by UV-Vis spectroscopy as a function of LDH shell thickness on Ag core.: (a) Ag NPs, (b) core/shell NPs with 10 nm shell thickness, (c) core/shell NPs with 12 nm shell thickness, and (d) core/shell NPs with 15 nm shell thickness

Silver nanorods with various aspect ratios were also synthesized (see the Experimental section). Just as gold (Au) nanorods<sup>[32]</sup>, bare Ag nanorods, with varying aspect ratio that increased with decreasing volume of seed solution, gave promising results. Figure 5 shows a bright-field TEM image and EDX data for specific Ag nanorods of 90-110 nm in length and 20-30 nm in diameter.

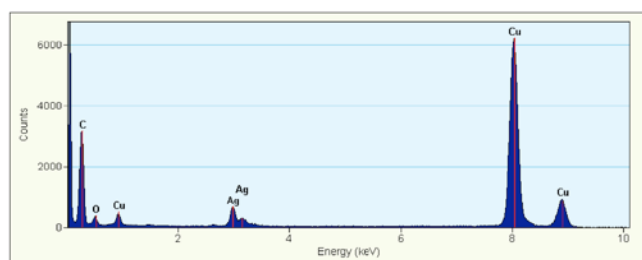
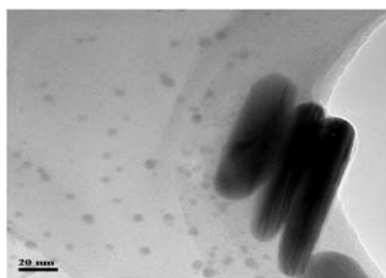


Figure 5 TEM bright-field image (top) of Ag nanorods and corresponding EDX data (bottom)

As depicted in Figure 6, the  $\lambda_{\max}$  for longitudinal SPR resonance of these nanorods gradually shifts towards longer

wavelengths with increasing aspect ratios; well into the NIR range. Also note that  $\lambda_{\max}$  for both transverse and longitudinal SPRs are observed in the Ag nanorods, with the dominance of longitudinal resonance with increasing aspect ratio. Additionally, since the relative contribution of scattering to the total cross section increases, the longitudinal plasmon resonance broadens<sup>[31]</sup>.

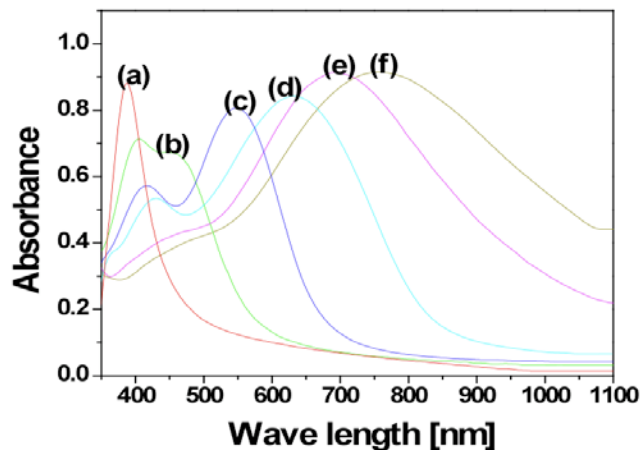


Figure 6 Absorption spectra by UV-Vis spectroscopy as a function of the aspect ratio of Ag nanorods synthesized with different amounts of seed solution. (a) Ag NP seeds, (b) 1000  $\mu$ l, (c) 500  $\mu$ l, (d) 200  $\mu$ l, (e) 100  $\mu$ l, and (f) 50  $\mu$ l

#### IV. CONCLUSION

The present work was a preliminary step towards the eventual goal of achieving simultaneous hyperthermia and chemotherapy, as well as molecular imaging of cancer cells using the nanostructured Ag-LDH platform. Here, a simple approach for synthesizing mono-dispersed spherical Ag (core)/LDH (shell) NPs without the need for any post-synthesis treatments has been presented. The core/shell NPs and Ag nanorods were characterized by FESEM, XRD, DLS, TEM, EDX, and UV-vis spectroscopy. In the spherical Ag (core)/LDH (shell) NPs, dramatic increases in the shell thickness will be required to bring the transverse  $\lambda_{\max}$  for SPR into the NIR region, but with the potential for NP aggregation. Alternatively, the lack of  $\lambda_{\max}$ -shift in spherical systems can be mitigated by the use of Ag nanorod cores of appropriate aspect ratio. The consequent cylindrical-shaped Ag nanorod (core)/LDH (shell) NPs, with varying LDH shell thickness and chemotherapeutic loading capacity, could potentially become a competitive and multimodal theranostic platform.

#### ACKNOWLEDGEMENTS

SKD acknowledges financial support from the National Cancer Institute, National Institutes of Health (1R21CA133618), National Science Foundation (CBET-0829128), and ASU Foundation's Women & Philanthropy (WZ91010). The authors acknowledge and deeply appreciate the useful discussions with Professor Kaushal Rege of Chemical Engineering and Dr. Vinay Nagaraj of the Biodesign Institute at Arizona State University (ASU), and are grateful to Dr. Thomas Groy, Dr. Paul Westerhoff, and Dr. Karl Weiss of ASU for assistance with XRD, DLS, and TEM, respectively.

## REFERENCES

- [1] O. C. Farokhzad, and R. Langer, "Nanomedicine: Developing smarter therapeutic and diagnostic modalities," *Adv. Drug Deliver. Rev.*, vol. 58, pp. 1456-1459, Dec. 2006.
- [2] H. C. Huang, S. Barua; G. Sharma, S. K. Dey, and K. Rege, "Inorganic nanoparticles for cancer imaging and therapy," *Journal of Controlled Release*, vol. 155, pp. 344-357, Nov. 2011.
- [3] R. F. Service, "Nanotechnology: Nanoparticle Trojan Horses Gallop from the lab into the clinic," *Science*, vol. 330, pp. 314-315, Oct. 2010.
- [4] S. K. Dey, and R. Sistiabudi, "Ceramic nanovector based on layered double hydroxide: attributes, physiologically relevant compositions and surface activation," *Mater. Res. Innov.*, vol. 11, pp. 108-117, Sep. 2007.
- [5] A. Flesken-Nikitin, I. Toshkov, J. Naskar, K. M. Tyner, R. M. Williams, W. R. Zipfel, E. P. Giannelis, and A. Y. Nikitin, "Toxicity and biomedical imaging of layered nanohybrids in the mouse," *Toxicol. Pathol.*, vol. 35, pp. 804-810, Oct. 2007.
- [6] S. J. Choi, J. M. Oh, and J. H. Choy, "Safety aspect of inorganic layered nanoparticles: Size-dependency in vitro and in vivo," *J. Nanosci. Nanotechnol.* vol. 8, pp. 5297-5301, Oct. 2008.
- [7] S. Y. Kwak, W. M. Kriven, M. A. Wallig, and J. H. Choy, "Inorganic delivery vector for intravenous injection," *Biomaterials*, vol. 25, pp. 5995-6001, Dec. 2004.
- [8] M. Del Arco, E. Cebadera, S. Gutierrez, C. Martin, M. J. Montero, V. Rives, J. Rocha, and M. A. Sevilla, "Mg, Al layered double hydroxides with intercalated indomethacin: Synthesis, characterization, and pharmacological study," *J. Pharm. Sci.*, vol. 93, pp. 1649-1658, Jun. 2004.
- [9] F. P. Bonina, M. L. Giannossi, L. Medici, C. Puglia, V. Summa, and F. Tateo, "Diclofenac-hydrotalcite: In vitro and in vivo release experiments," *Appl. Clay Sci.*, vol. 41, pp. 165-171, Oct. 2008.
- [10] M. Silion, M. I. Popa, G. Lisa, and D. Hritcu, "New hybrid compounds containing intercalated Ciprofloxacin into layered double hydroxides: Synthesis and characterization," *Rev. Roum. Chim.*, vol. 53, pp. 827, Sep. 2008.
- [11] P. Cherukuri, E. S. Glazer, and S. A. Curleya, "Targeted hyperthermia using metal nanoparticles," *Adv. Drug Deliver. Rev.*, vol. 62, pp. 339-345, Mar. 2010.
- [12] L. Li, Y. J. Feng, Y. S. Li, W. R. Zhao, and J. L. Shi, "Fe<sub>3</sub>O<sub>4</sub> Core/Layered Double Hydroxide Shell Nanocomposite: Versatile Magnetic Matrix for Anionic Functional Materials," *Ange. Chem. Int. Edit.*, vol. 48, pp. 5888-5892, Jul. 2009.
- [13] H. Zhang, D. K. Pan, K. Zou, J. He, and X. Duan, "A novel core-shell structured magnetic organic-inorganic nanohybrid involving drug-intercalated layered double hydroxides coated on a magnesium ferrite core for magnetically controlled drug release," *J. Mater. Chem.*, vol. 19, pp. 3069-3077, Mar. 2009.
- [14] D. K. Pan, H. Zhang, T. Fan, J. G. Chen, and X. Duan, "Nearly monodispersed core-shell structural Fe<sub>3</sub>O<sub>4</sub>@DFUR-LDH submicro particles for magnetically controlled drug delivery and release," *Chem. Commun.*, vol. 47, pp. 908-910, 2011.
- [15] A. Otto, "Excitation of nonradiative surface plasma waves in Silver by method of frustrated total reflection," *Z. Phys.*, vol. 216, pp. 398-410, 1968.
- [16] D. A. Porter, and K. E. Easterling, *Phase Transformation in Metals and Alloys*, 2nd ed., Ed. UK: Chapman & Hall, 1996, Chapter. 4.
- [17] S. H. Brewer, W. R. Glomm, M. C. Johnson, M. K. Knag, and S. Franzen, "Probing BSA binding to citrate-coated gold nanoparticles and surfaces," *Langmuir*, vol. 21, pp. 9303-9307, Sep. 2005.
- [18] R. Chitrakar, Y. Makita, A. Sonoda, and T. Hirotsu, "Synthesis of a novel layered double hydroxides [MgAl<sub>4</sub>(OH)<sub>12</sub>](Cl)<sub>2</sub>·2.4H<sub>2</sub>O and its anion-exchange properties," *J. Hazard. Mater.*, vol. 185, pp. 1435-1439, Jan. 2011.
- [19] R. Allmann, "Crystal structure of Pyroaurite," *Acta Crystall. B-Struc.*, vol. B 24, pp. 972-977, 1968.
- [20] S. Tezuka, R. Chitrakar, A. Sonoda, K. Ooi, and T. Tomida, "Studies on selective adsorbents for oxo-anions. Nitrate ion-exchange properties of layered double hydroxides with different metal atoms," *Green Chem.*, vol. 6, pp. 104-109, Feb. 2004.
- [21] T. R. Jensen, M. D. Malinsky, C. L. Haynes, and R. P. Van Duyne, "Nanosphere lithography: Tunable localized surface plasmon resonance spectra of silver nanoparticles," *Journal of Physical Chemistry B*, vol. 104, pp. 10549-10556, Nov. 2000.
- [22] J. L. Lyon, D. A. Fleming, M.B. Stone, P. Schiffer, and M. E. Williams, "Synthesis of Fe oxide core/Au shell nanoparticles by iterative hydroxylamine seeding," *Nano Letters*, vol. 4, pp. 719-723, Apr. 2004.
- [23] R. W. Wood, "On a remarkable case of uneven distribution of light in a diffraction grating spectrum," *Philos. Mag.*, vol. 4, pp. 396-402, Jul. 1902.
- [24] C. F. Bohren, and D. R. Huffman, *Absorption and Scattering of Light by Small Particles*, Ed. Germany: John Wiley & Sons, 1983.
- [25] P. K. Jain, K. S. Lee, I. H. El-Sayed, and M. A. El-Sayed, "Calculated absorption and scattering properties of gold nanoparticles of different size, shape, and composition: Applications in biological imaging and biomedicine," *J. Phys. Chem. B*, vol. 110, pp. 7238-7248, Apr. 2006.
- [26] L. R. Hirsch, R. J. Stafford, J. A. Bankson, S. R. Sershen, B. Rivera, R. E. Price, J. D. Hazle, N. J. Halas, and J. L. West, "Nanoshell-mediated near-infrared thermal therapy of tumors under magnetic resonance guidance," *Proc. Natl. Acad. Sci. USA*, vol. 100, pp. 13549-13554, Nov. 2003.
- [27] C. Loo, A. Lin, L. Hirsch, M. H. Lee, J. Barton, N. J. Halas, J. West, and R. Drezek, "Nanoshell-enabled photonics-based imaging and therapy of cancer," *Technol. Cancer Res. T.*, vol. 3, pp. 33-40, Feb. 2004.
- [28] S. J. Oldenburg, J. B. Jackson, S. L. Westcott, and N. J. Halas, "Infrared extinction properties of gold nanoshells," *Appl. Phys. Lett.*, vol. 75, pp. 2897-2899, Nov. 1999.
- [29] R. Weissleder, "A clearer vision for in vivo imaging," *Nat. Biotechnol.*, vol. 19, pp. 316-317, Apr. 2001.
- [30] M. L. J. Landsman, G. Kwant, G. A. Mook, and W. G. Zijlstra, "Light-absorbing properties, stability, and spectral stabilization of Indocyanine Green," *J. Appl. Physiol.*, vol. 40, pp. 575-583, 1976.
- [31] R. D. Averitt, S. L. Westcott, and N. J. Halas, "Linear optical properties of gold nanoshells," *J. Opt. Soc. Am. B*, vol. 16, pp. 1824-1832, Oct. 1999.
- [32] S. Link, M. B. Mohamed, and M. A. El-Sayed, "Simulation of the optical absorption spectra of gold nanorods as a function of their aspect ratio and the effect of the medium dielectric constant," *J. Phys. Chem. B*, vol. 103, pp. 3073-3077, Apr. 1999.

# Mechanical Characterization and Improvement of Weaveability for Glass/Polypropylene Commingled Hybrid Yarns

A.R.Torun\*, E. Staiger, G.Hoffmann, Ch. Cherif

Institute of Textile Machinery and High Performance Material Technology, Technische Universitaet Dresden,  
01062 Dresden, Germany  
refahtorun@gmail.com

**Abstract-**This study was conducted due to the necessity for improving the processability of commingled yarns during textile processing, in particular dense 3D preform weaving. Open structure of the commingled yarns caused higher production stops. As a possible solution, Glass/Polypropylene (GF/PP) commingled yarns with different twisting levels were produced. Effect of twisting on the mechanical properties of commingled yarns and on their compression molded UD composites are determined. As a result, twisting did not significantly affect the modulus of elasticity of UD-composites. However, the tensile strength of UD-composites was reduced by further processing even without twisting. Therefore small twisting levels can be applied on commingled yarns to improve processability of dense preforms without significantly affecting the mechanical performance. Furthermore, the damage on the yarns, preforms and composites is determined for various weft densities which indicate differing crimp ratios. Higher crimp ratios both increase the damage on reinforcement yarns and significantly decrease the mechanical properties.

**Keywords-** Hybrid Yarn; Thermoplastic Composite; Woven Preform

## I. INTRODUCTION

Thermoset polymers have been dominating the market as the matrix of choice for composites. Thermosets have lower viscosity in comparison with thermoplastics, which can be seen as the main advantage for the sake of processability. They also do not necessarily need pressure or heat during processing. Thermoset resins are generally inexpensive and stronger than thermoplastics with a higher serving temperature. Short workable pot life, the difficulties concerning the recycling issues and emission of volatile organic compounds are the main disadvantages. Thermoplastics offer higher impact strength and a good surface finish. They can be processed without emission of hazardous gases and recycled much easier<sup>[1], [2]</sup>. Recycling is becoming more and more important due to the strict regulations of mass production industries such as automobile industry.

The viscosities of fully polymerized thermoplastics are around two to three orders of magnitude higher than their thermoset counterparts<sup>[3]</sup>. In order to overcome the difficulties of impregnation caused by high viscosity of thermoplastics, reinforcement materials (e.g. carbon, glass) and thermoplastic polymer (e.g. PP, PEEK) are already mixed in solid state. The aim of solid state mixing is to

reduce the flow path of polymers during impregnation. This mixture is processed into preforms mostly with textile machinery. Thermoplastic polymers in the preform are melted under the application of pressure and temperature (e.g. pultrusion, compression molding), and consolidated<sup>[4]-[6]</sup>.

Commingled yarns can be produced with a modified air-jet texturizing machine (Fig. 1). The most important modification is the type of air nozzle used. Commercial air nozzles are available, which claim to reduce the damage on the reinforcement yarns during processing and offer a better mixture in the crosssection. Especially for commingled yarns, a good mixture in the crosssection is crucial, because the main idea of commingling process is to reduce the flow paths of the viscous thermoplastic resin. Another important modification for commingling process is the bobbin winding device. Commingled yarns should be wound up with a constant yarn tension with higher bending radii of machine elements to minimize the damage on the yarn. Besides material mixing and high production rates, commingled yarns embody structural elongation which enables a smoother processing with textile machinery. During commingling process, reinforcement yarns are damaged by the applied air pressure in the nozzle, which can be seen as a drawback. Another disadvantage of commingled yarns was identified from processing point of view while executing trials on high packing densities of 3D near-net shape woven preforms<sup>[7]-[9]</sup>. Harnesses apply forces on the warp yarns in both normal and longitudinal direction during weaving. These forces should be minimized by reducing the warp yarn tension especially for the brittle reinforcement yarns. However, reduced warp yarn tension with high packing density increases the probability of stuck yarns in the shed and causes unclear shed opening. After commingling, yarns become more voluminous and open. Depending on the structure, high packing density commingled yarns showed higher production stops than conventional materials, which necessitates improvement for the industrial production. According to Lee et al.<sup>[10]</sup> and Rudov-Clark et al.<sup>[11]</sup>, the fibre damage in the weaving process, due to elongation and yarn friction, has only a low impact on the properties of stiffness and strength in the composite. However, the unclear shed opening and resulting machine stops were not discussed.

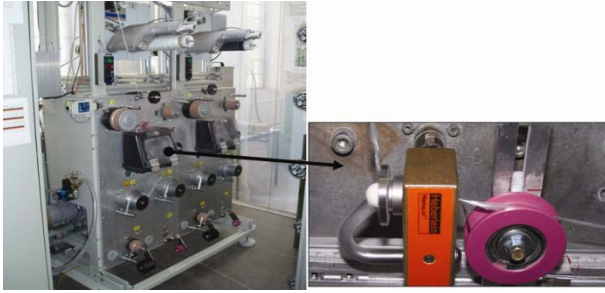


Fig. 1 Air-jet texturizing machine utilized for commingled yarn production (left) and detail view of the air nozzle (right)

Over-delivery of input yarns is necessary for the formation of the commingled structure [12]. This indicates the possibility of slightly twisting the commingled yarn to create a more compact yarn structure without causing significant effect on the composite properties. In the literature, contributions about the effects of twisting on high performance yarns were reported. However, no study is available about the effect of twisting on the commingled yarns and their composites. Within the scope of this study, main aim is to determine whether twisting can be applied to commingled yarns in order to improve the processing behavior on textile machinery. The effect of twisting level both on the yarn and composite properties were analyzed to see how the physical and mechanical properties were changed.

## II. EXPERIMENTAL

### A. Materials

The GF/PP commingled yarns were produced with the commercial input materials of 300 tex glass (E 35, P-D Glasseiden GmbH, Germany) and 3 x 32 tex polypropylene (Prolen H, CHEMOSVIT FIBROCHEM a.s., Slovakia) which resulted in a fiber volume fraction of 52% in UD composites. Commingled yarns were produced with 4 bar air pressure in the nozzle and a winding speed of 100 m/min. In order to generate the commingled structure, input cylinders deliver the glass and polypropylene yarns with a higher speed than the output cylinder which is removing the final commingled yarn out of the air-nozzle. This setting is called over-delivery and defined as the percentage ratio of the speed difference to the output cylinder speed. Equation 1 shows the calculation of over-delivery OD, where  $S_i$  is the input speed of feeding cylinders and  $S_o$  is the output speed of take-up cylinders.

$$OD = \frac{S_i - S_o}{S_o} * 100 \quad (1)$$

Over-delivery of glass yarns was kept at a value of 2% to avoid damage and extensive loss of orientation. Over-delivery of polypropylene yarns was 8%, therefore polypropylene filaments had higher entanglement than glass filaments and were tending to be at the outer part in the cross-section.

Produced commingled yarns were twisted (DirecTwist, Agteks) with 0, 5, 10, 15, 20, 40 and 60 tpm (twist per meter)

and compared with the reference yarn which was commingled without any further process. 0 twist per meter in the trials actually means winding to another bobbin by using the same twisting machine. Winding without twist was done to isolate the effect of extra processing on the yarn properties. 5 to 20 tpm were the main experiments of concern whereas 40 and 60 tpm experiments demonstrated extreme values. Uni-directional (UD) composites were produced with compression molding. Processing conditions for compression molding is shown in Figure 2.

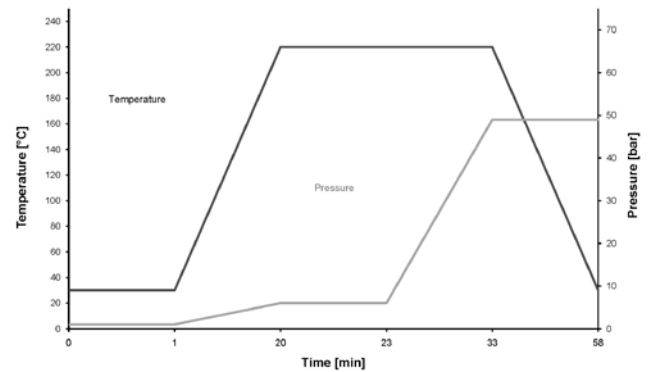


Fig. 2 Processing parameters for compression molding of UD-composite plates

Woven fabrics with the below defined weave were produced with weft densities of 7, 8, 9 and 10 yarn/cm. Warp density was 20 yarn/cm for every sample. Commingled hybrid yarns, which were defined in Section 4, were used both as warp and weft yarns. Compression molding technique was used with the same settings of Section 4. In order to increase the wall thickness of spacer fabrics, it is possible to lay flat woven fabrics above and under the spacer fabrics, and they can be pressed together. Therefore, within the design of experiments, 1, 2 and 3 layers of flat woven fabrics were consolidated and tested.

### B. Testing Procedure

Yarn profiles as well as yarn-yarn and yarn-metal friction coefficients were determined by using dynamic tensile tester (LH-402 CTT-DTT Attachment, Lawson Hemphill Inc. USA). A CCD camera was used to measure the yarn diameter values with 3.25 micron precision when the yarn was moving at a speed of 100 m/min. Yarn-metal and yarn-yarn friction coefficients were determined dynamically according to ASTM D-3108, and ASTM D-3412. Tensile tests for yarns were executed with 20 specimens according to the norm DIN EN ISO 2062, with a clamping length of 500 mm and testing speed of 25 mm/min (Z100, Zwick GmbH & Co. KG). Tensile tests of UD-composites were executed according to DIN EN ISO 527-4. Upper and lower clamping areas were 50 mm each, and the testing lengths of the specimens were 150 mm. 0° specimens had a width of 15 mm and 90° specimens had a width of 25 mm. 12 specimens for 0° and 8 specimens for 90° were tested for each twisting level and the reference. Testing speeds for both 0° and 90° were 2 mm/min. Confidence intervals with 95% were determined according to Student's t-distribution.

Woven fabrics were tested according to DIN EN ISO 13934-1, with a width of 50 mm and gauge lengths of 200 mm. 5 samples were tested for each trial. For the woven composites, tensile tests were executed according to DIN EN ISO 527-4. Upper and lower clamping areas were 50 mm each, and the testing lengths of the specimens were 150 mm. Both weft and warp direction samples had the width of 25 mm. Testing speed were 2 mm/min. 4 point bending tests were executed according to DIN EN ISO 14125. Sample length was 60 mm and sample width was 15 mm. Testing speed of bending was 2 mm/min. Charpy impact test was executed according to ISO 179-2. Confidence intervals with 95% were determined according to Student's t-distribution.

### III. RESULTS AND DISCUSSION

#### A. Commingled Yarn Structure

Commingling process is based on the mixing of materials through an air nozzle. As in the air jet texturizing process, commingling process creates a special yarn structure with two different areas which are called as bulky and knot areas (Fig. 3). Continuous air pressure through the nozzle creates distinctive areas; in bulky region the materials are voluminous and open whereas in knot areas they are intermingled together. Various process parameters such as nozzle type, air pressure, take-up speed etc. affect the frequency and intermingling intensity of knot areas. However, a full control on this phenomenon is not possible. In the case of commingled yarns, a better mixture of reinforcement and matrix materials occurred in the knot area. Figure 3 demonstrates the cross-sectional observations from bulky and knot areas, dark points are polypropylene and the light colored points are glass filaments.

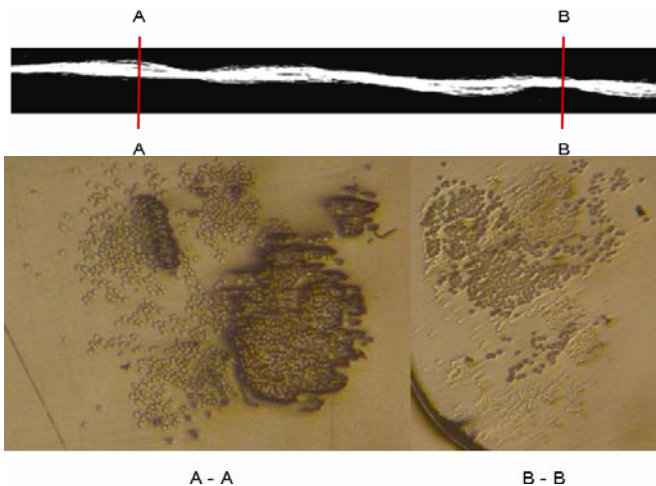


Fig. 3 Cross-sectional observations of bulky (A-A) and knot (B-B) areas of GF/PP commingled yarns X-twill weave (left) L: lower weft yarn, U: upper weft yarn, and woven fabric (right)

Profile scanning results demonstrated a progressive improvement of commingled yarn evenness with increasing twist (Fig. 4). Bulky and sticky regions on commingled yarns were the main cause of production stops during weaving. The number of events, which is defined as  $\pm 50\%$  variations in yarn diameter, was decreased from 42 events/m to the interval of 30-35 events/m for all twisting ratios.

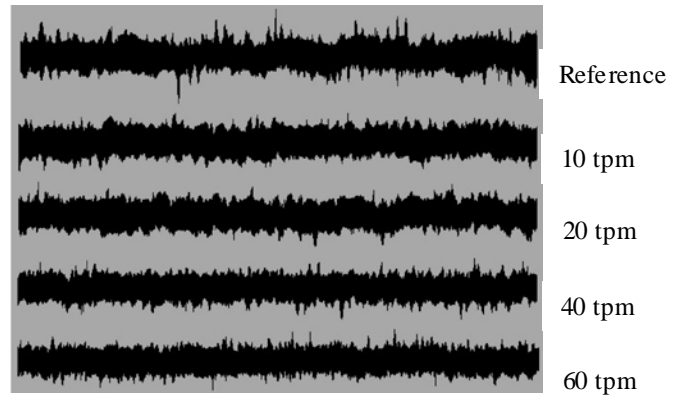


Fig. 4 Comparison of GF/PP commingled yarn profile, from top to bottom; reference commingled yarn, 10tpm, 20tpm, 40tpm, 60tpm

Mean values of yarn diameter (Fig. 5) were increased for 0 tpm and 5 tpm samples, which was caused by the effect of the additional process step. After 10 tpm, yarn diameter decreased gradually.

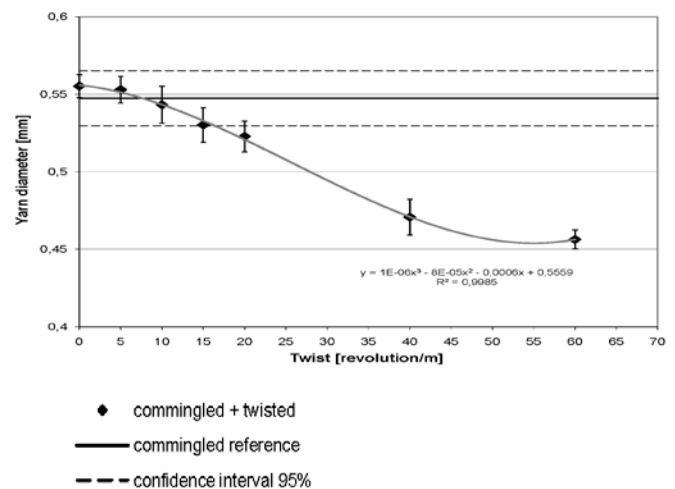


Fig. 5 Comparison of GF/PP commingled yarn profile, from top to bottom; reference commingled yarn, 10 tpm, 20 tpm, 40 tpm, 60 tpm

The standard deviation of every sample was less than the reference commingled yarn, thus more regular yarn structure was generated.

Small yarn diameters enable denser packing of material during weaving. 3rd degree regression polynomial in Figure 3 has a local minimum around 55 tpm. After 60 tpm the diameter would not change significantly. However, the regression polynomial increases. Therefore the regression polynomial can be used for interpolation between the twisting values of 0 tpm and 60 tpm, but twisting values more than 60 tpm cannot be estimated with extrapolation.

#### B. Yarn Mechanical Properties

Over-delivery of input materials in commingling process is necessary in order to create the knot areas, and most of the additional material length is integrated in these areas because the bulky region can easily be stretched during further processing. The twist angle equivalent of over-delivery ratio was calculated according to Equation 2, where  $\alpha_{od}$  is twist angle equivalent caused by over-delivery and OD (%) is the over-delivery of input material.

Over-delivery of the reinforcement material within commingled hybrid yarn can be approximated as an angle distortion of a lamina. The input length of the reinforcement material is the hypotenuse of a right triangle and the output length is the adjacent side. Figure 6 demonstrates this approximation where OD is the over-delivery as percentage and  $\theta$  is the angle of distortion.

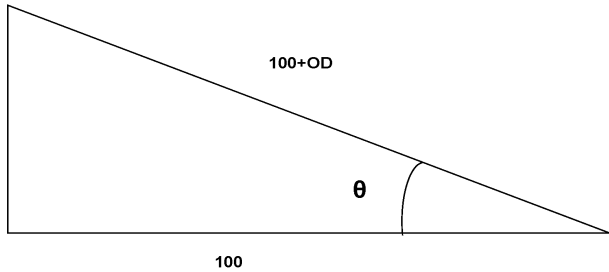


Fig. 6 Comparison of GF/PP commingled yarn profile, from top to bottom; reference commingled yarn, 10tpm, 20tpm, 40tpm, 60tpm

The inverse trigonometric function of cosine gives the equivalent of the distortion angle as shown in the Equation 2.

$$\alpha_{od} = \cos^{-1}\left(\frac{100}{100 + OD}\right) \quad (2)$$

An interesting phenomenon was the increase of both breaking force and E-modulus of commingled yarns after further processing. After twisting with 0° (only winding), yarn samples had higher E-modulus and breaking force than the reference yarn (Fig. 7). This is caused by the restructuring of the knot areas under tension, the yarn was stretched and the orientation of the reinforcement material in knot areas was increased. Figure 7 demonstrates the E-modulus and breaking force comparison of twisted and reference GF/PP commingled yarns. 40 tpm sample had almost the same E-modulus and breaking force values as the reference sample. Reduction of E-modulus started with 60 tpm sample, however the breaking force was still the same as the reference yarn. These results indicate that the higher intermingling of filaments through twisting increases the mechanical properties of commingled yarns. Damage on glass fibers cannot be easily detected with yarn testing.

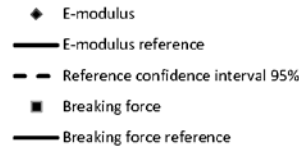
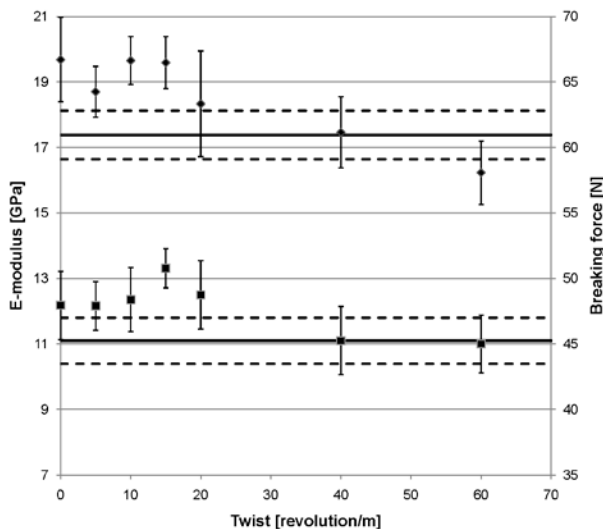


Fig. 7 Effect of twisting on the E-modulus and breaking force of GF/PP commingled yarns

### C. UD Composite Properties

The 0° and 90° E-modulus calculations were executed according to laminate theory. UD-composite calculations were based on the homogeneous distribution of the glass filament in the PP matrix. Off-axis angle equivalent of over-delivery value for glass yarn was integrated to the equation, thus the UD composites structures were assumed to have a slight angle distortion.

Slab models deliver sufficient approximation to the elastic constants of a lamina. Within this model, aligned long fiber composites were treated as if the two constituents of matrix and reinforcement are bonded together. Relative thicknesses of slabs were determined according to the volume fractions of fiber and matrix. Interface regions as well as local stress concentrations were ignored. E1 (E-modulus fiber direction) is calculated according to equal strain assumption for both matrix and fiber in longitudinal direction. The Equation 3 is also called as “the rule of mixtures” and delivers a very good approximation. Discrepancies may result from the different poisson’s ratios of matrix and reinforcement. However, it can be theoretically proved by the Eshelby model that the deviation is small under all conditions [13], [14].

$$E_1 = E_{1f} * Vf + E_m * (1 - Vf) \quad (3)$$

Transverse modulus of a composite with unidirectional fibers can also be approximated by a slab model which assumes an equal stress condition for matrix and fibers. The stress field is complex under transverse loading and in the literature, especially for thermoplastic matrices, underestimation of transverse modulus was reported. The modified equation for the transverse modulus contains a correction factor  $\eta$  [15]-[17]. If  $\eta$  is taken as 1, the equation becomes the usual expression derived from an equal stress assumption for matrix and reinforcement. In order to fit the experimental data,  $\eta$  was taken as 0.6 which compensates the above mentioned underestimation of transverse modulus.

$$E_2 = \frac{Vf + \eta * (1 - Vf)}{\frac{Vf}{E_{2f}} + \frac{\eta * (1 - Vf)}{E_m}} \quad (4)$$

The expression for the in-plane shear modulus is analogous to the expression of transverse modulus because it assumes equal shear stress on the matrix and fibers. In order to avoid the underestimation,  $\eta$ ’s parameter with 0.6 is applied in the calculations.

$$G_{12} = \frac{Vf + \eta' * (1 - Vf)}{\frac{Vf}{G_{12f}} + \frac{\eta' * (1 - Vf)}{G_m}} \quad (5)$$

Since the equal strain assumption is applicable to a UD lamina, the poisson's ratio can be determined by "the rule of mixtures".

$$v_{12} = v_{12f} * Vf + v_m * (1 - Vf) \tag{6}$$

According to the above expression, 2% over-delivery of glass filaments was equivalent to 11.36° off-axis angle distortion. The off-axis longitudinal and transverse stiffness were calculated according to laminate theory.

Stiffness value in longitudinal direction is found as 34.13 GPa which is underestimating the experimental results. Experimental results of longitudinal E-modulus in Figure 8 show agreement with the nominal values stiffness values according to the rule of mixtures. This indicates that the angle distortion caused by the over-delivery disappears during compression molding under tension. Modulus of elasticity in 0° direction is not much affected from twisting. Statistically, only the modulus of elasticity of the 60 tpm sample can be regarded as a reduction. On the other hand, the effect of further processing can be easily seen from the tensile strength reduction starting immediately with 0 tpm sample. All the samples had an overall tendency of strength reduction. However, between 0 tpm and 60 tpm samples, it cannot be concluded that higher twist reduces the strength more than lower twist.

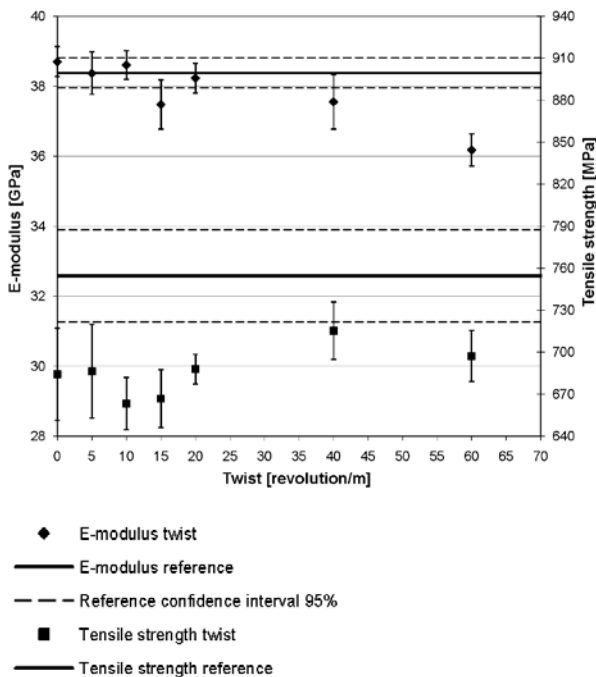


Fig. 8 Modulus of elasticity and tensile strength of UD composites from GF/PP commingled yarns in 0°

Lamina stiffness calculation in transverse direction, 3.98 GPa, is in good agreement with overall experimental results (Fig. 9). It can be seen in Figure 5 that the yarn diameter is decreasing after 10 tpm. As the UD performs were prepared with the same amount of material, increasing compactness of the reinforcement material leads to greater resin rich areas. This reduces the E-modulus in transverse direction. Transverse tensile strength shows a slight reduction tendency with increasing twist level.

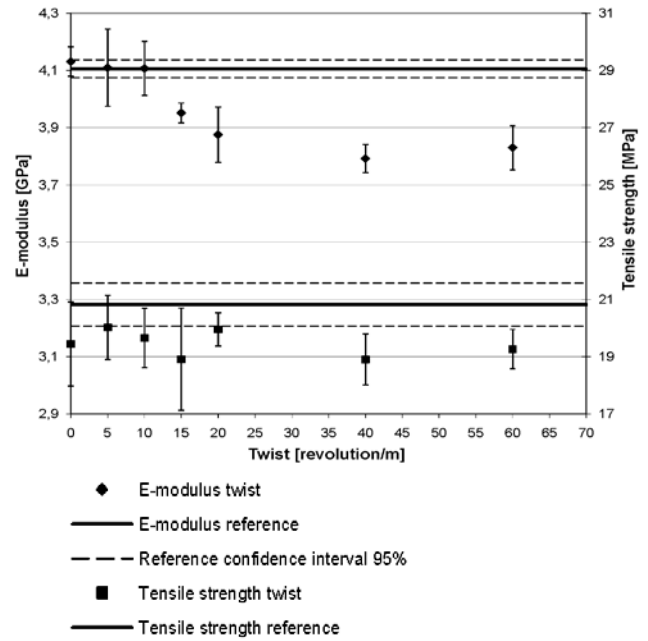


Fig. 9 Modulus of elasticity and tensile strength of UD composites from GF/PP commingled yarns in 90°

D. Woven Fabric Properties

It is important to execute experiments concerning the mechanical characteristics of 2D woven fabrics and their composites in order to gain insight about the potential performance of composites from 3D woven fabrics. The aim of this section is to determine the process damage on the reinforcement material as well as the effect of structural parameter in particular weft density and number of plies.

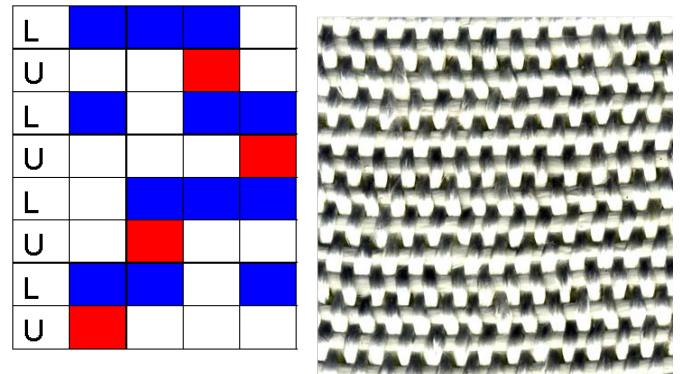


Fig. 10 X-twill weave (left) L: lower weft yarn, U: upper weft yarn, and woven fabric (right)

Compression molding causes significant change of thickness during consolidation of thermoplastic matrix preforms. If a constant weave is selected, increasing the weft density results in higher weight per unit area as well as a higher thickness of the final composite. On the other hand, higher weft density changes the inner structure of the woven fabric and processing conditions. A weaving machine with a dobby shed opening mechanism has a limited number of heddle frames (mostly up to 24). The weaving machine, which was used for the development of spacer fabrics, had 16 heddle frames. Spacer fabrics with woven cross-links have four different areas, two for upper and lower layers and two for the cross-links<sup>[18]</sup>. These four areas have four heddle

frames each for the construction of weave. Figure 10 demonstrates the selected double layer X-twill weave for the woven areas of spacer fabrics. Double layer woven fabric provides sufficient thickness after compression molding, and the X-twill weave is homogenous due to its both diagonal directions. Usual twill weaves have only one diagonal direction which results in anisotropic in-plane mechanical properties.

Fabric mass per unit area increases with the increase of weft density. Table 1 demonstrates the variation of mass per unit area for the woven fabric samples with 7-10 yarn/cm. This increase directly affects the final composite thickness which is shown in Table 2.

TABLE I RELATION BETWEEN WEFT DENSITY AND MASS PER UNIT AREA

Weft Density [Yarn/Cm]	7	8	9	10
Mass per unit area [g/dm <sup>2</sup> ]	11,307	11,960	12,389	13,065

TABLE II THICKNESSES OF CONSOLIDATED WOVEN FABRICS

		Weft Density [number of yarns/cm]			
		7	8	9	10
Number of Layers	1	0,68 mm	0,71 mm	0,73 mm	0,77 mm
	2	1,36 mm	1,4 mm	1,46 mm	1,53 mm
	3	2,03 mm	2,1 mm	2,19 mm	2,28 mm

Changing of process parameters on the weaving machine also changes the amount of damage on the materials. Process damage on the materials during weaving is mainly caused by friction through feeding, shear and bending caused by the heddle frames, shear stresses caused by beat-up and the friction and buckling caused by the take-up motion. Conventional materials such as cotton compensate these stresses with their internal elongation. Reinforcement materials such as glass fibers are mostly brittle and they are prone to damage particularly under bending along a small radius. In this sense, heddle frames are the most critical machine elements where process damage occurs. Changing of weft density also changes the flow rate of material, thus higher weft density results in higher number of cycles of warp yarns through the heddle frames. Figure 11 depicts the schematic of shed opening.

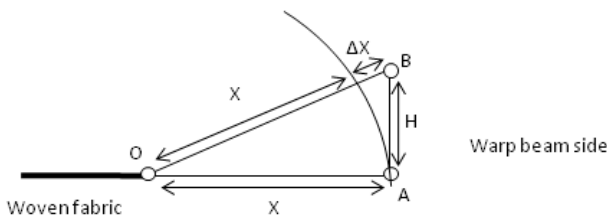


Fig. 11 Schematic of shed opening

The elongation of technical yarns is negligible, so the position change of eyelet from Point A to Point B is compensated from the warp beam side. Any point on the warp yarn must travel the distance ΔX through the eyelet of heddle frame. Weft density determines the number of cycles, in which the warp yarn can pass through this distance under buckling and shear stresses. ΔX can be calculated according

to the Equation 7 where X is the distance between the woven fabric line and the horizontal position of eyelet, and H is the distance between the horizontal position and the maximum height of eyelet.

$$\Delta X = \sqrt{X^2 + H^2} - X \tag{7}$$

In every cycle of the weaving machine, warp yarns travel the distance TD which is the inverse of weft density WD (Equation 8).

$$TD = WD^{-1} \tag{8}$$

In order to find the number of cycles NC for warp yarns to pass through the heddle frame, the expression of ΔX is divided by the travel distance in one cycle TD which gives:

$$NC = \left[ \sqrt{X^2 + H^2} - X \right] * WD \tag{9}$$

From Equation 9, it can be seen that the number of cycles to pass through the heddle frame is directly proportional to the weft density. Therefore it is expected to have higher damage to the warp yarns processed with higher weft densities.

Figure 12 compares the breaking force of unprocessed reference GF/PP commingled yarns and the processes steps after warp beam preparation and the woven fabric manufacturing with different weft densities. As expected, the tendency of reduction in breaking force can clearly be seen both on the weft and the warp yarns.

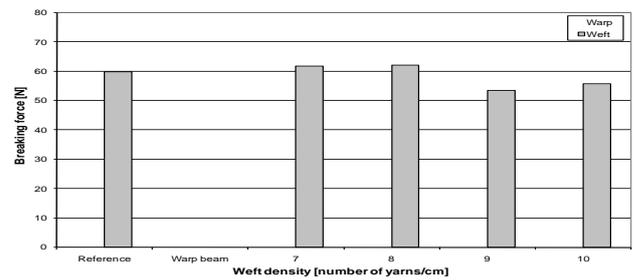


Fig. 12 Change of yarn tensile strength after beaming and weaving

Woven fabric tensile test results are depicted in Figure 13. The tendency of breaking force reduction of fabrics in warp direction with increasing weft density is higher in comparison with the tendency of individual yarns. The reason for this phenomenon is that both warp yarn crimp and damage to the yarn increases with higher weft density. In weft direction, breaking force increases with higher weft density simply due to the increased number of yarns. Therefore the process damage cannot be seen directly from the breaking force of the fabric.

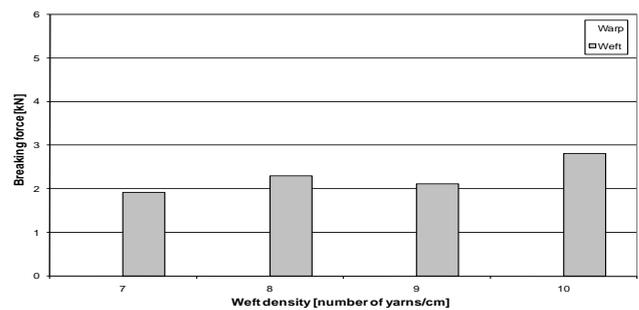


Fig. 13 Tensile strength of woven fabrics with different weft densities

Compression molding causes extensive deformation of woven fabrics in the normal direction. Depending on the process conditions and the fabric structure, the thickness of the final composite is around 20% of the thickness of woven fabric. This deformation in the normal direction results in the sinus form of warp yarns, which can be seen in Figure 14 for different weft densities. It can be clearly seen from the figure that the increasing weft density also increases the lateral deformation. Thus the period of sinus form in the sample with the weft density of 10 yarn/cm is shorter than that of the sample with the weft density of 7 yarn/cm.



Fig. 14 Composite surfaces with weft densities of 7 to 10 from left to right

Figures 15–20 demonstrate the results of tensile tests in warp and weft directions with weft densities 7-10 and 1-3 plies. Increasing weft density slightly increases both modulus of elasticity and tensile strength in weft direction. Higher weft density changes the structure of the reinforcement, particularly the curvature of warp yarns along the weft yarns increases. Higher curvature of warp yarns results in smaller resin rich areas which have a positive effect on tensile behavior. On the other hand, higher weft density reduces the modulus of elasticity and tensile strength drastically. Process damage on the warp yarns is higher with higher weft density (Figures 12), but the reduction of properties is mainly caused by the distortion of the reinforcement material.

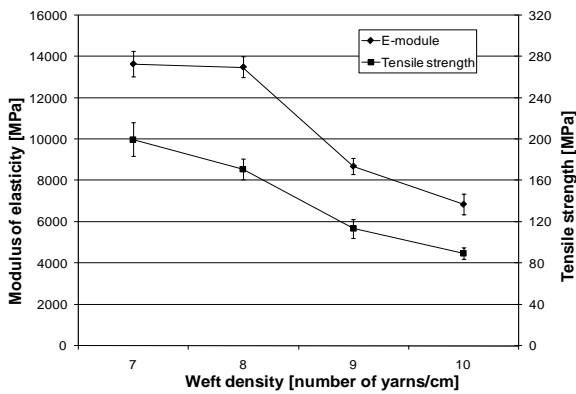


Fig. 15 Modulus and tensile strength of 1 layer consolidated fabrics in warp direction

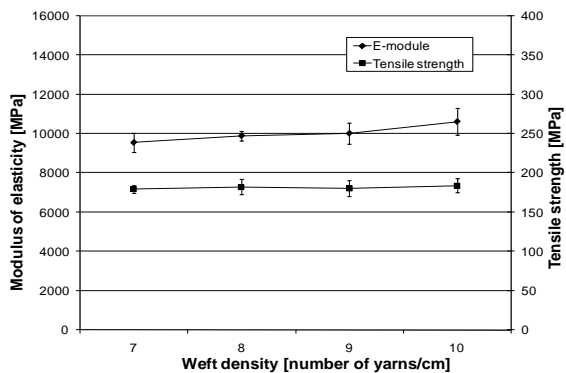


Fig. 16 Modulus and tensile strength of 1 layer consolidated fabrics in weft direction

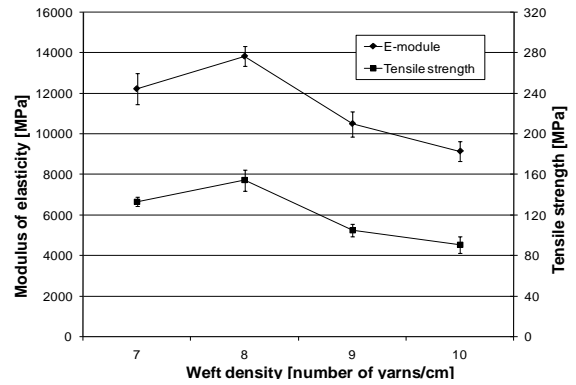


Fig. 17 Modulus and tensile strength of 2 layer consolidated fabrics in warp direction

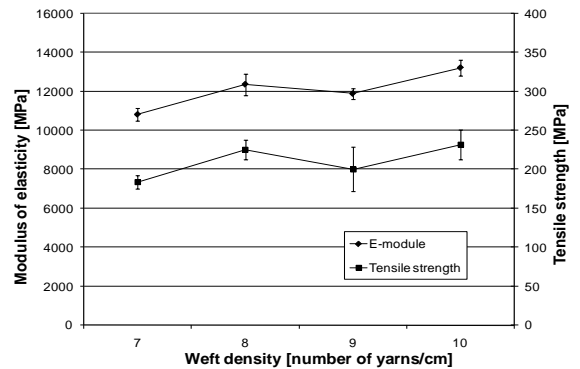


Fig. 18 Modulus and tensile strength of 2 layer consolidated fabrics in weft direction

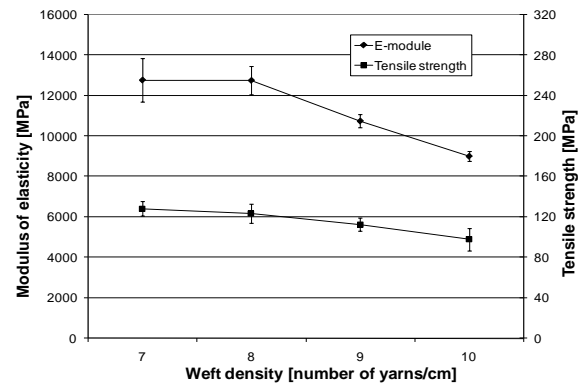


Fig. 19 Modulus and tensile strength of 3 layer consolidated fabrics in warp direction

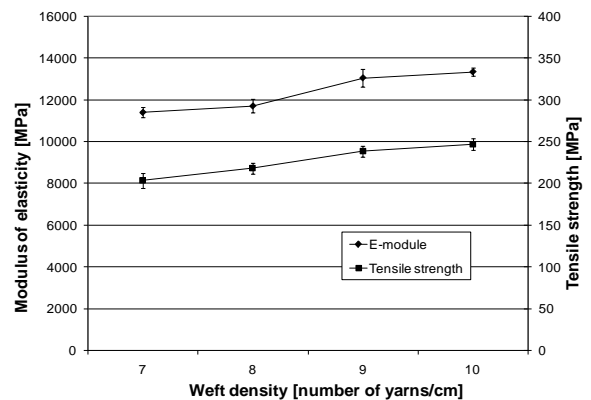


Fig. 20 Modulus and tensile strength of 3 layer consolidated fabrics in weft direction

Bending and impact tests were conducted with two and three layers consolidated woven fabrics. One layer fabrics did not have the sufficient thickness. Flexural strength increases with increasing weft density in the weft direction. However, flexural strength reduces with increasing weft density in the warp direction (Figure 21). Impact strength is mostly affected by the thickness of the samples. Therefore, increasing of weft density and the number of plies increase the total impact energy (Figure 22)

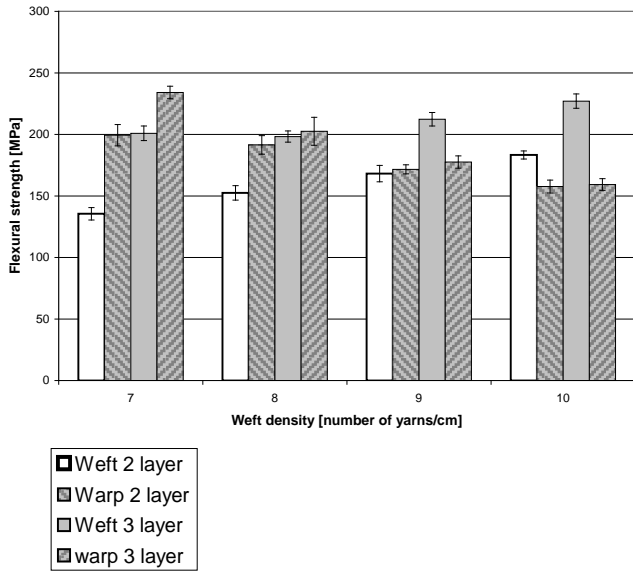


Fig. 21 Flexural strength of 2 and 3 layer consolidated fabrics in warp and weft direction

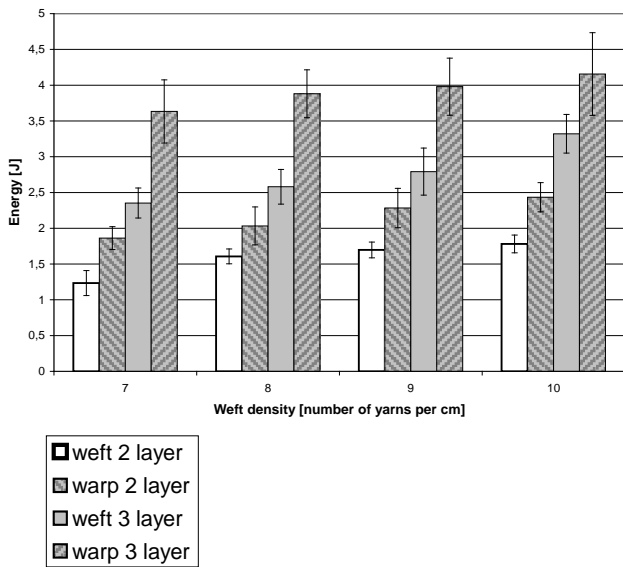


Fig. 22 Impact strength of 2 and 3 layer consolidated fabrics in warp and weft direction

IV. CONCLUSION

Effects of twisting on the mechanical properties of GF/PP commingled yarns are analyzed. This study is initiated through the production stops caused by the open and sticky commingled yarn structure during weaving of dense 3D woven preforms. Twisting decreases the average yarn diameter and creates a more compact and even

structure. In commingled yarns, two distinctive areas can be recognized. These areas have varied mixing quality and yarn consumption. Increases of both E-modulus and tensile strength of commingled yarns are observed until 40 tpm. A statistically confident reduction of E-modulus was observed after 40 tpm. However, UD tensile strength values of twisted samples were around 10% less than the reference commingled yarn. E-module in transverse direction starts decreasing with 20 tpm which correlates with the reduction in yarn diameter. A slight decrease in transverse tensile strength was observed. Twist application on commingled yarns creates more compact yarn structure which can increase productivity in dense woven preform manufacturing. Up to 20 tpm twist levels can be applied where a longitudinal strength reduction of about 10% can be tolerated without any E-modulus reduction. Similar to the investigations of Naik and Kuchibhotla [19] about the twist of glass yarns, the yarn twist does not significantly affect the composite properties up to an optimum twist angle. The influence of the compaction of the yarns by twisting the weavability was not discussed.

Woven fabrics with commingled yarns are subject to extensive deformation in the out-of plane direction when manufactured by hot press molding. Higher weft density increases the final composite thickness. However, it also increases the crimp of warp yarns, thus reduces the in-plane mechanical properties. Increasing weft density increased the damage both on weft and warp yarns. Single, double and triple layers of separate woven fabrics were pressed and consolidated with four different weft densities. In warp direction, significant decrease of modulus and strength was observed mainly due to the increasing crimp of internal structure. In weft direction, a slight increase of modulus and strength with increasing weft density was observed which was caused by the compact reinforcement structure and the reduced resin rich areas.

According to these results, higher crimp which was caused by higher weft density reduces the tensile properties significantly. Therefore, the yarn crimp should be avoided inside the woven structure. It is advantageous for tensile properties to adjust the component thickness by multiple layers of woven fabrics with lower weft density instead of using fewer layers of woven fabrics with higher weft density.

ACKNOWLEDGMENT

The authors would like to thank the German Research Foundation (DFG) for the financial support of the Collaborative Research Centre “Textile-reinforced composite components for function-integrating multi-material design in complex lightweight applications” (SFB 639, TP A3 & A4) at the Technical University of Dresden, Germany. The fruitful cooperation with The Leibniz-Institut für Polymerforschung Dresden e. V. as well as NV Michel Van de Wiele Carpet and Velvet Weaving Machines are highly appreciated.

REFERENCES

[1] Aström, B. T. Manufacturing of Polymer Composites: Nelson Thornes Ltd, Cheltenham, 2002.

- [2] Flemming, M.; Ziegmann, G.; Roth, S. Faserverbundweisen: Halbzeuge und Bauweisen: Springer Verlag, Berlin, 1997.
- [3] Advani, S. G. and Sozer, E.M., Process Modeling in Composite Manufacturing: Marcel Dekker, New York, 2003.
- [4] Offermann P., Wulfhorst, B., Mäder, E. Technische Textilien/ Technical Textiles 1995, 38 (2), 55-57.
- [5] Bernet, N., Michaud, V., Bourban, P.-E., Manson, J.-A. E. Composites, Part A 2001, 32, 1613-1626.
- [6] Bourban, P.-E., Bernet, N., Znaetto, J.-E., Manson, J.-A. E. Composites, Part A 2001, 32, 1045-1057.
- [7] Torun, A. R., Erdem, V., Hoffmann, G., Cherif, Ch. Technische Textilien/Technical Textiles 2009, 52 (3), 142-144, E137-E139
- [8] Torun, A. R., Mountasir, A., Hoffmann, G., Cherif, Ch. JCCM-1, Kyoto, Japan 2010.
- [9] Torun, A. R., Hoffmann, G., Cherif, Ch. 9th Texcomp, Delaware, USA, 2008.
- [10] Lee, B., Leong, K. H., Herszberg, I., Effect of Weaving on the Tensile Properties of Carbon Fibre Tows and Woven Composites, Journal of REINFORCED PLASTICS AND COMPOSITES, Vol. 20, No. 08/2001.
- [11] Rudov-Clarka, S., Mouritza, A. P., Leea, L., Bannister M. K., Fibre damage in the manufacture of advanced three-dimensional woven composites, Composites Part A: Applied Science and Manufacturing, Volume: 34, Issue: 10, Pages: 963-970, 2003.
- [12] Choi, B.-D., Entwicklung von Commingling-Hybridgarnen für langfaserverstärkte thermoplastische Verbundwerkstoffe, Dissertation, Technische Universität Dresden, 2005.
- [13] Eshelby, J. D. Proc Roy Soc 1957, A241, 376-396.
- [14] Eshelby, J. D. Proc Roy Soc 1959, A252, 561-569.
- [15] Hyer, M. W., Stress Analysis of Fiber-Reinforced Composite Materials; McGraw-Hill, 1998.
- [16] Hull, D., Clyne, T. W., An Introduction to Composite Materials: Cambridge University Press, Cambridge, 1996.
- [17] Halpin, J. C., Tsai, S. W., Air Force Materials Laboratory Technical Report 1967, AFML-TR-67, 423
- [18] Torun, A. R., Advanced Manufacturing Technology for 3D Profiled Woven Preforms, Dissertation, Technische Universität Dresden, 2011.
- [19] Naik N. K., Kuchibhotla R., Analytical study of strength and failure behaviour of plain weave fabric composites made of twisted yarns, Composites Part A: Applied Science and Manufacturing, Volume 33, Issue 5, Pages 697-708, 2002.

# Chemical Products Produced from High Density Polyethylene (HDPE) Waste Plastic

Moinuddin Sarker<sup>1</sup>, Mohammad Mamunor Rashid<sup>2</sup>, Muhammad Sadikur Rahman<sup>3</sup>, Mohammed Molla<sup>4</sup>

Natural State Research, Inc. Department of Research and Development, 37 Brown House Road (2<sup>nd</sup> Floor), Stamford, CT 06902, USA

<sup>1</sup>msarker@naturalstateresearch.com; <sup>2</sup>mamun@naturalstateresearch.com; <sup>3</sup>sadik@naturalstateresearch.com; <sup>4</sup>mmolla@naturalstateresearch.com

**Abstract-**Waste high density polyethylene (HDPE) in the form of liquid detergent bottles (white color) was used for this experiment to obtain naphtha grade fuel. The final product consisted of 30% naphtha product in volume and the rest was other grade fuel. The temperature range for the entire liquefaction process was 100-450°C. The naphtha chemical product was collected between 110-135°C. A glass reactor was used for experiment and the fractional column was also glass system and fractional glass was Pyrex glass. Produced chemical product was analyzed by gas chromatography and mass spectrometer and FT-IR. They were used to identify the chemical products band energy determination. Produced naphtha product has short and long chain aliphatic hydrocarbon and chemical product, density is 0.74 gm/ml and it has good Btu value and sulfur content meets the standards according to EPA. This chemical product could be used as a feed stock for other chemical production purposes.

**Keywords-** Chemical Product; Waste Plastic; High Density Polyethylene; HDPE; Thermal Degradation

## I. INTRODUCTION

Currently US generates a large quantity of waste plastics and waste tires each year. All these wastes are discarded and end up in sanitary landfills. As per older standards, only 4% of the waste plastics are reused. Waste plastics occupy approximately 21 vol.% of US landfills as per 1995 survey [1]. Increasing the recycling rate of plastic will require innovative and cost-effective recycling technologies. Recycling plastic back to fundamental feedstock has been one area of active research and shows promise in overcoming many problems plaguing the conventional recycling process. These new technologies have been called "feedstock recycling" or "advanced recycling technologies" and include process such as methanolysis of polyesters and thermal depolymerization of polyolefins [4-6]. Advanced recycling technologies, specifically the thermal depolymerization of polyolefins seems to be the most effective in converting the large amount of waste plastic to resourceful source.

Waste plastic recycling can be categorized into four modes. Primary recycling deals with conversion into products similar in nature to the original product. Secondary recycling involves conversion into products of different forms for less demanding applications. Tertiary recycling converts wastes into basic chemicals or feedstock. Quaternary recycling retrieves energy from wastes through combustion. An example of the last type is incineration of wastes for power generation. Secondary recycling, which

involves grinding, remelting and re-forming of the waste materials into lower-value products such as fillers and fibers, has been a more common practice for waste plastic until now [6-11]. Even though these methods are currently being applied, the feasibility of these methods in the future is not very possible. The slim possible chance is due to the large amount of waste plastic that is generated, and also different plastics have different types of characteristics which make it difficult to apply the different recycling methods [12-14].

Thermal degradation of converting waste plastic to liquid hydrocarbon materials is an economically and environmentally accepted method for converting the large amount of waste plastics. The products of such processes are liquid mixtures of hydrocarbons boiling in the temperature range 35-360 °C, gaseous hydrocarbons as well as solid residue, similar to wax and coke. Through the years excellent results have been obtained from liquefaction of individual polymers (Polyethylene (PE), Polypropylene (PP), Polystyrene (PS) etc.) and relatively clean mixed plastics using solid acid catalysts and metal-promoted solid acid catalysts. For example, Venkatesh et al. [3] and Shabtai et al. [4] have obtained high yields of liquids that consist predominantly of isoalkanes in the gasoline boiling range from HDPE, PP, and PS at relatively low temperature (300-375°C) using similar metal catalysts mentioned above. In this particular study, we are conducting a thermal degradation process utilizing waste high density polyethylene as a raw material. High density polyethylene is a large part of the waste plastic composition. One particular difference in this study was that no forms of catalysts were utilized during the conversion process. The conversion process is described in detail in the method section.

## II. MATERIALS & METHOD

### A. Materials

Waste plastic collected from local municipalities were mixed with HDPE, LDPE code and non-coded such as grocery bag, milk container, juice container, liquid detergent bottle etc. Waste plastics were a mixture of soft shape and hard shape. Collected waste plastic included foreign materials. Separated all kind of foreign materials and washed with soap then cut into small pieces manually. HDPE waste plastic was use for this experiment as a raw materials and it was wash with water and liquid detergent. HDPE waste plastic was detergent bottle and it was hard shape plastic and HDPE plastic color was white color.

### B. Experimental Process

HDPE white color liquid detergent bottle was used for liquefaction process by using small glass reactor with fractional distillation column. Liquefaction temperature range for liquefaction process was 100~450 °C. HDPE waste plastics were cut into small pieces and put into the reactor to set up the fractional distillation column with various temperatures to collect different grade fuels. Fig.1 showed chemical product collection process. Glass fractional distillation column set up with reactor and chemical naphtha was collected. Number 11 in the diagram is where the naphtha chemical is collected. Reactor temperature was monitored using variac. Reactor setup showed in diagram: 1 = HDPE waste plastic, 2= Glass reactor, 3 = Fractional distillation column, 4= 1<sup>st</sup> fraction temperature, 5= 2<sup>nd</sup> fraction temperature, 6=3<sup>rd</sup> fraction temperature, 7= 4<sup>th</sup> fraction temperature, 8= 5<sup>th</sup> fraction temperature, 9= light gas cleaning system, 10= 1<sup>st</sup> fraction fuel collection tank, 11=2<sup>nd</sup> fraction fuel collection tank, 12=3<sup>rd</sup> fraction fuel collection tank, 13=4<sup>th</sup> fraction fuel collection tank, 14 = 5<sup>th</sup> fraction fuel collection tank, 15 = small pump, 16 = Teflon bag for light gas storage. Waste

plastic used for experimental process was measured 500 gm by weight. Reactor was heated up from 100°C to up to 450°C gradually. Fractional column temperature was used for 1<sup>st</sup> fraction at 40 ~ 65°C, 2<sup>nd</sup> fractional column temperature was used 110~135°C, 3<sup>rd</sup> fractional column temperature was used 180 ~ 205°C, 4<sup>th</sup> fractional temperature was used 260~28 °C and finally 5<sup>th</sup> fraction temperature was used 340 ~ 365°C. Main goal of this particular experiment was to collect 2<sup>nd</sup> fraction fuel. Fuel collection percentage was 29% for the 2<sup>nd</sup> collection (naphtha chemical). During fractional distillation process some light gas was generated at around 5% and solid black residue was 4% and rest of percentage other grade fuels was 62% which is demonstrated in diagram number 10, 12, 13 and 14 collection tank. Chemical production process light gas was passing (through number 9) liquid alkali solution for removing contamination and small pump was for light gas to transfer into Teflon bag. Collected chemical product purified using RCI purification unit to remove water and ash contents from the fuel. The 2<sup>nd</sup> fraction fuel density is 0.74 g/ml and fuel was transparent and fuel color was light yellow.

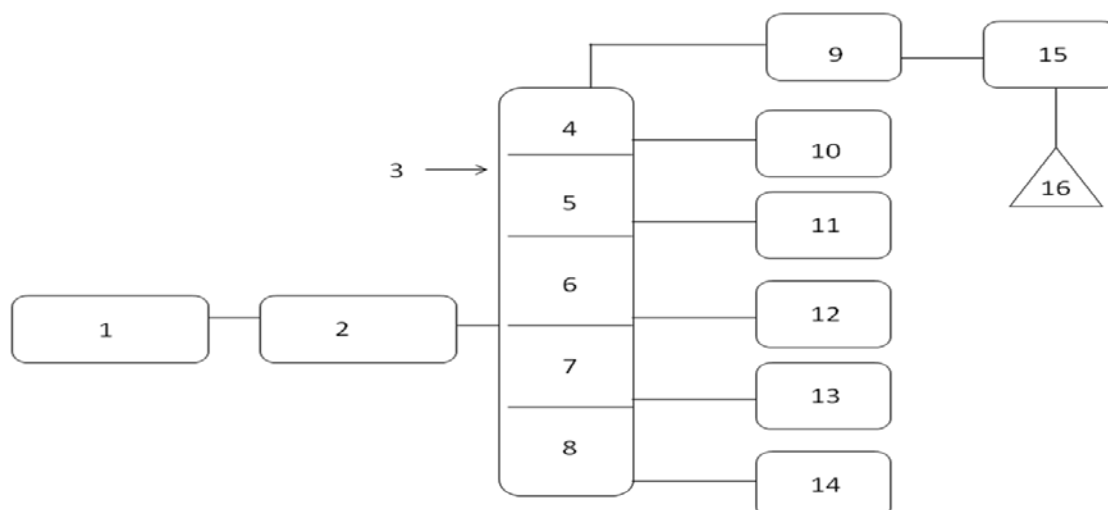


Fig. 1 HDPE waste plastic to chemical production process

## III. ANALYSIS RESULTS & DISCUSSION

### A. Analysis Techniques

Perkin Elmer GC/MS was used for liquid product analysis. GC/MS model number Clarus 500 and carrier gas was helium, 30 m length capillary column was used for Gas chromatography, and EI detector was used for compound mass detection. Auto sampler process was used for GC/MS analysis and sample was used only 5 µL. GC temperatures used for analysis were 40 to 325°C and rate was 10°C/min and MS mass detection was 35.00 ~ 528.00 EI+. FT-IR spectrum 100 was used for liquid product analysis purposed and NaCl cell was used for sample holding and cell thickness was 0.25 mm, range was 4000-400 cm<sup>-1</sup>, resolution was 4 and scene number was 32.

### B. Liquid Products Analysis

By using GCMS (Model Clarus 500) analysis of HDPE waste plastic to 2<sup>nd</sup> fractional fuel or chemical product (Fig. 2 and Table 1) in accordance with retention time and trace mass indicate various types of compound are present. HDPE 2<sup>nd</sup> fraction is collected at 110°C during experiment. High intensity compounds are preferred in the analysis. An investigated carbon range in the analyzed fuel is C<sub>4</sub> to C<sub>15</sub> because by fractional distillation large carbon chains are breaking down into small chain, resulting in lower carbon range. Most of the peaks are considered in the analysis and as per their retention time and trace mass maximum peaks are mentioned, in accordance to retention time 1.64 and trace mass 43 derived compound is Butane (C<sub>4</sub>H<sub>10</sub>), retention time 1.89 and trace mass 42, compound is Cyclopropane, 1, 2-dimethyl-, cis-(C<sub>5</sub>H<sub>10</sub>), retention time 1.93, trace mass 43 compound is Cyclopropane, 1, 2-dimethyl-, cis- (C<sub>5</sub>H<sub>10</sub>), retention time 2.08, trace mass 67 compound is 1, 3-Pentadiene (C<sub>5</sub>H<sub>8</sub>), retention time 2.34

and trace mass 42 compound is Butane, 2, 3-dimethyl- ( $C_6H_{14}$ ), retention time 2.52, trace mass 56, compound is 1-Pentene, 2-methyl- ( $C_{13}H_{28}$ ), retention time 2.60 and trace mass 56, compound is Hexane ( $C_6H_{14}$ ), retention time 2.92 and trace mass 56, compound is Cyclopentane, methyl- ( $C_6H_{12}$ ), retention time 3.16 and trace mass 67, compound is Cyclopentene, 1-methyl-, ( $C_6H_{10}$ ), retention time 3.32 and trace mass 41, compound is Cyclohexane ( $C_6H_{12}$ ), retention time 3.66 and trace mass 56, compound is 2-Heptene ( $C_7H_{14}$ ), retention time 3.79 and trace mass 57, compound is Heptane ( $C_7H_{16}$ ), retention time 4.10 and trace mass 41, compound is Cycloheptene ( $C_7H_{12}$ ), retention time 4.33 and trace mass 69, compound is Cyclopentane, ethyl- ( $C_7H_{14}$ ) etc. Also in the middle of the analysis index retention time 4.63 and trace mass 67, compound is Cyclopentane, ethylidene, ( $C_7H_{12}$ ), retention time 4.89 and trace mass 67, compound is Cyclohexene, 1-methyl-, ( $C_7H_{12}$ ), retention time 5.20 and trace mass 41, compound is 2-Octene, (Z), ( $C_{18}H_{16}$ ), retention time 5.27 and trace mass 55, compound is Cyclopentane, 1-ethyl-2-methyl-, cis- ( $C_8H_{16}$ ), retention time 5.35 and trace mass 43, compound is Octane ( $C_8H_{18}$ ), retention time 5.84 and trace mass 67, compound is 1-Methyl-2-methylenecyclohexane, ( $C_8H_{14}$ ), retention time 6.02 and trace mass 83, compound is ethylcyclohexane,

( $C_8H_{16}$ ), retention time 6.16 and trace mass 67, compound is Cyclopentene-1-Propyl ( $C_8H_{14}$ ), retention time 6.59 and trace mass 81, Cyclohexene-1-Ethyl ( $C_8H_{14}$ ), retention time 7.06 and trace mass 43, compound is Nonane ( $C_9H_{20}$ ), retention time 7.70 and trace mass 55 Compound is Cyclohexane, propyl- ( $C_9H_{18}$ ), retention time 8.63 and trace mass 41, compound is Decene ( $C_{10}H_{20}$ ), retention time 8.67 and trace mass 57, compound is Decane ( $C_{10}H_{22}$ ), retention time 10.27 and trace mass 41, compound is 1-Undecene, ( $C_{11}H_{22}$ ), retention time 10.41 and trace mass 57, compound is Undecane ( $C_{11}H_{24}$ ), retention time 11.83 and trace mass 41, compound is 1-Dodecane ( $C_{12}H_{24}$ ), retention time 11.95 and trace mass 57, compound is Tridecane ( $C_{12}H_{26}$ ), etc. At the end phase of the analysis index high retention time and trace mass such as retention time 13.29 and trace mass 41, compound is 1-Tridecane ( $C_{13}H_{26}$ ), retention time 13.41, trace mass 57 compound is Tridecane ( $C_{14}H_{30}$ ), retention time 14.68, trace mass 41 compound is 1-Tetradecene, retention time 14.78, trace mass compound is Tetradecane ( $C_{14}H_{30}$ ), retention time 15.98, trace mass 55 compound is 1-Pentadecene and ultimately retention time 16.09, trace mass 57, compound is Pentadecane ( $C_{15}H_{32}$ ), etc.

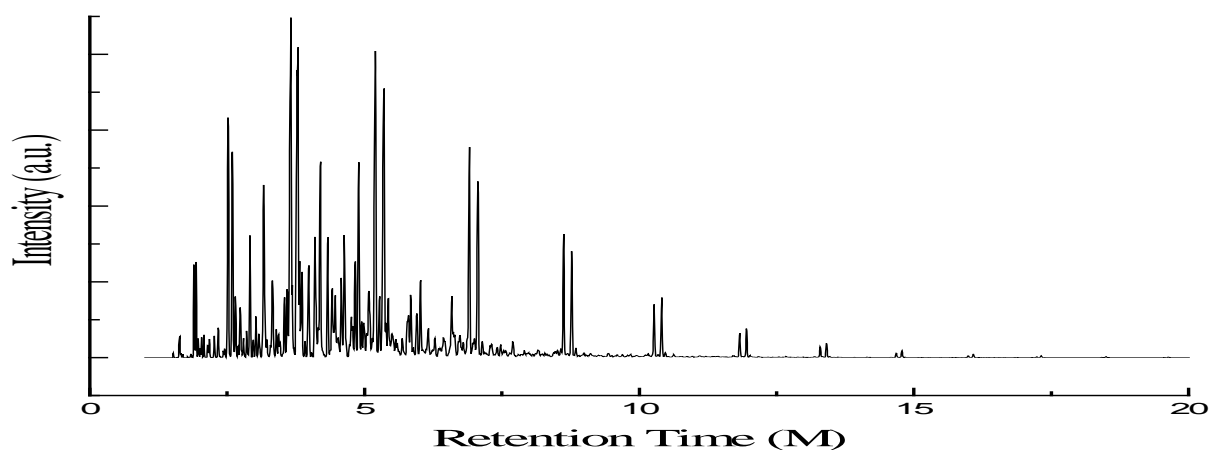


Fig. 2 GC/MS Chromatogram of HDPE waste plastic to chemical product

TABLE I GC/MS CHROMATOGRAM OF HDPE WASTE PLASTIC TO CHEMICAL PRODUCT COMPOUND LIST

Number of Peak	Retention Time (min)	Trace Mass ( $m/z$ )	Compound Name	Compound Formula	Molecular Weight	CAS Number
1	1.64	43	Butane	$C_4H_{10}$	58	106-97-8
2	1.89	42	Cyclopropane, 1,2-dimethyl-, cis-	$C_5H_{10}$	70	930-18-7
3	1.93	43	Pentane	$C_5H_{12}$	72	109-66-0
4	2.08	67	1,3-Pentadiene	$C_5H_8$	68	504-60-9
5	2.34	42	Butane, 2,3-dimethyl-	$C_6H_{14}$	86	79-29-8
6	2.52	56	1-Pentene, 2-methyl-	$C_6H_{12}$	84	763-29-1
7	2.60	56	Hexane	$C_6H_{14}$	86	110-54-3
8	2.92	56	Cyclopentane, methyl-	$C_6H_{12}$	84	96-37-7
9	3.16	67	Cyclopentene, 1-methyl-	$C_6H_{10}$	82	693-89-0
10	3.32	41	Cyclohexane	$C_6H_{12}$	84	110-82-7
11	3.66	56	2-Heptene	$C_7H_{14}$	98	592-77-8
12	3.79	57	Heptane	$C_7H_{16}$	100	142-82-5
13	4.10	41	Cycloheptene	$C_7H_{12}$	96	628-92-2

14	4.33	69	Cyclopentane, ethyl	C <sub>7</sub> H <sub>14</sub>	98	1640-89-7
15	4.63	67	Cyclopentane, ethylidene-	C <sub>7</sub> H <sub>12</sub>	96	2146-37-4
16	4.89	67	Cyclohexene, 1-methyl-	C <sub>7</sub> H <sub>12</sub>	96	591-49-1
17	5.20	41	2-Octene, (Z)-	C <sub>8</sub> H <sub>16</sub>	112	7642-04-8
18	5.27	55	Cyclopentane, 1-ethyl-2-methyl-, cis-	C <sub>8</sub> H <sub>16</sub>	112	930-89-2
19	5.35	43	Octane	C <sub>8</sub> H <sub>18</sub>	114	111-65-9
20	5.84	67	1-Methyl-2-methylenecyclohexane	C <sub>8</sub> H <sub>14</sub>	110	2808-75-5
21	6.02	83	Cyclohexane, ethyl-	C <sub>8</sub> H <sub>16</sub>	112	1678-91-7
22	6.16	67	Cyclopentene, 1-propyl-	C <sub>8</sub> H <sub>14</sub>	110	3074-61-1
23	6.59	81	Cyclohexene, 1-ethyl-	C <sub>8</sub> H <sub>14</sub>	110	1453-24-3
24	6.91	56	1-Nonene	C <sub>9</sub> H <sub>18</sub>	126	124-11-8
25	7.06	43	Nonane	C <sub>9</sub> H <sub>20</sub>	128	111-84-2
26	7.70	55	Cyclohexane, propyl-	C <sub>9</sub> H <sub>18</sub>	126	1678-92-8
27	8.63	41	1-Decene	C <sub>10</sub> H <sub>20</sub>	140	872-05-9
28	8.77	57	Decane	C <sub>10</sub> H <sub>22</sub>	142	124-18-5
29	10.27	41	1-Undecene	C <sub>11</sub> H <sub>22</sub>	154	821-95-4
30	10.41	57	Undecane	C <sub>11</sub> H <sub>24</sub>	156	1120-21-4
31	11.83	41	1-Dodecene	C <sub>12</sub> H <sub>24</sub>	168	112-41-4
32	11.95	57	Dodecane	C <sub>12</sub> H <sub>26</sub>	170	112-40-3
33	13.29	41	1-Tridecene	C <sub>13</sub> H <sub>26</sub>	182	2437-56-1
34	13.41	57	Tridecane	C <sub>13</sub> H <sub>28</sub>	184	629-50-5
35	14.68	41	1-Tetradecene	C <sub>14</sub> H <sub>28</sub>	196	1120-36-1
36	14.78	57	Tetradecane	C <sub>14</sub> H <sub>30</sub>	198	629-59-4
37	15.98	55	1-Pentadecene	C <sub>15</sub> H <sub>30</sub>	210	13360-61-7
38	16.09	57	Pentadecane	C <sub>15</sub> H <sub>32</sub>	212	629-62-9

FT-IR Spectrum-100 analysis of HDPE waste plastic to chemical product (Fig. 3 and Table 2) in favor of wave number, several types of functional groups are present. In accordance with wave number 2959.01 cm<sup>-1</sup>, 2732.21 cm<sup>-1</sup> and 2669.08 cm<sup>-1</sup> functional group is C-CH<sub>3</sub>, wave number 1822.20 cm<sup>-1</sup> and 1717.18 cm<sup>-1</sup> compound is Non-Conjugated and wave number 1642.41 cm<sup>-1</sup>, functional group is Conjugated. Then wave number 1471.60 cm<sup>-1</sup>, functional group is CH<sub>2</sub>/CH<sub>3</sub>, wave number 1378.66 cm<sup>-1</sup>, functional group is -CH<sub>3</sub>, wave number 993.43 cm<sup>-1</sup> and 905.90 cm<sup>-1</sup>, functional group is -CH=CH<sub>2</sub>, ultimately wave number 965.22 cm<sup>-1</sup>, functional group is -CH=CH-(trans) as well as wave number 726.87 cm<sup>-1</sup>, 694.24 cm<sup>-1</sup> and 674.73 cm<sup>-1</sup> functional group is -CH=CH-(cis). Energy value are calculated, using formula is Energy=hv, where h=plank constant, v=frequency of photon and v=cW, therefore, E=hcW, where C=the speed of light (3x10<sup>10</sup> cm/sec), W=wave number in cm<sup>-1</sup>. According to equation

high wave number light has more energy than low wave number light such as wave number 2959.01 cm<sup>-1</sup> (C-CH<sub>3</sub>), energy=5.87X10<sup>-20</sup> J, wave number 2732.21 cm<sup>-1</sup> (C-CH<sub>3</sub>), energy=5.42X10<sup>-20</sup> J, wave number 2669.08 cm<sup>-1</sup> (C-CH<sub>3</sub>), energy=5.30X10<sup>-20</sup> J, wave number 1822.20 cm<sup>-1</sup> (Non-Conjugated) energy, E=3.61X10<sup>-20</sup> J, wave number 1717.18 cm<sup>-1</sup> (Non-Conjugated) energy, E=3.41X10<sup>-20</sup> J, wave number 1641.86 cm<sup>-1</sup> (Conjugated) energy, E=3.26X10<sup>-20</sup> J, wave number 1471.60 cm<sup>-1</sup> (CH<sub>2</sub>/CH<sub>3</sub>) energy, E=2.92X10<sup>-20</sup> J, wave number 1378.66 cm<sup>-1</sup> (CH<sub>3</sub>) energy, E=2.73X10<sup>-20</sup> J, wave number 993.43 cm<sup>-1</sup> (-CH=CH<sub>2</sub>) energy, E=1.97x10<sup>-20</sup> J, wave number 965.22 cm<sup>-1</sup> (-CH=CH-(cis)) energy, E=1.91x10<sup>-20</sup> J, wave number 905.90 cm<sup>-1</sup> (-CH=CH<sub>2</sub>) energy, E=1.80x10<sup>-20</sup> J, wave number 726.87 cm<sup>-1</sup> (-CH=CH- (cis), energy, E=1.44 x10<sup>-20</sup> J, wave number 694.24 cm<sup>-1</sup> (-CH=CH- (cis)), energy, E=1.37 x10<sup>-20</sup> J and ultimately wave number 674.73 cm<sup>-1</sup> (-CH=CH- (cis)), energy, E=1.34 x10<sup>-20</sup> J as well.

TABLE II HDPE WASTE PLASTIC TO HDPE WASTE PLASTIC TO CHEMICAL PRODUCT FUNCTIONAL GROUP NAME

Number of Wave	Wave Number (cm <sup>-1</sup> )	Functional Group Name	Number of Wave	Wave Number (cm <sup>-1</sup> )	Functional Group Name
1	2959.01	C-CH <sub>3</sub>	8	1378.66	CH <sub>3</sub>
2	2732.21	C-CH <sub>3</sub>	9	993.43	-CH=CH <sub>2</sub>
3	2669.08	C-CH <sub>3</sub>	10	965.22	-CH=CH-(trans)
4	1822.20	Non-Conjugated	11	905.90	-CH=CH <sub>2</sub>
5	1717.18	Non-Conjugated	12	726.87	-CH=CH-(cis)
6	1641.86	Conjugated	13	694.24	-CH=CH-(cis)
7	1471.60	CH <sub>2</sub> / CH <sub>3</sub>	14	674.73	-CH=CH-(cis)

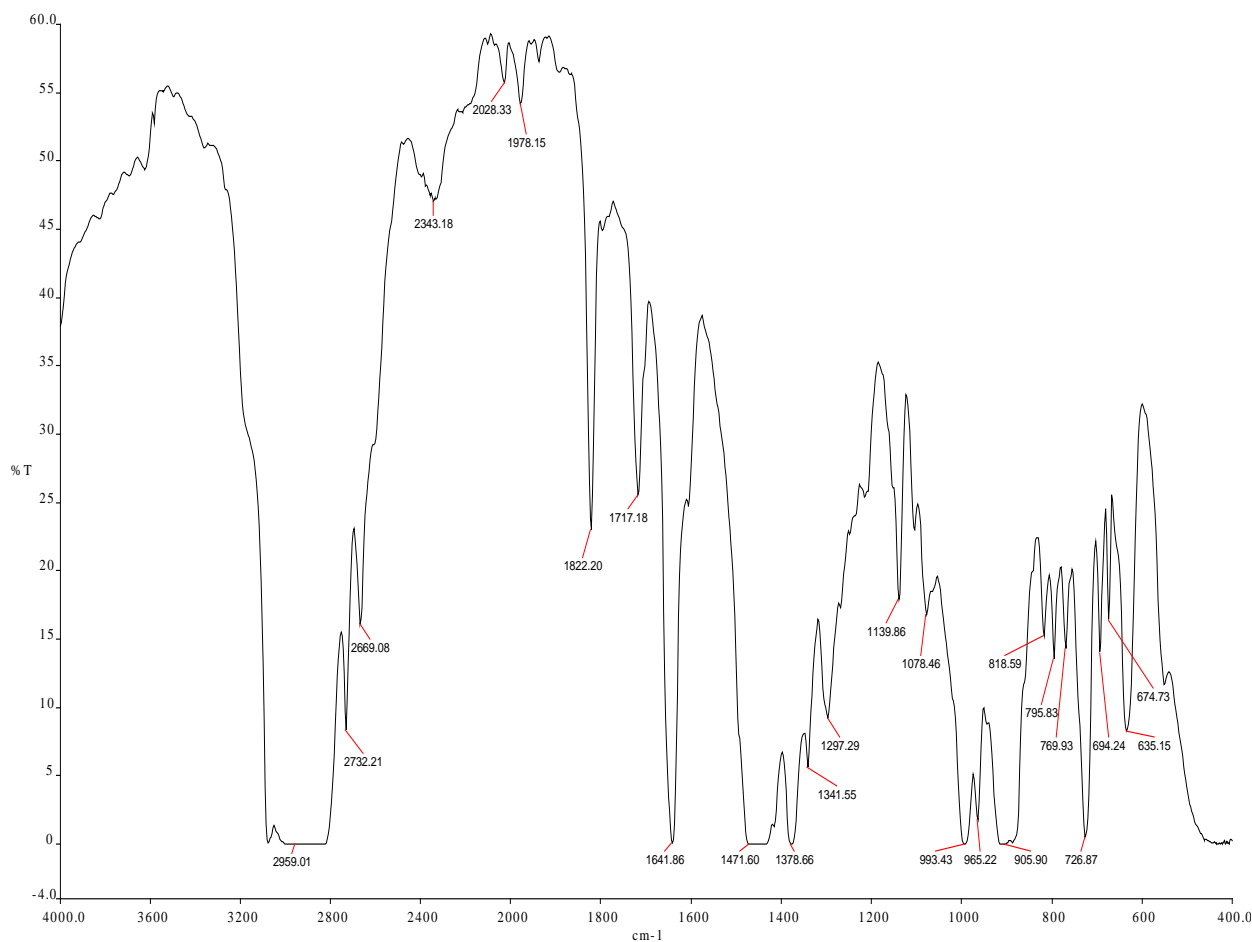


Fig. 3 FT-IR Spectrum of HDPE waste plastic to chemical product

DSC analysis of HDPE plastic to 2nd fraction fuel or chemical product (Fig. 4) indicates the onset temperature of 141.14°C. The peak temperature of the fuel is 145.80°C. Peak height is 90.7354 mW and heat flow Endo up from 100 to 95%. Peak area is 18873.444 mJ, heat enthalpy value delta H is 18873.4467 J/g. This fuel peak temperature is

145.80°C and fuel collection temperature was 110-135°C and carbon range for fuel C<sub>4</sub> to C<sub>15</sub>. From analysis graph showed 50°C temperature fuel boil 13.87%, 92% fuel boil finished at 250°C and finally 396.69°C temperature need for whole fuel boiled because this fuel has short chain hydrocarbon C<sub>4</sub> to long chain hydrocarbon C<sub>15</sub>.

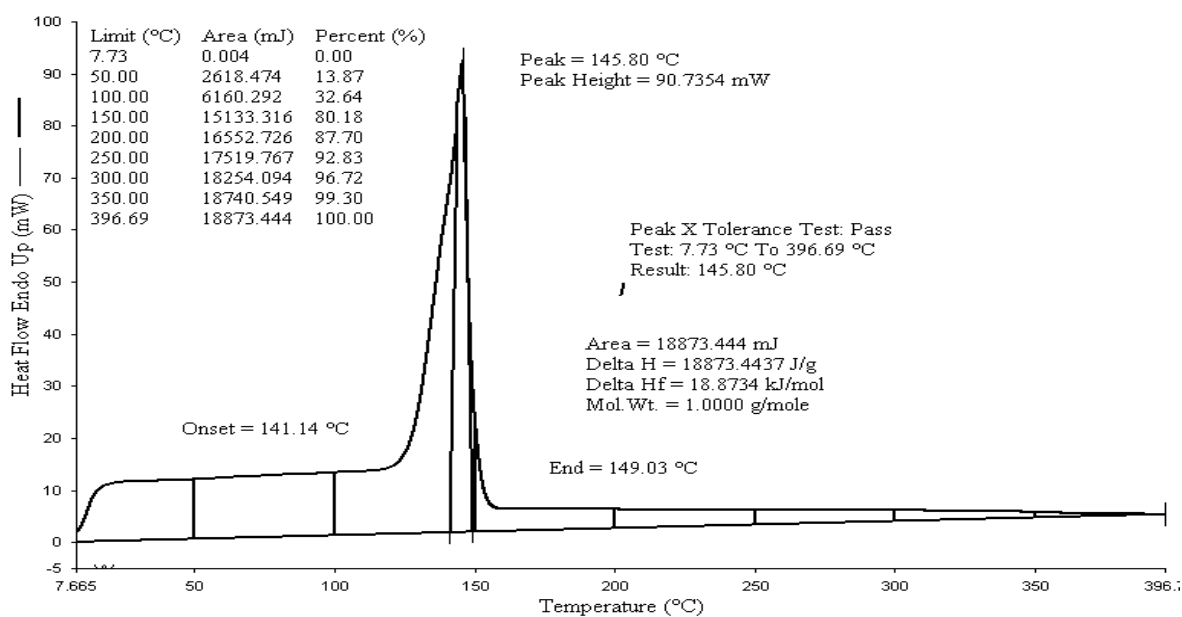


Fig. 4 DSC graph of HDPE plastic to chemical product

Some ASTM test was performed for chemical product such as n-paraffins, Iso-paraffins, Olefins, Naphthenes, Aromatics, naphthenes and aromatics by volume (ASTM D5134\_MOD), sulfur (ASTM D5453), Heat gross of combustion (ASTM D240), Density @ 15°C (ASTM D4052), API gravity @ 60 °F (ASTM D4052), IBP recovery (ASTM D86), Dry vapor pressure equivalent EPA (ASTM D5191), Metal content (ASTM D5708\_MOD), Appearance (ASTM D4176), Acid Number (ASTM D974), CHN Percentage (ASTM D5291), C and H ratio (ASTM D5291).

#### IV. CONCLUSION

Chemical product produced from HDPE waste plastic by using fractional distillation process. Temperature range was setup for particular chemical product 110-135°C. Chemical product conversion rate was good percentage from HDPE waste plastic. Analysis of chemical product result shows short to long chain aliphatic hydrocarbon mostly alkane and alkene group compounds are present. Carbon range showed from GC/MS analysis C<sub>4</sub> to C<sub>15</sub>. By using this technology waste plastic could be removed from land fill and save the environment and support the chemical sector. GCMS (Gas

Chromatography and Mass Spectrometer) analysis of HDPE 2<sup>nd</sup> fraction fuel which is similar to naphtha or chemical product found that numerous aliphatic and aromatic compounds are available in accordance with their retention time and trace mass. In some cases appeared that at high retention time and high trace mass high peak intensity compound are appeared versus at low retention time and low trace mass low peak intensity compounds are emerged as well. GCMS analyses gave actual entirety of compounds which is present in the fuel entity. FT-IR (Fourier Transform Infra-red Spectrometer) analysis is giving the exact availability of hydrocarbon functional groups in the fuel including other organic and inorganic functional groups. In addition ASTM (American Standard and Testing Method) also performed some test in order to characterize the fuel properties. ASTM analysis makes sure and derived some alkene compounds such as paraffin's, olefins, naphthenes as well as aromatic compound constituents of naphtha or chemical products. DSC (Differential Scanning Calorimeter) represents the onset temperature of fuel products which is melting point of the products. In addition DSC analysis also provides percentage of burning contents versus temperature profile limit with consumed mJ (milli joule) as well as peak and peak heights which is compared to other chemical standard products respectively.

#### ACKNOWLEDGEMENT

The author acknowledges the support of Dr. Karin Kaufman, the founder and sole owner of Natural State Research, Inc., (NSR). The authors also acknowledge the valuable contributions NSR laboratory team members during the preparation of this manuscript.

#### REFERENCES

[1] S. H. Ng, H. Seoud, M. Stanculescu, and Y. Sugimoto, *Energy & Fuels*, 1995, 9, 735.

- [2] A. R. Songip, T. Masuda, H. Kuwahara, K. Hashimoto, *Energy & Fuels*, 1994, 8, 131.
- [3] K. R. Venkatesh, J. Hu, W. Wang, G. D. Holder, J. W. Tierney, I. Wender. *Energy Fuels* 1996; 10: 1163- 1170.
- [4] J. Shabtai, X. Xiao, W. Zmierzak. *Energy Fuels* 1197; 11: 76-87.
- [5] M. Tangiei, M. Feng, Z. Fenz, F. Huggins, G. Huffman. *Energy & Fuels*, 1994, 8, 1228.
- [6] H. Kastner, and W. Kaminsky, *Hydrocarbon processing*, 1995, 74(5), 109
- [7] Z. Feng, J. Zhao, J. Rockwell, D. Bailey, G. Huffman, *Fuel processing technology*, 1996, 49, 17.
- [8] *Advanced recycling of plastics*, final report with the American Plastic Council. 1995.
- [9] P. Ramdoss and A. Tarrer, *Energy & Fuels*, 1996, 10, 996.
- [10] P. Ramdoss and A. Tarrer, *Energy & Fuels*, 1997, 51, 83.
- [11] G. Robbins, R. Winschel, and F. Burke. *ACS preprint*, American Chemical Society, 1996.
- [12] A. Ayame, Y. Uemichi, T. Yoshida, H. Kanoh, J. Jpn. *Petroleum Inst.* 1979, 22, 280.
- [13] A. Ayame, Y. Uemichi, T. Yoshida, H. Kanoh, J. Jpn. *Petroleum Inst.* 1980, 23, 35.
- [14] V. Weekman and D. Nace, *AIChE Journal*, 1970, 16, 397.



Moinuddin Sarker, PhD, MCIC, is the Executive Vice President (EVP), CTO and Chief Operating Officer (COO) at the Natural State Research (NSR), Inc at Stamford, CT and the inventor of NSR's award winning technology to convert municipal waste plastics into liquid hydrocarbon fuel. He has a Ph. D. degree in Chemistry from University of Manchester Institute of Science and Technology (UMIST), Manchester, UK (1996). He has more than 20 years of professional research experience in different universities and research organizations all over the world including the US, Canada, the Netherlands, Germany, Taiwan, Bangladesh and the UK. During his research work, he carried out research in four different synchrotron radiation sources around the world: CRCL lab. Daresbury, Warrington, Cheshire, UK (1991-1996), Synchrotron Radiation Research Center (SRRC), Hsinchu, Taiwan, R.O.C (1996-1999), Berlin Electron Storage Ring Company for Synchrotron Radiation (BESSY II) (2000) and Advance Photon Sources (APS), Chicago, USA (2001-2004). He has two patent pending and 55 research publications to his credit in peer reviewed journals and conferences. Dr. Sarker is a distinguished member of 25 professional organizations such as Society of Automobile International (SAE), American Chemical Society (ACS), American Physical Society (APS), American Institute of Chemical Engineering (AIChE), International Union of Pure and Applied Chemistry (IUPAC), Canadian Society for Chemistry (CSC), Chemical Institute of Canada (CIC), Canada and many more. Dr. Sarker has been invited speaker various conferences in around the USA and World. Dr. Sarker is the inventor of the technology and product entitles: "**Method for converting waste plastics to lower – molecular weight hydrocarbons, particularly hydrocarbon fuel materials and the hydrocarbon material produced thereby**" (US and International Patent Pending). Dr. Sarker also heads a humanitarian effort in Bangladesh, the Moinuddin Foundation ([www.moinuddinfoundation.org](http://www.moinuddinfoundation.org)) which helps provide essentials for the poor and underprivileged.



Mohammad Mamunor Rashid born 1976 into Bangladesh and now he becomes USA citizen. He finished his M. Sc degree in Chemistry from Jagannath University College under National University in Bangladesh. He received his B. Sc and M. Sc degree 2000 and 2002. He is working now Natural State Research, Inc. since 2006 as Plant Manager waste plastic to fuel conversion process and save the environment field. He is co-author of several publications about waste plastic to fuel related journal. He has almost 35 publications into various journals. He has participated seminar and conference. E-mail address: mamun@naturalstateresearch.com



Muhammad Sadikur Rahman, from Bangladesh, Permanent Resident of USA, lives in New York. He obtained his B. Sc (Hon's) 2001, M. Sc in Chemistry 2003 from M.C College under National University of Bangladesh. He has been working in the research and development field as a laboratory

Chemist in the company of Natural State Research, Inc. He is co-author of several publications about waste plastic to fuel related journal. He has almost 15 publications into various journals. He has participated seminar and conference. E-mail address: sadik@naturalstateresearch.com



Mohammed Molla, he born 1986 into Bangladesh and now he is USA Citizen. He is studying B. Sc at City College of NY under CUNY. He is working Natural State Research, Inc as an Intern. He is co-author of several publications about waste plastic to fuel related journal. He has almost 20 publications into various journals. He has participated seminar and conference. E-mail address: mmolla@naturalstateresearch.com

# Damage Modeling of Graded Ti-based Composites Using Repeated Unit Cell Approach

C. Y. Tang<sup>1</sup>, C. P. Tsui<sup>\*2</sup>, Y. Q. Guo<sup>3</sup>, B. Gao<sup>4</sup>, R. H. Luan<sup>5</sup>

<sup>1,2,3</sup>Department of Industrial and Systems Engineering, the Hong Kong Polytechnic University  
Hung Hom, Kowloon, Hong Kong, P.R. China

<sup>4,5</sup>Department of Prosthodontics, College of Stomatology, The Fourth Military Medical University, Xi'an, 710032, P.R. China  
<sup>1</sup>mfcytang@inet.polyu.edu.hk; <sup>\*2</sup>mfgary@inet.polyu.edu.hk;

<sup>3</sup>yunqiang.guo@gmail.com; <sup>4</sup>gaobo@fmmu.edu.cn; <sup>5</sup>rhluan@fmmu.edu.cn

**Abstract-** In the present study, macroscopic mechanical behaviors of titanium-based functionally graded biomaterials (FGMs) under the influence of composite damage have been investigated using the repeated unit cell approach. Based on the proposed method, the FGMs were idealized to be composed of finite uniform layers, each of which is represented by one repeated unit cell. The titanium (Ti) matrix is modeled as an isotropic hardening elastic plastic solid following the incremental ( $J_2$ ) theory of plasticity. As the strength and fracture toughness of hydroxyapatite (HA) inclusion is very weak as compared with the Ti metal, the HA particles may be broken firstly when the composite is subjected to an excessive load. The brittle failure criterion has been implemented in the VUMAT subroutine using the finite element software ABAQUS. A uniaxial tension test along the y-axis of the unit cell has been simulated. The simulation results show that the load-bearing capability of Ti/HA FGMs will decrease rapidly with the increase in the volume fraction of HA. Due to the absence of the load bearing capability of HA, the mechanical behaviors of unit cell are similar to those of a porous structure and the applied load is entirely carried by the Ti matrix. The computational results indicate that this method is capable of predicting the failure process of Ti/HA FGMs.

**Keywords-** Functionally Graded Biomaterials; Repeated Unit Cell; Brittle Failure; Damage

## I. INTRODUCTION

In recent years, there has been increasing attention to the development of biocomposites for load-bearing orthopedic applications, because the mechanical and biological properties of biocomposites can be tailored for specific application by varying the amount and type of constituent materials [1-5]. Hydroxyapatite (HA), a bioactive ceramic material, has outstanding osteoconductivity, enabling bone to form or to adhere to its surface [6, 7]. However, the low tensile strength and poor impact strength of HA have hindered its use in load-bearing applications. Titanium (Ti) and its alloys have been used in several implant applications due to its excellent mechanical behaviors and bioinert oxide surface. However, they suffer certain disadvantages, such as poor osteoinductive properties. Therefore, significant research efforts have been made on improving bioactivity of Ti by coating its oxide surface with HA [8]. However, the HA coating layer often breaks down mechanically. To resolve the limitation of the HA coating, the conception of functionally graded biomaterials (FGMs) may be applied for designing implant. Titanium/Hydroxyapatite (Ti/HA) FGMs

can be fabricated successfully by a laser rapid forming method [9], which makes full use of the excellent bioactivity of HA as well as the high strength and toughness of Ti. This type of implant can provide more Ti for the upper part to withstand the occlusal force, and more apatite for the lower part for implantation into the jaw bone [10].

Material damage and its evolution govern the fracture behavior of FGMs that provides essential knowledge for damage tolerance and defect assessment in structural design. In contrast with the relatively extensive literature on the quasi-static and dynamic behavior of cracks in FGMs [11-13], attempts to study the material damage of FGMs quantitatively by relating the micro-structural damage to the mechanical response of a FGM have not been reported. It is usually very difficult and almost impossible to investigate FGM structural problems analytically. Therefore, applications of finite element method (FEM) [14] in investigating fracture behaviors of FGMs under mechanical or thermal loading have been an active area recently. Under excessive loading, the brittle failure of HA particles can occur in Ti/HA FGMs. So far, there is no method with which internal damage phenomena and the microscopic fracture process of FGMs can be satisfactorily predicted. Therefore, it is necessary to establish a method of bridging the microstructural damage mechanical mechanism and the macrostructural behaviour.

This study, based on the previous work on investigating the microscopic mechanical behavior of Ti/HA FGMs [15], not only provided the detailed implementation of the previous work but also focused on modeling the effect of composite damage on the macroscopic mechanical behavior of Ti/HA FGMs. In order to consider two phase microstructure and gradual variation of mechanical properties in FGMs, a repeated unit cell approach has been proposed. And the brittle failure criteria of HA has been implemented in the VUMAT subroutine using the finite element software package—ABAQUS. Using the proposed method, the microscopic damage behavior of Ti/HA composite and hence the macroscopic mechanical behavior of Ti/HA FGMs could be simulated.

## II. REPEATED UNIT CELL APPROACH

Due to graded microstructure, the local field in FGMs not only changes greatly between two phases, but also

varies spatially in the gradation direction. The distribution of HA particles has a graded variation in the longitudinal direction. For simplicity, the shape of HA particles was idealized as spherical. As shown in Fig. 1, the FGM was idealized to be composed of finite uniform layers and each layer was represented by one repeated unit cell. In this paper, the FGM was divided into five layers, in which HA particles were spherical and the volume fractions of HA are 0%, 10%, 20%, 30% and 40%, respectively. By varying the volume fractions of HA, these five layers were expressed as HA0-Ti, HA10-Ti, HA20-Ti, HA30-Ti and HA40-Ti. For example, HA10-Ti was designated as 10% of HA in the composite by volume. Moreover, the particle distribution was approximated by arranging the particles in a face-centered cubic (FCC) packing. With this packing pattern, particle volume fraction in this model could reach 74%. Due to symmetry, only one-eighth of the FCC packing is needed for analysis.

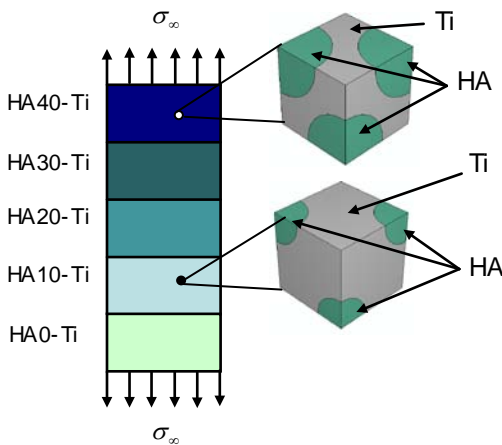


Fig. 1 Schematic illustration of two-phase functionally graded particulate material

To investigate the effect of filler particle volume fraction on the mechanical properties of FGMs, five representative unit cells were established in this paper. The required filler radius can be determined from

$$r = \left( \frac{3L^3\phi}{2\pi} \right)^{1/3}$$

where  $\phi$  is the volume fraction of HA, and  $L$  is the length of the cubic unit cell. Periodic boundary conditions were used to force the particle and matrix to remain in its original shape. The cell was loaded in tension along the y-direction. The cell was forced to maintain its regular cubic shape after deformation due to the effect of the surrounding material and the loading character<sup>[16]</sup>.

### III. CONSTITUTIVE EQUATIONS OF TI AND HA

The Ti matrix was modeled as an isotropic hardening elastic plastic solid following the incremental (J2) theory of plasticity. And the corresponding constitutive relation is available in FEM software—ABAQUS. The strength and fracture toughness of HA particles are very weak as compared with the Ti metal. The HA particles may be broken firstly when the composite is subjected to an excessive load. According to the experimental results, the

deformation behavior of the HA particle can be characterized by a purely elastic constitutive law. The generalized Hooke's law is satisfactory to reflect the deformation behavior of the HA particle in the biocomposite<sup>[17]</sup>. The constitutive equation and the failure criterion of HA can be expressed as follows:

$$\left. \begin{aligned} \sigma &= D\varepsilon, & \sigma_M < \sigma_b \\ \sigma &= 0, & \sigma_M \geq \sigma_b \end{aligned} \right\}$$

where  $\sigma$ ,  $\varepsilon$  and  $D$  are the stress tensor, the strain tensor and the elastic constitutive matrix, respectively. Moreover,  $\sigma_M$  is the von Mises stress, and  $\sigma_b$  represents the ultimate strength, and  $D$  can be defined as:

$$D = \frac{E}{2(1+\nu)(1-2\nu)} \begin{bmatrix} 2(1-\nu) & 2\nu & 2\nu & 0 & 0 & 0 \\ 2\nu & 2(1-\nu) & 2\nu & 0 & 0 & 0 \\ 2\nu & 2\nu & 2(1-\nu) & 0 & 0 & 0 \\ 0 & 0 & 0 & 1-2\nu & 0 & 0 \\ 0 & 0 & 0 & 0 & 1-2\nu & 0 \\ 0 & 0 & 0 & 0 & 0 & 1-2\nu \end{bmatrix}$$

where  $E$  and  $\nu$  are Young's modulus and Poisson ratio, respectively.

The constitutive equation and brittle failure criterion of HA have been implemented in the VUMAT subroutine of ABAQUS/Explicit. If material points satisfied the failure criterion, they would be set to zero stress and strain and eliminated from the model. Once a material point has been flagged as a "deleted" status, it could not be reactivated. The corresponding material parameters of Ti and HA are summarized in Table 1.

TABLE 1 MATERIAL PROPERTIES OF TI<sup>[12]</sup> AND HA<sup>[13]</sup>

Material	$E$ (GPa)	$\nu$	$\sigma_s$ (MPa)	$\sigma_b$ (MPa)	$\rho$ (kg/m <sup>3</sup> )
Ti	110	0.35	450	800	4500
HA	40	0.27	--	100	3219

### IV. COMPUTATIONAL RESULTS AND DISCUSSION

In this section, uniaxial tension tests along the y-axis of the repeated unit cells have been simulated using the proposed method and user-defined material subroutine. The macroscopic stress-strain curves are obtained and illustrated in Fig. 2. In this figure, when the von Mises stress of the HA particle reaches a value of 100 MPa, the particle failed and lost the load-bearing capability. The load decreases abruptly due to the presence of the brittle failure of the HA particles. And the strain softening phenomenon can be observed in the unit cell. Figure 2 also shows that the volume fraction of HA affects the mechanical behaviors of Ti/HA FGMs evidently. It is noted that the load-bearing capability of the composite decreases rapidly with the increase in the volume fraction of HA. According to the rule of mixture based on Reuss equal stress assumption, the apparent stress strain relation of graded structure was derived and plotted in Fig. 3.

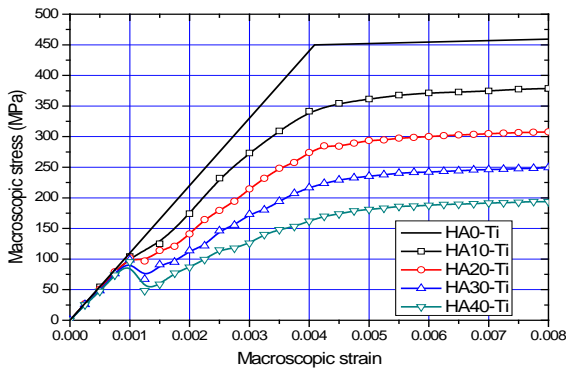


Fig.2 Macroscopic stress-strain relations predicted by the repeated unit cell model

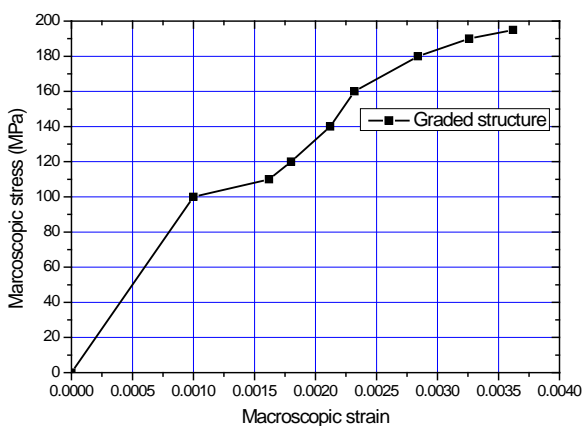


Fig.3 The apparent stress-strain relation of the graded structure

Figure 4(a) illustrates the von Mises stress contour of HA10-Ti composite before the failure of HA occurs. It can be seen that the von Mises stress distribution is interrupted at the interface between Ti and HA. Because of the higher Young's modulus in the Ti matrix, the stress of HA particle is much larger than that of the Ti matrix. Due to the absence of the load bearing capability of HA, the mechanical behaviors of the composite are similar to those of a porous one, and the applied load is entirely carried by the Ti matrix as shown in Fig. 4(b). Moreover, the work hardening of Ti matrix would continue with the increase in the strain of the unit cell. Bone, a kind of functionally graded material structure, can be modelled by the proposed method to determine its macroscopic mechanical response and the local damage in its structure.

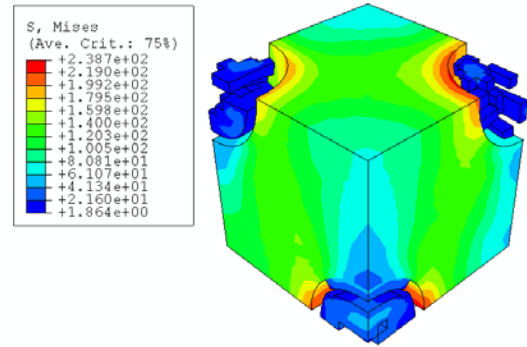
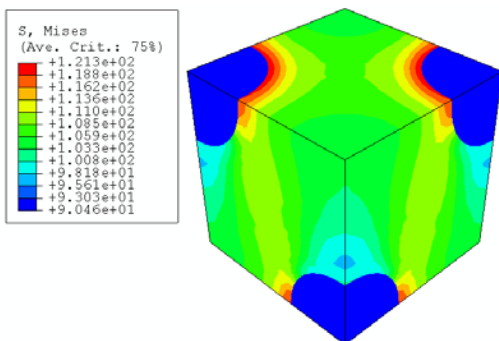


Fig.4 Von Mises stress contour of unit cell (a) no damage, (b) particle fracture

V. CONCLUSIONS

In this paper, a repeated unit cell approach with consideration of the two phase microstructure and gradual variation of FGMs has been developed. And the brittle failure criteria of HA has been implemented in the Vumat subroutine using the finite element software—ABAQUS. Using the proposed method, the macroscopic and microscopic mechanical behaviors of Ti/HA FGMs have been investigated, and the effect of the failure of HA on the Ti/HA FGMs has also been incorporated in modeling. The computational results indicate that this method can be used for simulating the microscopic damage behavior of Ti/HA composite and hence predicting the macroscopic mechanical response of Ti/HA FGMs.

ACKNOWLEDGMENT

The authors would like to thank for the support from the Research Committee of The Hong Kong Polytechnic University (Project code: G-YG18).

REFERENCES

- [1] S.L. Evans, P. J. Gregson, "Composite technology in load-bearing orthopaedic implants," *Biomaterials*, vol. 19, pp. 1329-1342, 1998.
- [2] M. S. Abu Bakar, P. Cheang, K. A. Khor, "Mechanical properties of injection molded hydroxyapatite-polyetheretherketone biocomposites," *Compos. Sci. Tech.*, vol.63, pp.421-425, 2003.
- [3] D. Aleksendric, I. Balac, C.Y. Tang, C.P. Tsui, P.S. Uskokovic, D.P. Uskokovic, "Surface characterization of PLLA polymer in HAp/PLLA Biocomposite material by means of nanoindentation and artificial neural networks," *Advances Appl. Ceram.*, vol. 109, pp. 65-70, 2010.
- [4] L. Chen, C. Y. Tang, D. Z. Chen, C. T. Wong, C. P. Tsui, "Fabrication and Characterization of Poly-D-L-lactide/nano-hydroxyapatite Composite Scaffolds with Poly(ethylene glycol) Coating and Dexamethasone Releasing," *Compos. Sci. Tech.*, vol.71, pp.1842-1849, 2011.
- [5] D. Z. Chen, C. Y. Tang, K. C. Chan, C. P. Tsui, H. F. P. Yu, C. P. M. Leung, "Dynamic Mechanical Properties and In Vitro Bioactivity of PHBV/HA Nanocomposite," *Compos. Sci. Tech.*, vol. 67, pp. 1617-1626, 2007.
- [6] Y. H. Meng, C. Y. Tang, C. P. Tsui, P. S. Uskokovic, "Fabrication and characterization of HA-ZrO<sub>2</sub>-MWCNT

- ceramic composites," *J. Compos. Mater.*, vol. 44, pp. 871-882, 2010.
- [7] G. J. Cheng, D. Pirzada M. Cai, P. Mohanty, A. Bandyopadhyay, "Bioceramic coating of hydroxyapatite on titanium substrate with Nd-YAG laser," *Mater. Sci. Eng.: C* vol. 25, pp. 541-547, 2005.
- [8] X. B. Zheng, M. H. Huang, C. X. Ding, Bond strength of plasma-sprayed hydroxyapatite/Ti composite coatings," *Biomaterials*, vol. 21, pp. 841-849, 2000.
- [9] X. Lin, T. M. Yue, H. O. Yang, W. D. Huang, "Microstructure and phase evolution in laser rapid forming of a functionally graded Ti-Rene88DT alloy," *Acta Materialia* vol. 54, pp. 1901-1915, 2006.
- [10] F. Watari, A. Yokoyama, F. Saso, M. Uo, T. Kawasaki, "Fabrication and properties of functionally graded dental implant," *Compos. Part B*, vol. 28B, pp. 5-11, 1997.
- [11] P. Gu, R. J. Asaro, "Crack deflection in functionally graded materials," *Inter. J. Solids Struct.* vol. 34, pp. 3085-3098, 1997.
- [12] T. L. Becker, R. M. Cannon, R. O. Ritchie, "Finite crack kinking and  $T$ -stresses in functionally graded materials," *International Journal of Solids and Structures*, vol. 38, pp. 5545-5563, 2001.
- [13] V. Parameswaran, A. Shukla, "Asymptotic Stress Fields for Stationary Cracks Along the Gradient in Functionally Graded Materials," *Journal of Applied Mechanics*, vol. 69, pp. 240-243, 2002.
- [14] G. Sankarasubramanian, S. Eswari, "Influence of size strength relation in modeling the behaviour of quasi-brittle materials," *Indian Journal of Engineering and Materials Sciences*, vol. 16, pp. 100-110, 2009.
- [15] Y. Q. Guo, C. Y. Tang, C. P. Tsui, T. M. Yue, B. Gao, *Abstract Book of Eurofillers 2007 Conference*, Zalakaros, Hungary, August 26 -30, 105, 2007.
- [16] I. Bala, P.S. Uskokovi, N. Ignjatovi, R. Aleks, D. Uskokovi, "Stress analysis in hydroxyapatite/poly-L-lactide composite biomaterials," *Comput. Mater. Sci.*, vol.20, 275-283, 2001.
- [17] H. Haddadi, C. Teodosiu, "3D-analysis of the effect of interfacial debonding on the plastic behaviour of two-phase composites," *Computat. Mater. Sci.* vol. 16, pp. 315-322, 1999.